The fate of pebbles and planetesimals entering protoplanetary envelopes

Emil Zadera

Lund Observatory
Lund University

2019-EXA155

Degree project of 60 higher education credits (for a degree of Master)
May 2019

Supervisor: Anders Johansen

Lund Observatory
Box 43
SE-221 00 Lund
Sweden

Abstract

Planetary embryos grow by the accretion of solid dust-material, ranging from cm- to m-sized pebbles up to km-sized planetesimals. However, the underlying size-distribution of the accreted material is poorly understood. When the pebbles and planetesimals encounter a protoplanet, they are subjected to the gaseous environment of the protoplanetary envelope. Because of the drag-force from the gas, the pebble- and the planetesimal-trajectories change significantly from their initial Keplerian orbits, and so does the evolution of their surface temperatures and the ablation rates. It is consequently of interest to track the evolution for a large range of particle sizes that encounter protoplanets, from small pebbles to large planetesimals. Depending on which particle size is responsible for the growth of protoplanets, and the corresponding thermal evolution and ablation, the protoplanetary core and its envelope will evolve differently. If all the accreted particles are ablated, we expect the envelopes of protoplanets to be polluted and with less massive cores. On the other hand, if the ablation is inefficient, protoplanetary cores are expected to grow efficiently. Effectively, the form in which material is accreted sets constraints on protoplanetary interior and atmospheric evolution models.

In this project, I study the evolution of both pebbles and planetesimals that encounter a protoplanet. This is done by simulating the trajectories of the in-falling solids in the protoplanetary envelope while tracing their thermal evolution, dynamical pressure, and ablation. The mass loss of the particles is further related to the accretion rates onto protoplanets of different mass, where both the solid and the ablated mass are accounted for.

From the results, I can conclude that pebbles are efficiently ablated above protoplanetary cores with masses of $0.5\,M_\oplus$. Small planetesimals, between $10^3 - 10^4$ cm in size, are fully ablated for core masses about $1 - 5\,M_\oplus$. For sizes of $10^5 - 10^6$ cm, the core masses have to reach between $5 - 10\,M_\oplus$. Finally, for planetesimals on the order of $10^7 - 10^8$ cm, several tenths of Earth-masses are required to fully ablate the impactors. This means that if protoplanets grow predominantly by pebble accretion, they grow into, so called, vapour-blobs, already at $0.5\,M_\oplus$. The evolution of the protoplanetary interior structure and the pollution of the envelope and its chemical composition is consequently determined by the internal gas-flows, dust settling, and the interchange of material between the envelope and the protoplanetary disc.

I also find that the latent heat is cooling the surface of the impactors efficiently, limiting the ablation rates. Planetesimals, that have a large reservoir of volatiles, can remain cold as they pass through the envelope by only ablating a small fraction of their total mass. I further find that the sum of the accreted solid mass and the ablated material follows the classical core accretion model, where no ablation of the particles is included. Thus, the results obtained in classical core accretion simulations are in the larger picture unaffected by ablation.

Key words: Pebble – Planetesimal – Protoplanet – Ablation – Accretion – Dynamics

Acknowledgements

I wish to thank my supervisor Anders Johansen for his guidance throughout this work and for coming up with the idea for this interesting project. I am especially thankful for the support during the stressful hours and also for the interesting discussions regarding planet formation. I also want to thank Michiel Lambrechts for his helpful comments and guidance. I further want to thank Thomas Ronnet for sharing and discussing knowledge regarding ablation of pebbles and planetesimals. I wish to thank Paul McMillan for his constructive feedback which helped improving my work. Last I want to thank the people at the department for creating an environment where I could develop as a researcher.

Populärvetenskaplig beskrivning

De mest framgångsrika planetbildningsmodellerna som forskare jobbar med idag härstammar från en idé som kom fram för nästan 300 års sedan, under 1700-talet. Det var den svenske forskaren Emanuel Swedenborg och den tyske filosofen Immanuel Kant som kom fram med en hypotes som vi idag kallar Solnebulosan. Idén bygger på att solen bildades från ett gigantiskt stoftmoln som kollapsade, på grund av gravitation, till stjärnor som omringas av roterande diskformade strukturer av gas och stoft där planeter formas. Därefter har de disklika strukturerna som vi idag observerar kring unga stjärnor blivit nämnda protoplanetära skivor.

Dock var det inte förrän år 1969 som själva modellen angående planetbildningen, som är grund för dagens forskning, blev sammanfattad I ett verk som publicerades av den sovjetiske forskaren Victor Safronov. Han beskrev hur dammkorn med is- och sten lika egenskaper I den protoplanetära skivan växer via kollisioner mellan varandra, tills de bildat kilometerstora block som vi kallar planetesimaler. Vidare uppbyggnad av planetesimalerna sker sedan genom både kollisioner och anhopning av närliggande damm på grund av gravitation. Så småningom har protoplaneter bildats, vars massa ligger mellan en tiondels-, upp till tiotals gånger jordens massa. Protoplaneterna är då tillräckligt massiva så att de kan hålla ihop en atmosfär av gas som I vissa fall kan växa till sig så att de blir lika massiva som gasjättarna I vårt solsystem. Forskare vet idag att själva formationen av planetesimalerna är något mer komplex än bara via kollisioner. Men att protoplaneter växer till planeter genom attraktion av allt mellan dammkorn till planetesimaler är I stort sett en accepterad hypotes.

Aktiva forskningsområden idag angår distributionen av storlekarna på materialet som faller mot protoplaneterna och hur gasflödet runt en protoplanet ser ut. Men varför har detta betydelse? En anledning är att protoplaneternas tillväxttid inte är oberoende av storleken på byggnadsmaterialet. Vidare kommer protoplaneternas atmosfär medföra att det infallande materialet börjar förstöras innan det ens har nått dess yta, likt meteorer i jordens atmosfär. Slutligen avgör gasflödet, mellan den protoplanetära skivan och protoplanetens atmosfär, om materialet som förstördes bidrar till planetbildningen eller blir bortskickat.

I detta projekt har jag utvecklat en kod som simulerar evolutionen av enskilda partiklar som faller genom protoplanetära atmosfärer. Eftersom distributionen av storlekarna på det infallande materialet inte är väl känt, undersöker jag beteendet för allt mellan millimeter- till kilometer stora objekt. I simulationerna inkluderar jag allt från gasdynamik till meteorfysik för att förstå vad som händer med protoplaneterna och byggnadsmaterialet.

Contents

List of Figures

List of Tables

Chapter 1

Introduction

The formation of the planetary systems around distant stars, and that of the sun, are active research fields to date. Over the past decades, scientists have developed models of thin gaseous and dusty protoplanetary discs that form together with the planet-hosting stars. From the disc material, centimetre-size pebbles form by coagulation of micrometre-size dust grains, and up to hundred-kilometre-size planetesimals form when high density structures of the smaller solids collapse under self-gravity. These solids, often referred to as the dust component of the disc, are subjected to a turbulent environment where they encounter each other, eventually, building up the planetary systems we see today, and indeed, the models are able to produce planetary systems in simulations. Assuming that this bigger picture is correct, we ask if the details, which are often simplified, work out as we zoom into the models. In this work, I look into the details regarding thermal and dynamical evolution of solid rocky and icy material that encounter planetary embryos embedded in protoplanetary discs. The purpose is to demonstrate the role of thermal destruction, how it affects the accretion onto protoplanetary cores and their growth, whether it is important to include in models, as well as to track the fate of single pebbles up to kilometre-size planetesimals that encountered a planetary core.

1.1 Planet formation

Protoplanetary discs form around young stars and have life-times of about $3 - 10$ million years before they dissipate (Haisch et al. 2001; Mamajek 2009; Fedele et al. 2010). This is known from observations of the ratio between stars with and without discs, in stellar clusters, as a function of the cluster-age. Within the life-time of the disc, gas giants like Jupiter and Saturn are formed while the gas is still present; thus putting a constraint on the time-scales in planetary formation models. In contrast, the terrestrial planets do not accrete a thick gaseous envelope and are thus not constrained by the life-time of the disc. However, the initial formation paths may be similar for both planet types. An additional constraint on our formation models is the positive correlation between the giant planet occurrence and the metallicity of the hosting star (Santos et al. 2004; Fischer & Valenti 2005; Buchhave et al. 2012), which suggests that planets are easier to form in discs with higher abundance of solid material. This powerful constraint favours one planetary growth

model which strongly benefits from the increase of solid material in discs, namely the *core accretion model*.

The core accretion model assumes that the cores of planets form first and grow larger by accretion of solids from the protoplanetary disc. If the cores reach a mass above about one, to $\sim 10\,M_\oplus$, they start accreting the surrounding gas, and eventually, if the mass of the gaseous envelope becomes equal to the core-mass, a runaway gas accretion causes them to grow into gas giants (Mizuno 1980; Pollack et al. 1996). Early core accretion models have assumed an accretion onto the cores that is dominated by 1-100 kilometre-size planetesimals, e.g. Mizuno (1980). However, this assumption results in long core-growth time-scales compared to the disc life-time, or require planetesimal column-densities in the disc to be amplified by a factor $2-3$ times the *minimum-mass solar nebula* (MMSN Hayashi 1981; Pollack et al. 1996), a common nominal-reference-disc-model used in the planetary-science community. Eventually, the detection of small cm-size dust particles in protoplanetary discs (Testi et al. 2003), combined with the research of pebble-dominated accretion (Lambrechts & Johansen 2012), opened the door to a more efficient accretion regime, *pebble accretion*. Nowadays, the core accretion model is a highly active research area, and models that combine both pebble and planetesimal accretion are looked into, e.g. Alibert et al. (2018).

The wide range of dust-particle sizes in protoplanetary discs can be understood from the evolution from dust grains to planetesimals: Coagulation and sedimentation of dust grains result in cm-sized pebbles (Johansen & Lambrechts 2017). The pebbles begin to drift towards the star because of the headwind from the gas (Nakagawa et al. 1986), but as they drift, multiple pebbles can collectively form a larger structure which slows down their drift speed. At this point, pebbles from the outer disc can catch up to the collective structure and add to its mass[1]. Finally, when the dust to gas ratio at the location of the filament of pebbles is high enough, it collapses under self-gravity into planetesimals with sizes on the order of $\sim 10^1 - 10^2\,\mathrm{km}$ (Johansen et al. 2012, 2015). The turbulent motion in the disc can further aid the formation of high-density pebble-structures by inducing local pressure maxima towards which pebbles can drift. The formed planetesimals continue to grow by planetesimal and pebble accretion, but may also fragment in collisions to produce an intermediate-size population of solids – the planetesimals are kinematically hotter compared to minor bodies in the disc, in the sense that they are easily scattered by protoplanetary embryos, hence the chance of colliding planetesimals increase (Nesvorný et al. 2010; Rafikov 2004). Ultimately, a planetary embryo with a mass above $0.1\,M_\oplus$ is formed that is capable of altering the local density, pressure, and temperature structure of the surrounding gas, enough to change the trajectories and the fate of the in-falling dust particles. The temperatures in the envelopes may reach up to $10^4\,\mathrm{K}$ within a few core radii, which is significantly hotter than the typical mid-plane disc-temperatures outside of $1\,\mathrm{au}$ on the order of $10^2\,\mathrm{K}$ (Lambrechts et al. 2014). The in-falling planetary solids thus experience a harsh environment that tears them as they come close to the protoplanetary core - Similar to meteors in the atmosphere of the Earth.

[1] A process referred to as the streaming instability.

1.2 Recent observations and motivation

The *Atacama Large Millimeter/submillimeter Array* (ALMA) has recently revealed a large variety in the morphology of protoplanetary discs in the *Disk Substructures at High Angular Resolution Project* (DSHARP Andrews et al. 2018). Astronomical interferometry was used at the ALMA observatory, combining up to 66 antennas that provided baselines ranging from a few metres up to several kilometres. A focus of the DSHARP survey was to utilize the 240 GHz/1.25 mm band (Band 6 at ALMA), with a spatial resolution down to 5 au, to trace the distribution of dust grains in 20 protoplanetary discs. By operating in the mm-wavelength regime, it is possible to see the light, from the disc-hosting stars, which has been scattered off dust grains. Notably, the wavelengths of the scattered light is related to the size-distribution of the grains. Consequently, ALMA probed a certain regime of grain-sizes, typically sub-cm sizes; further discussed by Birnstiel et al. (2018), who applied a set of models to the ALMA data and could, for example, conclude that the maximum size of the grains reached at least 0.2 cm for the system HD 163296.

Figure 1.1 shows the morphological variations observed with ALMA including large-scale spiral structures (Elias 27); and further, in favour of the core accretion model which require protoplanetary cores, we find discs with concentrated dust-rings where possibly planetary embryos reside (Elias24, AS 209, and HD 163296). The three last-mentioned were studied by Dullemond et al. (2018), who argued that the dust to gas ratios are large enough to trigger gravitational instabilities to form planetesimals, following the criterion derived by Youdin & Goodman (2005). The structure of the gaps in the discs have further been studied in hydrodynamical simulation by Zhang et al. (2018), who demonstrated that planets with masses on the order of a Jupiter-mass could be responsible for the distribution of dust-rings, due to their ability to alter the local pressure gradients of the gas.

It is therefore of interest to study the growth of giant planets by the means of the core accretion model: First, the initial accretion onto planetesimals and the growth of protoplanetary cores; and secondly, the flow of gas onto large planetary embryos which deplete the local disc and pushes away solid material from the planetary orbit to form the observed ring-structures.

With the new observations and the deduced results in mind, I study the accretion of material onto protoplanetary cores. These are the primordial bodies of Mars-mass up to a few 10 Earth-mass cores. The goal is to understand which physical processes are of importance in core accretion models. Specifically, I study the heating-, dynamical-, and mass-evolution, also known as ablation, for a wide range of sizes of dust particles in protoplanetary envelopes. By doing so, I evaluate the importance of destruction processes that affect the in-falling material. In detail, it will tell us in what form the material is accreted, e.g. in vapour or solid form, and whether the dust particles hit the core or are destroyed in the envelope. The dominant form of accretion gives an insight on the structure of the final protoplanet, differing vapour-blob and solid-core embryos for the respective cases when all material is vaporised, or when it hits the core in a classical sense.

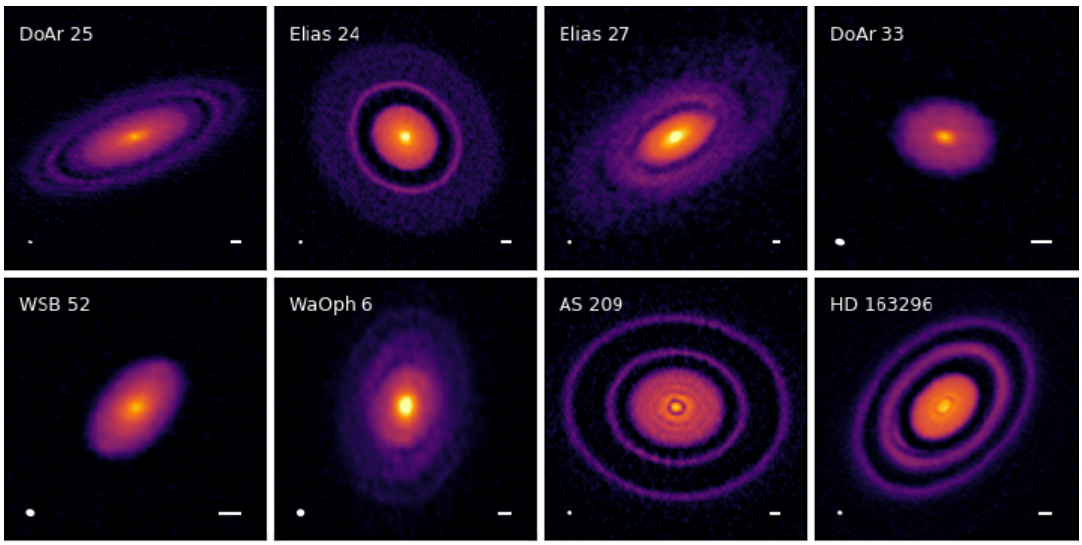

Figure 1.1: A subset of the continuum emission images in the 1.25 mm band from the DSHARP survey, observed by ALMA (Andrews et al. 2018). The emission is in this case predicted to come from sub-cm dust grains which scatter the light from the stars. The white mark at the lower left and right corners on each image correspond to the beam-size and a 10 au scale-bar, respectively, for comparison. See Section 1.2 for further details.

1.3 Physics of meteors in protoplanetary envelopes

The physics regarding meteors in the atmosphere of the Earth is most often based on empirical methods which can be described by a variety of both advanced and simplified destruction models, e.g. (Borovička & Spurný 1996; Register et al. 2017). In the models, several parameters, such as the internal strength and the fraction of absorbed energy onto the meteor are fitted to the observations of light-curves to describe the meteor phenomena. However, for a protoplanetary meteor, we have to make educated guesses about the material properties as it is not certain that they had the same structure as the small bodies in our solar system today. The purpose of this section is to give a basic understanding of the physics and the questions asked regarding protoplanetary meteors. The next subsection is dedicated to the rather well understood gas-drag, followed by the more uncertain ablation and the fragmentation models that are applied in simulations today.

1.3.1 Gas-drag

In the late seventies Weidenschilling (1977) described the terminal velocities of dust particles in protoplanetary discs that are reached due to the gas-drag. The drag is present because of an orbital velocity difference between the gas and the dust in the disc, as a result of a pressure gradient that is felt by the gas but not the dust. The apparent headwind robs the dust of angular momentum, making the solids drift towards the global pressure

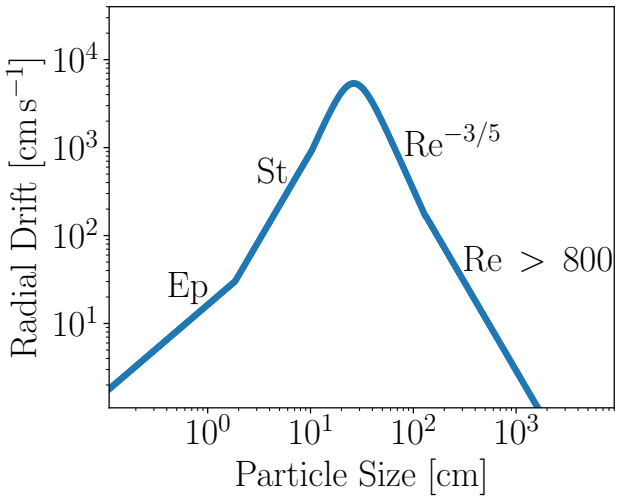

Figure 1.2: The radial drift velocity towards the star due to gas-drag in a MMSN, at 5 au, as a function of particle size. The scaling in the Epstein, Stokes, and the two following non-linear regimes, respectively, have been derived based on the work of Weidenschilling (1977).

maxima in the disc, or local maxima if present, where the gas obtains the same velocity as the dust and thus the gas-drag vanishes. The drag is consequently responsible for e.g. the drift of dust towards the star, as well as the efficient pebble accretion onto protoplanets due to the local pressure gradient induced by the planetary embryo (Lambrechts & Johansen 2012). Figure 1.2 shows the radial drift velocities towards the star in a MMSN at 5 au as a function of the particle size. There are four drift regimes which have been marked in the figure: the Epstein drag, Stokes drag, and two non-linear regimes (Weidenschilling 1977). Notably, the radial-drift peaks at decimetre-size particles, meaning that they are most affected by the drag. Meanwhile, because the centimetre-size and smaller pebbles are strongly coupled to the gas and are swept with its flow, the headwind becomes small, hence the radial drift decreases. On the other hand, large planetesimals plow through the gas as the drag-force becomes negligible, slowing the radial drift. The in-falling projectiles inside protoplanetary envelopes either: pass the planet because they can not decouple from the gas, get scattered efficiently because of negligible drag and small collisional cross-sections, or finally, drift efficiently towards the core. Hence the dynamical interplay between gas and dust plays an important role in accretion models.

1.3.2 Ablation

Meteors are subjected to both kinetic heating through friction, and radiative heating from the atmosphere itself (Pollack et al. 1986; Podolak et al. 1988). The heating of the meteor surface results in a mass loss which is referred to as ablation. This section explains the

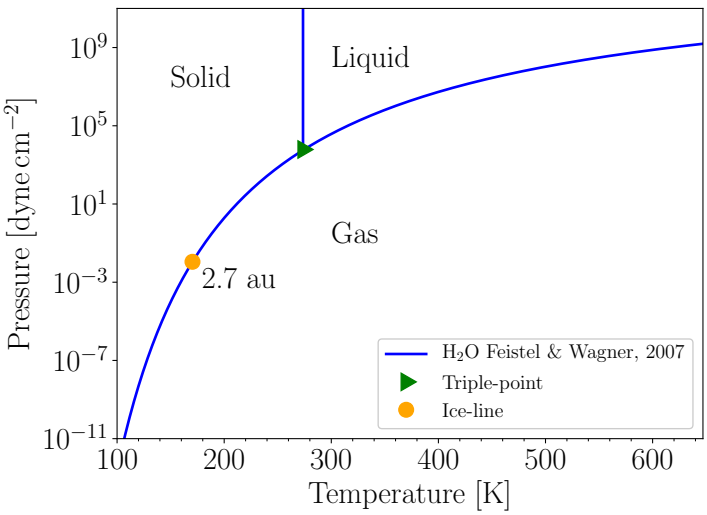

Figure 1.3: The phase-diagram of water up to the critical temperature at 647 K. The temperature and pressure conditions in the MMSN passes the equilibrium line between the solid and gaseous phase at a heliocentric distance of 2.7au, resulting in a water ice line. The equilibrium lines are calculated from the data of Feistel & Wagner (2007).

conditions in which material ablates, followed by the energy-transport and surface-heating.

1.3.2.1 Conditions for ablation

The physical ablation mechanism comes in the form of sublimation or melting, where the vapour-pressure and temperature involved determine the mode. The two channels can be understood from phase-diagrams of the involved species; an example for water being shown in Figure 1.3[2]. The blue lines indicate the equilibrium conditions, where the rate of condensation of gas is the same as the rate of vaporization of the solid- or liquid-phased material. At the triple-point, an equilibrium is reached between the three phases, and an almost straight line above this point corresponds to the region when the melting rate of solid material equals the freezing rate of the liquid. Typically, the pressures involved throughout this work are less than at the triple-point, hence, I will only refer to the phase-change between the solid and the gaseous phase. For a given temperature, the equilibrium line, also known as the saturated vapour-pressure, determines the maximum amount of vapour above a solid surface for a given species. By increasing the vapour content, the vapour-pressure is increased, hence, we move up in the phase-digram. On the other hand, the pressure goes down when gas is condensing back into solid-phase.

Once a meteor enters the envelope of a protoplanet, the amount of vapour required for

[2]Most commonly, the boundary-lines in the phase-diagram are derived from the Antoine equation, e.g. (Feistel & Wagner 2007). However, long polynomial models are also used, e.g. (Fray & Schmitt 2009).

saturation is negligible due to the low outer temperatures, thus no mass is lost in the form of vapour. However, once the body reaches higher temperatures, the meteor enters a region below the saturated vapour-pressure, and is forced to sublimate material in the envelope. If the available material is not enough to reach saturation, the meteor will ablate completely, assuming that it spends enough time at the given temperature. Notably, the saturated vapour-pressure is a steep function of temperature, thus, a small change in temperature can make the difference between total, or no mass-deposition.

1.3.2.2 Energy-transport and surface-heating

The ablation rate is determined by the temperature at the surface of the meteor, thus by the energy-flux from the environment onto the projectile. Focusing on protoplanetary envelopes, I assumed that the envelope is smoothly connected to the disc, thus avoiding any violent shock-events that Earthly meteors suffer on entry. This section first discusses the frictional heating, followed by the radiative heating, and finally introduces the endothermic cooling due to sublimation.

As the meteors move in the gaseous environment, a fraction, Λ, of the energy dissipated in the gas is transferred to the solid. From the meteor community, the absorbed energy can be related to a mass loss through the, so called, *ablation coefficient* σ_a $[\mathrm{kg\,J^{-1}}]$ (Field & Ferrara 1995; Zahnle 1992), defined by

$$\sigma_{\mathrm{a}} \equiv \frac{\Lambda}{C_{\mathrm{D}} L}, \tag{1.1}$$

where C_D is the drag coefficient, and L $[\mathrm{J\,kg^{-1}}]$ is the latent heat of vaporization (sublimation), or fusion (melting). Observational data has then been used to find the value of this coefficient. However, the ablation coefficient varies over a large range in the literature, between 10^{-10} to 10^{-7} $[\mathrm{kg\,J^{-1}}]$ (Field & Ferrara 1995; Ahrens et al. 1994; Inaba & Ikoma 2003; Biberman et al. 1980). As the uncertainty of the ablation coefficient is large, it is rarely applied to simulations of protoplanetary impactors directly and will not be used in this work.

Nonetheless, it was pointed out by Zahnle (1992), that for altitudes 'higher than $\sim$ 30 km', observations of meteors in the atmosphere of the Earth have indicated a constant effective energy fraction of $\Lambda \approx 0.1$, while closer to the surface, the fraction may reach as low as 10^{-4}. Protoplanetary envelopes extend much further than a few core radii and it is thus a common assumption in simulations that the energy deposition fraction is constant, e.g. Podolak et al. (1988); D'Angelo & Podolak (2015); Inaba & Ikoma (2003)[3]. Without relating the frictional energy to a mass loss by the ablation coefficient, I use Λ to formulate the energy-flux onto the surface of the meteors due to friction

$$\dot{E}_{\mathrm{F}} = \pi r_{\mathrm{s}}^2 \Lambda C_{\mathrm{D}} \frac{\rho_{\mathrm{g}} v^3}{2}, \tag{1.2}$$

[3]In some cases, the fraction parameter Λ includes the drag-coefficient, In this work, however, the two are treated separately.

(D'Angelo & Podolak 2015), where πr_s^2 is the affected area (assuming a spherical body), $\rho_g v^3$ is the kinetic energy-flux, where v is the relative speed between the solid and the gas and ρ_g is the gas-density.

The meteor is subjected to radiative heating from the envelope, of which it absorbs a fraction ϵ. The meteor then re-emits some energy according to its surface temperature as a black-body, where the efficiency also is assumed to be given by ϵ (D'Angelo & Podolak 2015). Assuming that the envelope acts as a black body radiator, the net energy absorbed at the surface can be written as

$$\dot{E}_{\mathrm{R}} = 4\pi r_{\mathrm{s}}^2 \epsilon \sigma_{\mathrm{sb}} \left(T_{\mathrm{g}}^4 - T_{\mathbb{S}}^4\right) \tag{1.3}$$

where σ_{sb} is the Stefan-Boltzmann constant, T_{g} is the ambient temperature of the gas, and $T_{\mathbb{S}}$ is the surface temperature of the meteor.

Finally, the energy absorption results in an increase in surface temperature, which may trigger sublimation. The molecules at the surface of the meteor absorb thermal energy and transform it into kinetic energy to leave the body. In this case, the energy to sublime a unit of mass is given by the latent heat of sublimation L_{s} (Pollack et al. 1986) and the energy change due to this endothermic reaction is given by

$$\dot{E}_{\mathrm{M}} = L_{\mathrm{s}} \frac{\mathrm{d}M}{\mathrm{d}t}. \tag{1.4}$$

Once the energy flux is calculated, it is related to a surface temperature change, a relation where models in the literature begin to vary, e.g. Brouwers et al. (2018); D'Angelo & Podolak (2015); Ronnet et al. (2017). The specific approach used in this work is presented and discussed in Section 2.4.1.

1.3.3 Fragmentation

Meteors undergo dynamical fragmentation as they are subjected to ram-pressure in the atmosphere – a conceptional parameter that estimates the dynamical pressure at the front of the meteor e.g. Borovička & Spurný (1996); Register et al. (2017). Once the ram-pressure overcomes the internal strength of the meteor, the body fragments.

More specialized models include the fragmentation of solids, e.g. Mordasini et al. (2006). However, it requires specific assumptions on the structure of the solids to estimate their internal strengths – the dynamical pressure required to fragment the body. This limit was studied for icy and basaltic solids by Benz & Asphaug (1999), who simulated collisions of basaltic and icy solids based on a *smooth particle hydrodynamic* approach. Their resulting internal strengths varies from 0.1 MPa to 100 MPa for the considered impactor-sizes between $10^0 - 10^7$cm. This result was later compared to the dynamical pressure between the gas in protoplanetary envelopes and in-falling meteors (Inaba & Ikoma 2003, fig.2b), who found that the dynamical pressures do not reach the fragmentation limits. However, as the dynamical pressure is given by the gas-density and the relative velocities, the result is very model dependent. The internal strength of comets have further been estimated by

modelling observed impactors in Earth's atmosphere (Borovička & Spurný 1996; Register et al. 2017), which roughly agrees with the result of Benz & Asphaug (1999). Benz & Asphaug (1999) further concluded that the internal strengths of solid with sizes above 100 m are dominated by gravity, hence, even if the solids fracture internally the body remains intact as a bound rubble-pile. Consequently, their obtained strengths for this size-range are lower limits.

There are several fragmentation models; two of them are the pancake- and the discrete-fragmentation models, which further can be combined into a third model approach (Register et al. 2017). In the first, the fragmenting body is treated as a fluid of particles which flattens out in a single bow shock. In the latter, the solids split into discrete parts, where the masses or sizes of the fragments are predefined or drawn from a distribution function, e.g. Borovička & Spurný (1996). In Register et al. (2017), they compared the three above-mentioned fragmentation models by applying them to the lightcurves of the Chelyabinsk meteor (Popova et al. 2013; Brown et al. 2013). Remarkably, a simple Collective Wake model was able to predict the most basic structure of the lightcurves in the meteor event (Register et al. 2017, fig.6, Collective Wake). I have thus chosen to include the Collective Wake approach in this work, which is further explained in Section 2.4.2.

1.4 Previous studies

A good overview on the fate of central impactors in gaseous envelopes was done by Mordasini et al. (2006), who included ablation and an advanced multi-staged fragmentation model that involves both a pancake-model (Zahnle 1992), and Rayleigh-Taylor instabilities in the front of the solid (Sharp 1984; Roulston & Ahrens 1997; Korycansky et al. 2000).

In Figure 1.4, a key result of Mordasini et al. (2006) is shown, that is, the minimum meteoric mass that is able to penetrate to the protoplanetary core, as a function of the envelope mass. From the figure it can be concluded that for low-mass envelopes, as small as centimetre sized particles can reach the core, and as the envelope mass increases, the required particle size goes up, as expected. However, once particle sizes of a few $\sim 10^5$ cm are reached, Mordasini et al. (2006) argues that the meteors fragment in a burst into tiny fragments that ablate in the envelope, which can be seen as a tooth shaped curve in Figure 1.4. If the particle size increases further, the fragments become gravitationally bound and the meteor remains intact. The further evolution of the particle depends on the ablation time-scale versus the time it takes to reach the core.

This is somewhat in contradiction to the result of Inaba & Ikoma (2003), where the meteors did not reach the limiting ram-pressures. It should be noted that in Mordasini et al. (2006), the simulations are central impacts with velocities equal to the Hill speed[4], which is a simplified case. In practice, the trajectories of the meteors should be included, as they set the time-scales over which the material has time to ablates. Furthermore, the frictional heating, as well as the dynamical pressure depend on the gas flow. The work

[4]The approximate velocity on which planetesimals are scattered by protoplanets.

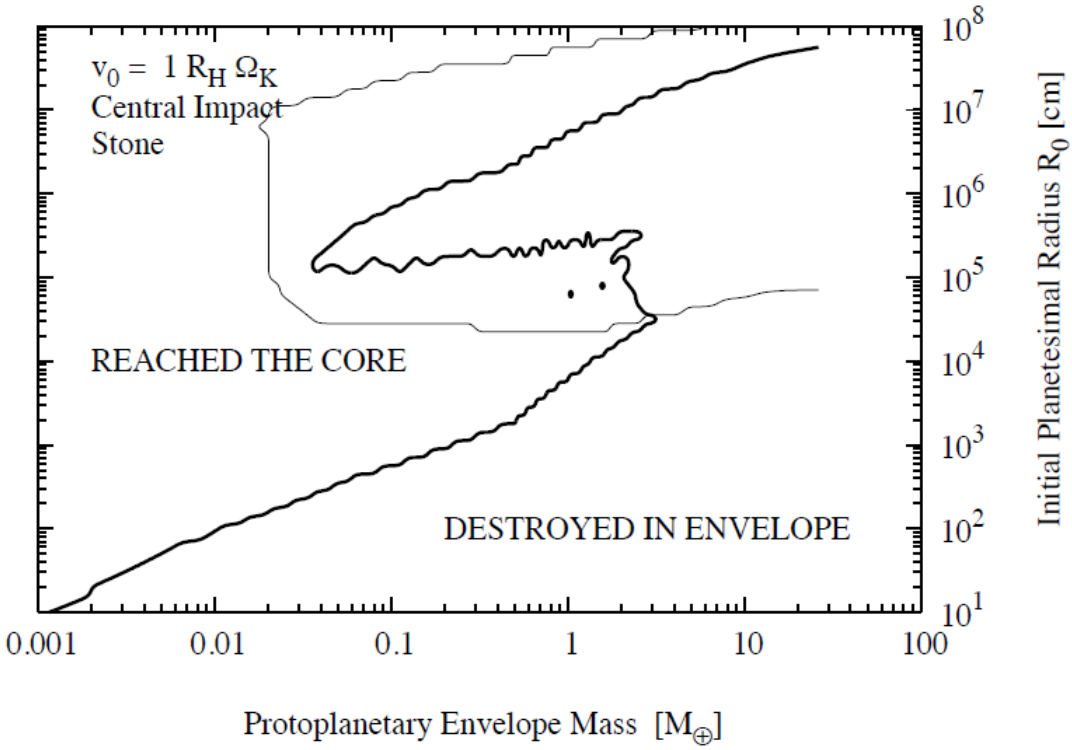

Figure 1.4: The minimum size of the incoming solid to reach the core for a given envelope mass (Mordasini et al. 2006). When the solids are below roughly 10^5 cm, the dominating mass loss is due to ablation. Above 10^5 cm, the solids reach their fragmentation limits, hence, they fragment into small particles that rapidly get ablated. As the impactor size further increases, the fragments remain bound by self-gravity, allowing the planetesimals to penetrate the massive envelopes.

of Mordasini et al. (2006) provides a base of what to expect in simulations but does not necessarily provide the accurate results for a given set of environmental parameters.

A more recent study was made by Brouwers et al. (2018), who found that the ablated mass fraction for 1 km-sized particles remain smaller than 10^{-2} for protoplanetary cores below $2\,M_\oplus$. For the larger picture, this would mean a low accretion rates in the form of vapour for planetesimals. For small ~ 0.1 m rocks, their simulations predict full ablation as was also obtained by Mordasini et al. (2006).

Brouwers et al. (2018) further looked at the breakup distance from the core, where the particles fragment. They found that for *weak*[5] particles, the disruption occurs on a few protoplanetary radii from the core surface. This may also explain why Inaba & Ikoma (2003) did not find fragmentation crucial, as it occurs when the particles are practically considered accreted in simulations.

Noteworthy, a lot of the work related to ablation in planetary formation models done

[5]They refer to particles as weak when their internal strength is below 1 Mpa.

today is based on early models, e.g. by Podolak et al. (1988), who studied the vaporization and melting of planetesimals. The ablation model has since then been marginally improved and a good description can be found in D'Angelo & Podolak (2015). The ablation model used in this work is a modified version of the prescription of D'Angelo & Podolak (2015), that was also used by Ronnet et al. (2017), and assumes that the equilibrium surface temperatures of the impactors are reached on small time-scales in comparison to the travelling time-scale.

Both projects with simplified gas-flows around the protoplanets, and those with complex hydrodynamic simulations have indicated that the accretion of pebbles is much more efficient than planetesimal accretion (Lambrechts & Johansen 2012; Popovas et al. 2018). This is the consequence of the gas-drag that robs the pebbles of their angular momentum, hence making them spiral towards the core. It is closely related to this work, as I will combine the destruction of the impactors with a simple gaseous flow around the protoplanet. The question remains whether the destruction of the solids change significantly, or not, when the dynamics are taken into count.

In summary of this section, previous work have studied the destruction of projectiles in protoplanetary envelopes, focusing on explaining the difference in importance of ablation and fragmentation depending on the protoplanetary mass and the size of the impactors. In general, the results indicate that small particles are easily ablated, while large planetesimals only ablate a small fraction of their mass. Furthermore, fragmentation is most likely occurring within a few core radii and may thus not affect the core accretion rate substantially in simulations. Finally, if particle destruction is not included, it is known that pebbles are accreted much more efficiently than planetesimals. The question remaining is whether the dynamics from the models without ablation in combination with the mass-evolution of the impactors will change the final accretion rates.

1.5 Structure of the thesis

The thesis is divided into four chapters: Chapter 1 introduces the topic of this work. Chapter 2 presents the model of the protoplanetary disc and the envelope, as well as the equation of motion and the impactor destruction mechanisms used in this work. In Chapter 3 the results are shown, where both the accretion rates onto protoplanets and the evolution of single impactors are brought to light. Finally, in Chapter 4 the results are discussed and concluded.

Chapter 2

Theory and model

In this chapter, I present the model of the protoplanetary disc (Section 2.1) and the protoplanetary envelope (Section 2.2), followed by the equation of motion (Section 2.3) and the destruction mechanisms of the in-falling bodies (Section 2.4). The derivations of the equations are not included in this paper, and the reader is directed to the cited literature for further details.

2.1 Disc structure

The protoplanetary disc model provides a basis for the temperature, the density, and the bulk composition around a potential protoplanet. Because the ablation is sensitive to the composition of the impactors it is important for the disc-model to be accurate. As protoplanetary discs evolve on much longer time-scales ($\sim 10^6$ years) compared to the time-scale on which single pebbles and planetesimals interact with the protoplanet, it is reasonable to assume a static disc model. A common model that is often used as a reference in the planetary science community is the *Minimum Mass Solar Nebula* (MMSN Hayashi 1981), which is used in this work.

The MMSN is a fair approximation about 5 au from the host star when compared to more realistic hydrodynamical models, e.g. Bitsch et al. (2015). However, I will extrapolate the model between 1 and 100 au to obtain the general trend of the temperature, the density, and the pressure in the disc. The MMSN is constructed by distributing the mass of the planets in the solar system evenly over the distance between the planets. This mass becomes the minimum dust content in the protoplanetary disc to form the planets in the solar system and assumes that the planets formed efficiently in situ (Hayashi 1981). The model then assumes a column-density of the gas that is 100 times the dust content resulting in a gas column-density of

$$\Sigma_{\mathrm{g}} = 1700\,\mathrm{g\,cm^{-2}}\left(\frac{r}{\mathrm{AU}}\right)^{-3/2}, \tag{2.1}$$

where r is the distance from the star. By letting the density of the gas have a Gaussian distribution in the vertical direction, Equation 2.1 can be used to obtain the mid-plane density as

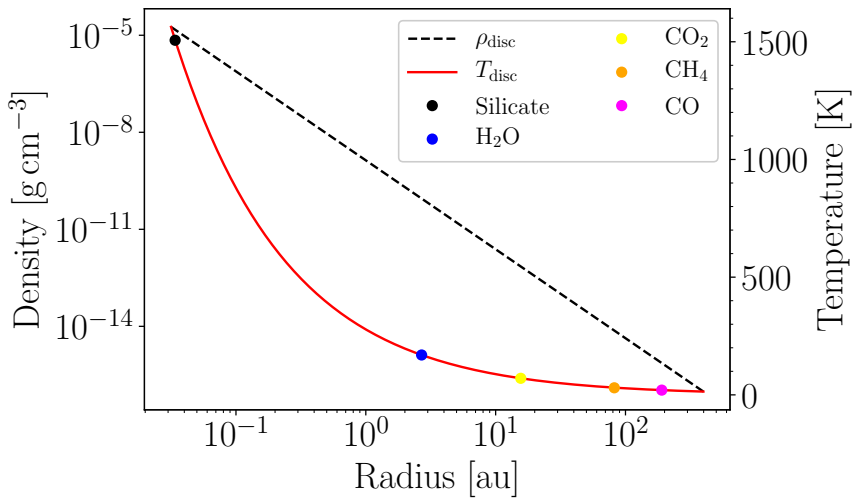

Figure 2.1: The density and temperature profile of the MMSN. The coloured points correspond to the ice- or rock-lines according to Madhusudhan et al. (2014), where the respective materials condensate, further discussed in Section 2.1.1.

$$\rho_{\rm g} = \frac{\Sigma_{\rm g}}{\sqrt{2\pi}H}, \tag{2.2}$$

where H is the gas scale-height, defined as

$$H = \frac{c_{\rm s}}{\Omega}. \tag{2.3}$$

Here, Ω is the Keplerian frequency $\Omega = (GM_\star/r^3)^{1/2}$, where G is the gravitational constant and $M_\star$ is the stellar mass, assumed to be one solar mass in this work. $c_{\rm s}$ is the local sound speed, calculated by assuming an ideal gas such that

$$c_{\rm s} = \left(\frac{k_{\rm B}T}{\mu m_{\rm H}}\right)^{1/2} = 9.9\times10^4\left(\frac{2.34}{\mu}\frac{T}{280\,{\rm K}}\right)^{1/2}\,{\rm cm\,s^{-1}}, \tag{2.4}$$

where $k_{\rm B}$ is the Boltzmann constant, $\mu = 2.34$ is the mean molecular weight in the disc (Hayashi 1981), and $m_{\rm H}$ is the mass of a Hydrogen atom. The temperature, T, is derived by assuming a low opacity, no viscous heating, and that the disc acts as a black-body emitter. In this simplified case, the temperature at each location is given by the solar irradiation, resulting in

$$T_g = \left(\frac{L_{\rm o}}{16\pi\sigma_{\rm sb}r^2}\right)^{1/4} \approx 280\,{\rm K}\left(\frac{r}{\rm AU}\right)^{-1/2}, \tag{2.5}$$

(Hayashi 1981), where $L_{\rm o} = 3.828\times10^{33}\,{\rm erg\,s^{-1}}$ is the stellar luminosity, assumed to be solar. The pressure throughout the disc is finally obtained from the ideal gas law as $P_{\rm g} = c_{\rm s}^2\rho_{\rm g}$. The density and the temperature profiles are shown in Figure 2.1.

2.1.1 Chemical composition of the impactors

Given the temperature and pressure throughout the disc, the phase of its chemical components can be deduced – as was briefly introduced in the case of water in Section 1.3.2. It is important to know the phase as it determines whether a chemical species is in solid state as a part of the impactors, or is present as a part of the gas.

In this work, I base the bulk composition of the in-falling material on observations and chemical equilibrium models done by Madhusudhan et al. (2014), who obtained the volume mixing ratios between the most common species in the disc mid-plane: H_2O, CO_2, CO, CH_4, and silicates. They further mention the presence of graphite grains, which is yet another current topic in planetary science, but do not include this element in their nominal model due to uncertainties. Studies have shown a lack of carbon incorporated into the primordial bodies in the solar system compared to the interstellar medium, from which it formed (Anderson et al. 2017). Notably, the carbon grains discussed in Madhusudhan et al. (2014) are not simple carbon molecules, that would have a condensation temperature close to a few hundred Kelvin ($\sim 425 - 626\,\mathrm{K}$ Pollack et al. 1994; Lodders 2003). To avoid the uncertainties induced by assuming a carbon distribution, I have chosen to neglect the carbon grains and follow the nominal prescription of Madhusudhan et al. (2014), given in Table 2.1.

The composition of the solids is determined by the relative position of the protoplanet and the ice/rock-lines in the disc (Figure 2.1). First, I calculate the composition of the gas from Table 2.1, by assuming the solar composition of Asplund et al. (2009): $\mathrm{O/H} = 4.9 \times 10^{-4}$, $\mathrm{C/H} = 2.7 \times 10^{-4}$, and $\mathrm{Si/H} = 3.2 \times 10^{-5}$. The condensation temperatures are then used to decide whether a type of molecule is present as a solid in the disc (outside of its respective condensation-line). As an example, at 5 au the solids consists of silicates and water ice (Figure 2.1). From Table 2.1 this location results in a volume mixing ratios for the solids as

$$X = [\,\mathrm{H_2O/H}\,] = 2.19 \times 10^{-4}, \quad \mathrm{Si/H} = [\,3.20 \times 10^{-5}\,].$$

The volume mixing ratios of the molecules in solid form are then multiplied by their molecular weight to obtain the mass-fractions: $\mu_{\mathrm{CO}} = 28.01$, $\mu_{\mathrm{CH_4}} = 16.04$, $\mu_{\mathrm{CO_2}} = 44.01$, $\mu_{\mathrm{H_2O}} = 18.02$, $\mu_{\mathrm{C}} = 12.01$, $\mu_{\mathrm{Mg_{1.1}Fe_{0.9}SiO_4}} = 140.69$[1]. The fraction of each molecular species is finally determined by dividing each mass-fraction with the sum of all mass-fractions, for the example at 5 au I obtain

[1] I assume that the silicates can be treated as a combination of forsterite and fayalite – end-members of olivine which is present in comets (Kimura et al. 2002; Nagahara et al. 1994) and further used in chemical mixing models in protoplanetary discs, e.g. Woitke et al. (2009); Draine & Lee (1984). However, Madhusudhan et al. (2014) assumes that each silicate grain contains three oxygen atoms per molecule (Table 2.3), hence silicates in the form of e.g. enstatite ($MgSiO_3$) or ferrosilite ($FeSiO_3$) which have a complex sublimation pattern that includes the formation of forsterite layers (Tachibana et al. 2002). I consider the silicates as olivine whose sublimation can be described without involving complicated chemical reactions Nagahara et al. (1994) and at the same time remain conservative due to their high condensation temperatures. Thus, if the silicates are sublimated in this work, the enstetite or ferrosilite correspondence would also be transformed into vapour.

Table 2.1: The chemical volume mixing for the gas in the protoplanetary disc in terms of the elemental volume fractions of the solar composition as a function of condensation temperature. For details regarding Case 1, I refer to Madhusudhan et al. (2014).

Species	T_{cond} (K)	Case 1[b]:X/H
CO	20	$0.45 \times C/H(0.9 \times C/H \quad \text{for} \quad T < 70\,K)$
CH_4	30	$0.45 \times C/H(0 \quad \text{for} \quad T < 70\,K)$
CO_2	70	$0.1 \times C/H(0 \quad \text{for} \quad T < 70\,K)$
H_2O	170	$O/H - (3 \times Si/H + CO/H + 2 \times CO_2/H)$
Carbon grains	150	0
Silicates	1500	Si/H

$$[\, f_{H_2O},\, f_{silicate}\,] = \frac{X_x \mu_x}{\sum_x (X_x \mu_x)} = [\,0.47,\, 0.53\,].$$

To comment on the work of Madhusudhan et al. (2014), they assume three oxygen atoms for each silicate molecule while in this work I treat the silicates as olivine with four oxygen atoms. Changing the factor of three into four in Table 2.3 results in water and silicate fractions of 0.43 and 0.57, respectively. However, since the results in this work are unaffected by the small change in fraction, I choose to follow the original prescription of Madhusudhan et al. (2014) as stated in Table 2.3. Regarding the different forms of silicates and their thermal properties, see footnote 1 (Page 19) and the cited literature within.

2.2 Protoplanetary envelope

The protoplanetary envelope changes the temperature and the density structure around the solids from that of the protoplanetary disc. Consequently, the equilibrium mixing described in Section 2.1.1 does not necessarily uphold due to ablation (Section 1.3.2). This section is dedicated to the model of the protoplanetary envelope.

The planetary core is here assumed to be small enough such that the disc structure is not perturbed significantly by its gravity to where a potential gap opens up in the disc (Dullemond et al. 2018). This happens at the pebble isolation mass[2] which is on the order of a few $10\,M_\oplus$ (Bitsch et al. 2018; Lambrechts & Johansen 2014).

It is a reasonable first assumption that the outer boundary conditions of the envelope are to be evaluated where the gravitational influence of the protoplanet balances that of

[2]Above this mass, the protoplanet alters the local disc-structure by inducing a pressure gradient on the gas. This results in a halting of the dust accretion onto the core and allows the protoplanetary envelope to contract and cool. Following, the protoplanet efficiently accretes gas and open up a gap in the disc.

the stellar tide. This is at the so called Hill radius, defined as

$$R_{\rm Hill} = r_{\rm p}\left(\frac{M_{\rm p}}{3M_\odot},\right)^{1/3} \tag{2.6}$$

where $r_{\rm p}$ is the semi-major axis of the protoplanet, and $M_{\rm p}$ the protoplanetary mass. From this point, I assume a hydrostatic, fully convective, ideal and adiabatic envelope. The equations governing the hydrostatic envelope are given by

$$-\frac{1}{\rho_{\rm e}}\frac{\partial P_{\rm e}}{\partial r} = \frac{GM_{\rm p}}{r^2}, \quad P_{\rm e} = \frac{k_{\rm B}T_{\rm e}}{\mu m_{\rm H}}\rho_{\rm e} \quad \& \quad P_{\rm e} = K_{\rm r}\rho_{\rm e}^{\gamma}, \tag{2.7}$$

where $\gamma = 7/5$ is the adiabatic index for a diatomic gas, and $\mu = 2.34$ is the mean molecular weight of the envelope, which is assumed to be the same as the that of the disc unless otherwise mentioned. $K_{\rm r}$ is the polytropic constant that is depending on the semi-major axis of the protoplanet and can be determined from the ideal gas law as

$$K_{\rm r} = \frac{k_{\rm B}T_{\rm r}}{\mu\rho_{\rm r}^{\gamma-1}}, \tag{2.8}$$

where the subscript r means that the parameter is evaluated from the disc profile, at the semi-major axis of the protoplanet. These parameters also define the boundary conditions for the envelope. The solution to Equation 2.7 then becomes

$$\rho_{\rm e}(r) = \left[\frac{GM_{\rm p}(\gamma-1)}{K_{\rm r}\gamma}\left(\frac{1}{r} - \frac{1}{R_{\rm Hill}}\right)\right]^{1/(\gamma-1)}, \tag{2.9}$$

which further relates to the temperature through the ideal gas law as

$$T_{\rm e}(r) = \frac{K_{\rm r}\mu m_{\rm H}}{k_{\rm B}}\rho_{\rm e}^{\gamma-1} \propto r^{-1}. \tag{2.10}$$

In Figure 2.2, the envelope profile of a set of protoplanetary cores have been plotted for 1 and 5 au, where I assume a MMSN disc. Note that the temperature and the density scales in the same way and are thus described by the same lines. I compare the model to the literature, e.g. Lambrechts et al. (2014), who included radiative transfer zones, and my model is in rough agreement down to a distance from the core of a few core radii. Beneath this point the density and temperatures starts to get underestimated, hence if the solids do reach the core in our simulation, it can still be the case where they were destroyed above the surface. Furthermore, Figure 2.2 shows the silicate- and the water ice lines inside the envelopes for the respective cores. The method of obtaining the locations of these condensation lines is presented in Section 2.2.1.

2.2.1 Condensation lines in the envelope

Like in the case of the protoplanetary disc, the pressure and the temperature profile in the envelope gives a hint on where the impactors are sublimating material. Note however, that

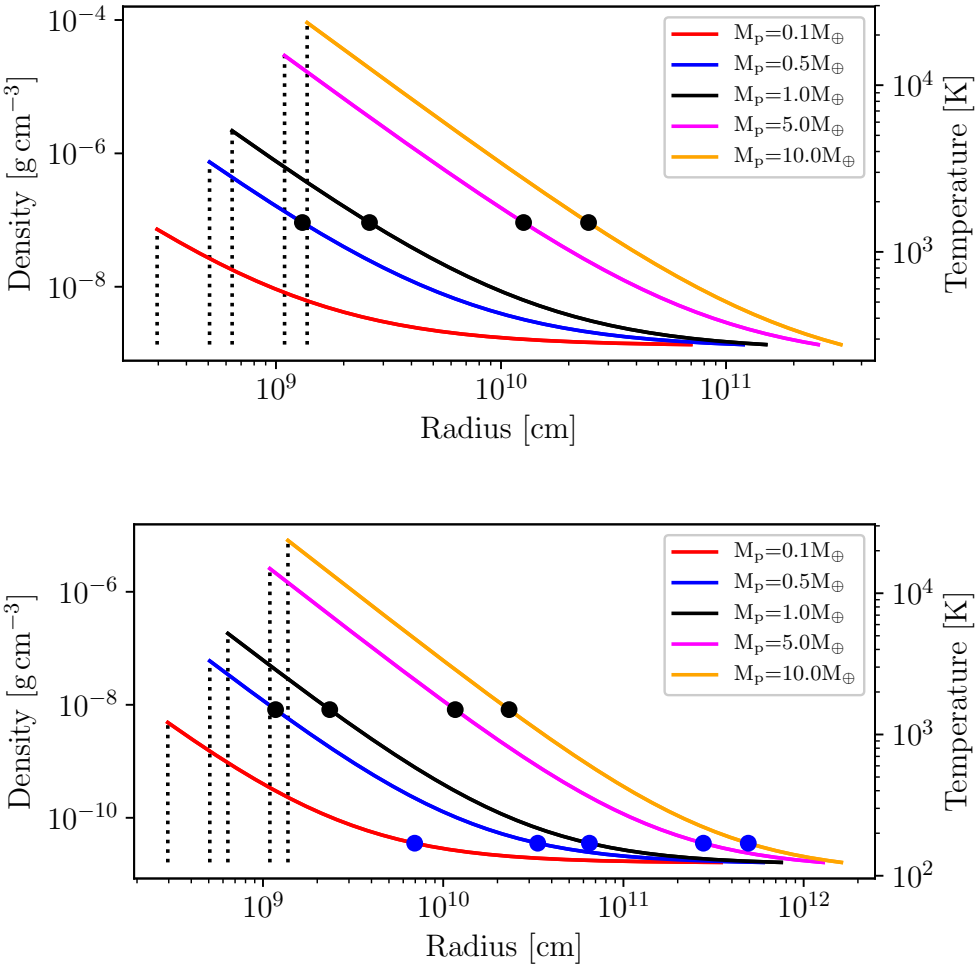

Figure 2.2: The density and temperature structure of the protoplanetary envelope of a $0.1 - 10 M_\oplus$ core, at 1 au (top), and 5 au (bottom). Note that the temperature and density has the same scaling over the two ranges on the vertical axes. The profiles are plotted between the radius of the core (dotted lines), and their respective Hill radii. Finally, the black and the blue dots correspond to the silicate- and the water ice/rock-lines.

the sublimation rate is set by the temperature at the surface of the projectile, rather than that of the envelope. While in the disc, it is reasonable to assume that the temperatures are the same, as no significant friction or endothermic cooling is expected, the altered trajectories and the steady rise in the ambient temperature due to the planetary embryo does not guaranty this equilibrium scenario. Nonetheless, it is interesting to know how the ablation of the impactors relate to the condensation lines. In this section, it is demonstrated how the rock/ice lines are derived, which is tightly connected to the sublimation rate that is described in Section 2.4.1.

The properties deciding whether a solid sublimes or not are given by the vapour-pressure of its chemical components and the temperature. The vapour-pressure, $P_{\mathrm{v,x}}$ is given by the pressure profile of the envelope, P_{e}, multiplied by the fraction of the chemical species, X_{x}, in question

$$P_{\mathrm{v,x}} = X_{\mathrm{x}} P_{\mathrm{e}}, \tag{2.11}$$

where X_{x} is obtained from Table 2.1.

At saturation, the vapour-pressure defines the maximum vapour that the atmosphere can hold for a given temperature (blue exponential line in Figure 1.3). Hence, it also defines the equilibrium conditions under which the sublimation- equals the condensation rate. Because the molecules have a Maxwellian velocity distribution[3], the material will sublimate as long as the vapour-pressure is below saturation. This allows us to define the ice/rock-lines at the radial distance in the envelope where the vapour-pressure equals the saturated-pressure. Within the ice/rock-line, solids are expected sublimate their material.

The saturation pressure is a steep function of temperature, and is in the simplest case approximated with the empirical Antoine-equation, given by

$$\log_{10}(P_{\mathrm{s,x}}) = A_{\mathrm{x}} - \frac{B_{\mathrm{x}}}{C_{\mathrm{x}} + T}, \tag{2.12}$$

where A_{x}, B_{x}, C_{x} are constants that are specific for the molecular species in the gas, hence the subscript. However, long empirical polynomial expansions are also used in the literature, e.g. (Fray & Schmitt 2009) of the form

$$\log_{10}(P_{\mathrm{s,x}}) = D_{0,\mathrm{x}} + \sum_{\mathrm{i}=1} D_{\mathrm{i,x}} T^{-\mathrm{i}}, \tag{2.13}$$

where $D_{\mathrm{i,x}}$ are constants. It should be mentioned that a large variety of constants can be found for both Equation 2.12 and 2.13, due to different laboratory limitations from which they were obtained. In this project, I use Equation 2.12 or 2.13, depending on the source from which the constants were taken. The resulting parameters are summarized in Table 2.2.

In Figure 2.3, the vapour-pressure (red) and the temperature of the envelope (black), as well as the saturated vapour-pressure (blue), in the case of water, have been plotted for core masses of 0.1-10 $M_{\oplus}$ at 5 au. From the graph, the location at which the saturated pressure surpasses the vapour-pressure can be deduced (green filled circles), and further be related to the temperature at that distance, that is, the condensation temperature (pink filled circles).

2.3 Equation of motion

The spacial scale of interest in this work is limited within the local environment around a protoplanetary core, where the in-falling solids become actively scattered, accreted, or

[3]The Maxwellian distribution has a long high-velocity tail, meaning that there will always be a fraction of molecules that escape the surface of the material.

Table 2.2: The parameters in equation 2.12, or 2.13 for the considered chemical components in this work. The sources are as follows: (1) Fray & Schmitt (2009), (2) Haynes et al. (1992), and (3) Nagahara et al. (1994).

Molecule	A	B	C	D	E	F	Eq.	Source
CO	1.043e1	-7.213e2	-1.074e4	2.341e5	-2.392e6	9.478e6	2.13	1
CH_4	1.051e1	-1.110e3	-4.341e3	1.035e5	-7.910e5	0.00	2.13	1
CO_2	1.476e1	-2.571e3	-7.781e4	4.325e6	-1.207e8	1.350e9	2.13	1
H_2O	6.034e12	5938	0	-	-	-	2.12	2
Mg_2SiO_4	6.72e14	65649	0	-	-	-	2.12	3

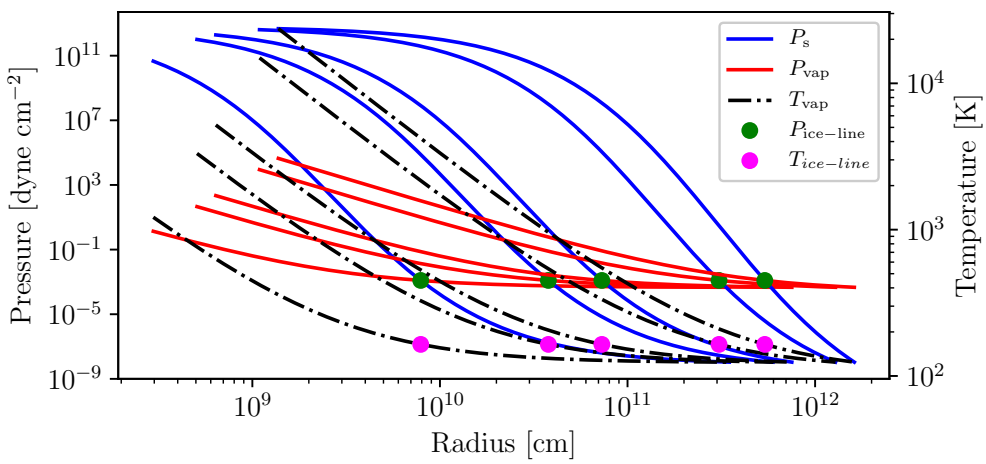

Figure 2.3: The determination of the location on the water ice lines inside the envelope by finding the intersection between the vapour-pressure (red) and the saturated vapour-pressure (blue). This is done for core-masses of 0.1, 0.5, 1.0, 5.0, and 10 $M_\oplus$ at 5 au, where the pressure and temperatures increase with the mass of the core. The corresponding condensation temperatures (pink filled circles) are then identified on the temperature profiles (black dash-dotted), at the radius of the intersection of the pressures involved (green filled circles). Notably, the condensation temperature remain nearly independent of the core-mass.

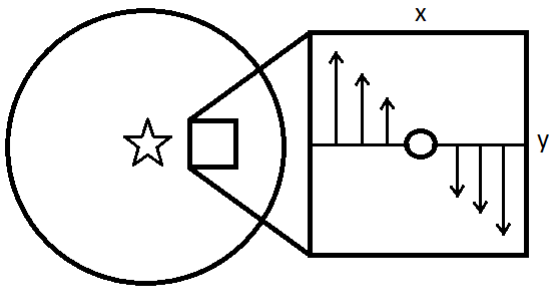

Figure 2.4: A shearing-box model that rotates with the protoplanet. The Keplerian shear velocity is indicated by the black arrows.

simply pass the planet without interaction. Consequently, it is unnecessary to simulate the protoplanetary disc on a global scale, and I focus on the local structure near the planetary core. A useful approach for this purpose is the shearing-box model, which is a simulation-frame of a small patch of the disc. In this section, I present the equation of motion for the particles that move in the frame of the shearing-box.

2.3.1 Shearing-box model

The shearing-box is centred around, and co-rotates with the protoplanet. A cartoon of a shearing-box is illustrated in Figure 2.4. The radial and the azimuthal directions of the disc are translated to the Cartesian frame of the box by linearisation of the accelerating forces. Here, the y-axis becomes the azimuthal direction in the disc, while the x-axis is the radial direction. As the Keplerian speed is faster closer to the star, the azimuthal velocity of the solids will exceed that of the protoplanet in the left half of the shearing-box, as indicated with black arrows in Figure 2.4. This also results in particles falling behind the protoplanet in the right half of the shearing-box.

In the following paragraphs, the equations of motion for the dust and the gas are presented. Generally, the motion of a dust or gas particle near the protoplanet can be obtained from the respective Euler equations of the following forms:

$$\frac{d\mathbf{v}}{dt} + \mathbf{v}\cdot\nabla\mathbf{v} = -A\rho_{\mathrm{g}}(\mathbf{v}-\mathbf{u}) - \frac{GM_{\odot}}{\mathbf{r}_{\mathrm{p}}^2} - \frac{GM_{\mathrm{p}}}{\mathbf{r}^2}, \tag{2.14}$$

$$\frac{d\mathbf{u}}{dt} + \mathbf{u}\cdot\nabla\mathbf{u} = -A\rho_{\mathrm{d}}(\mathbf{u}-\mathbf{v}) - \frac{GM_{\odot}}{\mathbf{r}_{\mathrm{p}}^2} - \frac{GM_{\mathrm{p}}}{\mathbf{r}^2} - \frac{1}{\rho_{\mathrm{g}}}\partial_{\mathbf{a}}\mathbf{P} - \frac{1}{\rho_{\mathrm{e}}}\partial_{\mathbf{r}}\mathbf{P}, \tag{2.15}$$

where, on the right hand side of Equation 2.14 and 2.15, the first term describes the drag force on the dust by the gas and the backreaction on the gas, respectively; the second term is the tidal force from the star; followed by the gravity of the planetary core. The equation for the gas further includes the pressure gradient in the protoplanetary disc and

the envelope which have been denoted $\partial_{\mathbf{a}}$ and $\partial_{\mathbf{r}}$, respectively. Furthermore, $\mathbf{v}$ and $\mathbf{u}$ are the velocities of the dust and the gas; $\mathbf{r}_{\rm p}$ and $\mathbf{r}$ are the distances from the star and the protoplanetary core; $\rho_{\rm d,g,e}$ are the densities of the dust, the gas in the protoplanetary disc, and the envelope. Here, I have used the notation of Nakagawa et al. (1986) for the drag and the back-reaction, where A is coupled to the commonly used friction-time[4], $t_{\rm f}$, hence also the Stoke's number, τ, that tells how close the motion of the dust and the gas is coupled. For the dust and the gas, respectively, the connection to the friction-time is given by

$$A = \frac{\Omega_{\rm k}}{(\rho_{\rm d} + \rho_{\rm g})\tau} = \frac{1}{\rho_{\rm g} t_{\rm f,d}} \quad \& \quad \frac{1}{\rho_{\rm d} t_{\rm f,g}} \tag{2.16}$$

where $\Omega_{\rm k}$ is the keplerian frequency. The friction-time is further discussed in Section 2.3.1.1.

Following, Equations 2.14 and 2.15 are translated to the rotating frame of the shearing-box. The centrifugal and the Coriolis forces are thus added to both equation. Furthermore, I make a first order approximation and Taylor-expansion on the tidal force, centred around the tidal pull on the protoplanet. Formally, I define the x-coordinate as $x = r_{\rm x} - r_{\rm p}$, where $r_{\rm x}$ and $r_{\rm p}$ is the semimajor-axis of a particle and the protoplanet, respetcively, where it is assumed that $r_{\rm x,p} \gg |x|$. If second order terms in the tidal force are neglected, it can be Taylor expanded as

$$-\frac{GM_\odot}{(r_{\rm p} + x)^2} = -\frac{GM_\odot}{r_{\rm p}^2(1 + \cancel{x^2/r_{\rm p}^2} + 2x/r_{\rm p})} \approx -\frac{GM_\odot}{r_{\rm p}^2}\big(1 - \frac{2x}{r_{\rm p}}\big). \tag{2.17}$$

Conveniently, the centrifugal force, defined as $r_{\rm x}\Omega_{\rm p}^2$, can be written on a similar form

$$(r_{\rm p} + x)\frac{GM_\odot}{r_{\rm p}^3} = \frac{GM_\odot}{r_{\rm p}^2}\big(1 + \frac{x}{r_{\rm p}}\big), \tag{2.18}$$

and adding Equations 2.17 and 2.18 results in the balance term

$$\dot{\mathbf{v}}_{\rm b} = 3\Omega_{\rm p}^2 x. \tag{2.19}$$

Finally, the Coriolis term describes the apparent acceleration of a particle due to the rotation of the frame as

$$\dot{\mathbf{v}}_{\rm c} = -2\mathbf{\Omega}_{\rm p} \times \mathbf{v} = \begin{pmatrix} 0 \\ 0 \\ \Omega_{\rm p} \end{pmatrix} \times \begin{pmatrix} v_x \\ v_y \\ 0 \end{pmatrix} = -2 \begin{pmatrix} -\Omega_{\rm p} v_y \\ +\Omega_{\rm p} v_x \\ 0 \end{pmatrix}. \tag{2.20}$$

where $\mathbf{v}$ can be interchanged with $\mathbf{u}$ in case of the gas. Following the above description, Equation 2.14, describing the dust, obtains the form

$$\frac{D\mathbf{v}}{Dt} + \mathbf{v} \cdot \nabla \mathbf{v} = -\frac{1}{t_{\rm f,g}}(\mathbf{v} - \mathbf{u}) + 3\Omega_{\rm p}^2 x - 2\mathbf{\Omega}_{\rm p} \times \mathbf{v} - \frac{GM_{\rm p}}{\mathbf{r}^2}. \tag{2.21}$$

[4]The time-scale over which the drag- and back-reacting forces act on the dust and the gas.

The motion of the gas (Equation 2.15) is, in addition to the Coriolis- and the balance-term, solved using a hydrostatic envelope (Equation 2.7). Furthermore, I use a form of the global pressure gradient introduced by Nakagawa et al. (1986) where

$$2\Omega_{\rm p}\eta v_{\rm k} = -\frac{1}{\rho_{\rm g}}\partial_{\mathbf{a}}\mathbf{P} \tag{2.22}$$

and η is a dimensionless parameter, such that the equation of motion of the gas becomes

$$\frac{d\mathbf{u}}{dt} + \mathbf{u}\cdot\nabla\mathbf{u} = -\frac{1}{t_{\rm f,d}}(\mathbf{u}-\mathbf{v}) + 3\Omega_{\rm p}^2 x - 2\mathbf{\Omega}_{\rm p}\times\mathbf{u} + 2\Omega_{\rm p}\eta v_{\rm k}. \tag{2.23}$$

In this first order approximation, the gas does thus not feel the presence of the protoplanet which is an acceptable case up to a few Earth-masses. However, it also depends on the location in the protoplanetary disc, caveats which are further discussed in Section 2.3.2.1.

For completeness of the equation of motion for the dust, the following subsection introduces the equations governing the friction-time of the gas drag, $t_{\rm f,d}$. The velocity field of the gas is continued in Section 2.3.2, where the terminal velocity of small dust particles also is presented which concludes the equations of motion.

2.3.1.1 Gas-drag onto the dust

The dust particles are moving in a gaseous environment and are thus subjected to gas-drag which is a force that accelerates the dust towards the velocity of the gas. Depending on the size (radius), $r_{\rm s}$, of the dust with respect to the mean free path of the gas[5], $\lambda = \mu_{\rm H}/(\sqrt{(}2)\rho_{\rm g}\pi {\rm H_{2d}}^2)$, the force follows one out of two different equations (Weidenschilling 1977). For small particles ($\lambda/r_{\rm s} > 4/9$), the force can be approximated by the Epstein drag:

$$\mathbf{F}_{\rm D} = \frac{4\pi\rho_{\rm g}r_{\rm s}^2}{3}(\mathbf{v}-\mathbf{u})c_{\rm s}, \tag{2.24}$$

while if ($\lambda/r_{\rm s} < 4/9$), the force is given by

$$\mathbf{F}_{\rm D} = C_{\rm D}\pi r_{\rm s}^2\rho_{\rm g}\frac{(\mathbf{v}-\mathbf{u})^2}{2}, \tag{2.25}$$

where $C_{\rm D}$ is the dimensionless drag coefficient of a sphere and depends on the Reynolds number, Re, (Whipple 1973) as

$$\begin{aligned} C_{\rm D} &= 24{\rm Re}^{-1} && \text{for} \quad {\rm Re} < 1 \\ C_{\rm D} &= 24{\rm Re}^{-0.6} && \text{for} \quad 1 < {\rm Re} < 800 \\ C_{\rm D} &= 0.44 && \text{for} \quad {\rm Re} > 800 \end{aligned}$$

[5]The mean free path is an estimate of the mean traveled distance before a molecule in the gas collides with another molecule. I assume a Hydrogen dominated gas, thus I use the kinetic diameter of the Hydrogen gas molecule ${\rm H_{2d}} \approx 286\times10^{-10}$ cm.

The three regimes for the Reynolds number are the Stokes drag, and two non-linear regimes, which are responsible for the corresponding drift regions shown in Figure 1.2. The Reynolds number gives an estimate on the level of turbulence in the flow by comparing the inertial force with the viscosity, η, of the gas; formally defined as

$$\mathrm{Re} = 2r_\mathrm{s}\rho_\mathrm{g}(\mathbf{v}-\mathbf{u})/\eta \quad \& \quad \eta = \frac{2\sqrt{\pi\mu m_\mathrm{H} k_\mathrm{B} T_\mathrm{g}}}{3\pi^2 H_\mathrm{2d}^2} \tag{2.26}$$

e.g. Bird et al. (2006). The time-scale over which a dust particle is affected by the gas-drag can then be estimated by dividing the relative momentum of the dust particle with the acting drag-force

$$t_\mathrm{f} = \frac{M|\mathbf{v}-\mathbf{u}|}{|\mathbf{F}_\mathrm{D}|}, \tag{2.27}$$

where $\mathbf{F}_\mathrm{D}$ is given by Equation 2.24 or 2.25, and M is the mass of the dust particle. This time-scale, also referred to as the friction-time, can be compared to the gravitational crossing time-scale Ω_p^{-1}, to estimate the efficiency of the drag-force as following:

$$\tau_\mathrm{small} = \Omega_\mathrm{p}\, t_\mathrm{f} \qquad \text{when} \quad \lambda/r_\mathrm{s} > 4/9 \tag{2.28}$$

$$\tau_\mathrm{large} = (4/9)\frac{r_\mathrm{s}}{\lambda}\tau_\mathrm{small} \quad \text{when} \quad \lambda/r_\mathrm{s} < 4/9 \tag{2.29}$$

$$\tag{2.30}$$

(Lambrechts & Johansen 2012), where τ is the Stokes number. Low Stokes number indicate that the gas-drag dominates, and the particles are swept with the gas-flow. Meanwhile, a larger Stokes number means that the gas-drag is negligible and the trajectory is determined by gravity. If the time-scales are comparable, e.g. $\tau \sim 0.1 - 1$, the particles are in an intermediate regime, where they feel the strongest headwind from the gas. Consequently, these particles are expected to drift rapidly[6].

2.3.2 The gas-flow and terminal velocities

This section presents the terminal velocities of the gas and the dust particles that are well coupled to the gas. In this scenario, the gas is efficiently sweeping the dust in its flow and it is satisfied when the friction-time is much smaller than the gravitational scattering time, $t_\mathrm{f} \ll \Omega_\mathrm{s}^{-1}$ (Ronnet et al. 2017). In this work, I found that the particles that effectively reach the terminal velocities have friction times that fall under the following criteria:

$$t_\mathrm{f} < \frac{1}{10}\Omega_\mathrm{s}^{-1} = \frac{1}{10}\left(\frac{GM_\mathrm{p}}{\mathbf{r}^3}\right)^{-1/2}. \tag{2.31}$$

In this section, the main equations and results are brought up. The full derivation of the terminal velocities can be found in Appendix B.1. The assumptions are as follows:

[6]Notably, the Stokes number is a function radial distance, due to the dependence on the Keplerian frequency, thus the size of the most rapidly drifting particles changes with semi-major axis.

1. The protoplanet moves on a circular orbit.
2. The velocities of the gas and dust grains are perturbed Keplerian flows.
3. The density of the dust is much smaller than the density of the gas.

The second assumption means that both the flow of the gas and the swept dust is dominated by the tidal force of the star, a commonly used approximation, e.g. (Nakagawa et al. 1986; Weidenschilling 1977). The Keplerian velocities for the dust, v_k, at a displaced semimajor-axis of $r_\mathrm{p} + x$, where r_p is the location of the protoplanet and $|x| \ll r_\mathrm{p}$, is given by

$$v_\mathrm{k} = \Omega_\mathrm{p}(r_\mathrm{p} + x) = \sqrt{\frac{GM_\odot}{(r_\mathrm{p} + x)^3}}(r_\mathrm{p} + x) \approx \sqrt{\frac{GM_\odot}{r_\mathrm{p}^3}}a + \frac{d\Omega_\mathrm{p}}{dr_\mathrm{p}}x = v_\mathrm{p} - (3/2)\Omega_\mathrm{p}x. \tag{2.32}$$

Following, the velocities of interest are diverging from the Keplerian velocity by a small margin $\tilde{v}_y$ and $\tilde{u}_y$ for the dust and gas, respectively. Henceforth, I solve for the divergence from the Keplerian speed. In the shearing-box frame, the Keplerian velocity of the protoplanet is subtracted, resulting in a velocity vector for the particles given by

$$\mathbf{v} = \begin{pmatrix} v_x \\ \tilde{v}_y \quad -(3/2)\Omega_\mathrm{p}x \\ v_z \end{pmatrix}. \tag{2.33}$$

Focusing on the 2-dimensional case and substituting the above velocity vector into Equation 2.21 and 2.23 results in a set of four equations to be solved in the equilibrium case:

$$\begin{aligned}
\frac{dv_x}{dt} &= -\frac{1}{t_\mathrm{f,d}}(v_x - u_x) + 2\Omega_\mathrm{p}v_y - \frac{GM_\mathrm{p}}{\mathbf{r}^3}x \\
\frac{d\tilde{v}_y}{dt} &= -\frac{1}{t_\mathrm{f,d}}(v_y - u_y) - \frac{1}{2}\Omega_\mathrm{p}v_x - \frac{GM_\mathrm{p}}{\mathbf{r}^3}y \\
\frac{du_x}{dt} &= -\frac{1}{t_\mathrm{f,g}}(u_x - v_x) + 2\Omega_\mathrm{p}u_y + 2\Omega_\mathrm{p}\eta v_\mathrm{k} \\
\frac{d\tilde{u}_y}{dt} &= -\frac{1}{t_\mathrm{f,g}}(u_y - v_y) - \frac{1}{2}\Omega_\mathrm{p}u_x.
\end{aligned}$$

As shown in Appendix B.1, when assuming that the dust is negligible compared to the density of the gas, the solution is given by

$$v_x = -2\frac{\tau}{\tau^2 + 1}\big(\eta v_\mathrm{k} + \frac{1}{\Omega_\mathrm{p}}\big[\frac{x}{2} + \tau y\big]\frac{GM_\mathrm{p}}{\mathbf{r}^3}\big) \tag{2.34}$$

$$\tilde{v}_y = -\frac{1}{\tau^2 + 1}\big(\eta v_\mathrm{k} - \frac{1}{\Omega_\mathrm{p}}\big[\frac{\tau^2}{2}x - \tau y\big]\frac{GM_\mathrm{p}}{\mathbf{r}^3}\big) \tag{2.35}$$

$$u_x = 0 \tag{2.36}$$

$$\tilde{u}_y = -\eta v_\mathrm{k}, \tag{2.37}$$

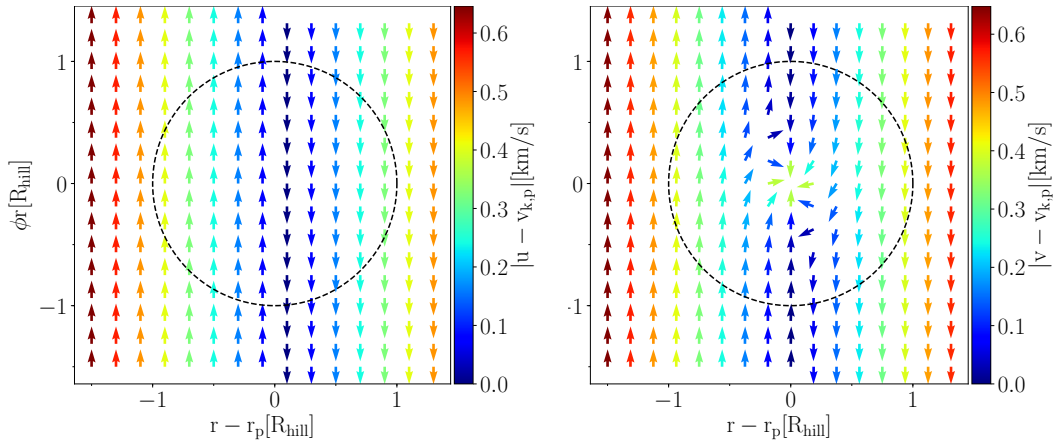

Figure 2.5: A first order approximation of the sub-Keplerian velocity field (left), and the terminal velocity field of cm-sized particles at 5 au, $\sim \tau = 10^{-2}$, (right). The dashed line corresponds to the hill sphere around the protoplanet, and the absolute velocity, relative to the Keplerian speed of the protoplanet, is shown in the color-map.

where $\tau = \Omega_p t_{f,d}$ is the stokes number for small particles. Note that the solution is divided into two terms, of which the first is the solution of a pure disc model as derived by Lambrechts & Johansen (2012); Nakagawa et al. (1986); Weidenschilling (1977), while the second term is the effect induced by the protoplanet. The resulting gas-flow and the terminal velocity field of cm-sized particles at 5 au are plotted in the left and right panel, respectively, in Figure 2.5. The linear flow around the protoplanet is an adequate approximation for the purpose of this work. However, divergences and caveats are further discussed in the following subsection.

2.3.2.1 Comparison with hydrodynamic gas flows

The velocity field of the gas, shown in Figure 2.5 (left), is a first order approximation and it is useful to compare it to hydrodynamic simulations (HD) in order to interpret the results.

Hydrodynamic simulations have shown complex velocity fields around protoplanets, e.g. Lambrechts & Lega (2017); Paardekooper et al. (2010); Baruteau & Masset (2008). An example of the mid-plane structure is shown in Figure 2.6, borrowed from Lambrechts & Lega (2017). The Keplerian streamlines, plotted in gray, are pulled towards the core as they pass the protoplanet. This is a second order effect that is neglected in my model. Furthermore, as the gas is pulled towards the protoplanet, it can cross the protoplanetary orbit and end up on so called horseshoe orbits, depicted in orange. Finally, there is an outflow of gas from the near centre, illustrated in white, which comes from vertically inflowing gas that is not included in my 2D approach.

The gray and the white streamlines in Figure 2.6 will always have a moderately accurate correspondence in Figure 2.5, even if the origin of the stream-lines are different. The major differences occur in the horizontal components near $x = 0$ which are completely

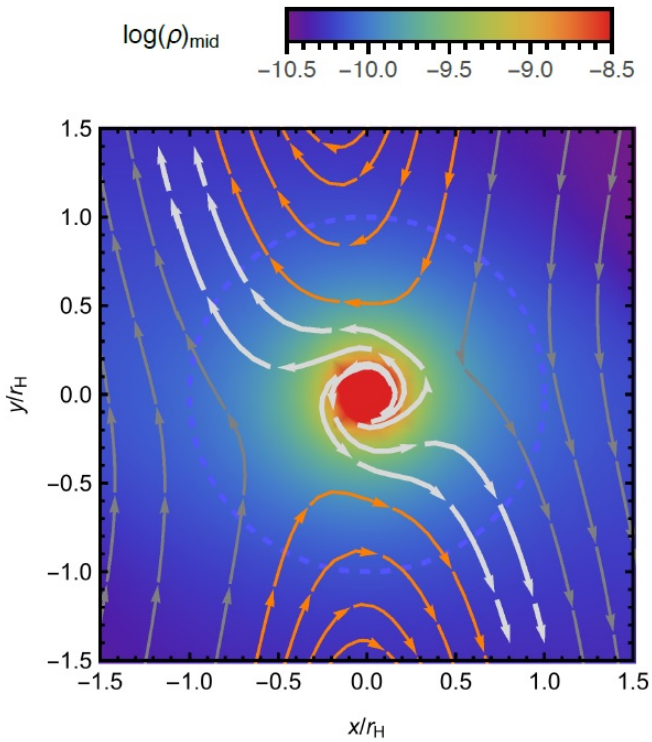

Figure 2.6: The mid-plane structure of the gas around a protoplanet as a result from hydrodynamic simulations by Lambrechts & Lega (2017). The background color corresponds to the logarithm of the density structure of the gas, the streamlines show the direction of the gas flow, and the Hill sphere has been plotted as a dashed line. The gray lines indicate the Keplerian dominated flow. In orange, the gas is pulled onto horseshoe orbits that cross the planetary orbit and effectively leave the shearing-box frame. The white stream lines correspond to vertically in-falling gas that spirals towards the core but ends up on two outflow channels. For further insight see Lambrechts & Lega (2017).

ignored in my model. As a consequence, the impact parameters (initial x-position) of the accreted material will be shifted towards $x_0 \approx 0$, rather than originating from $x_0 \approx 0.6 - 0.7\, R_{\mathrm{Hill}}$, which would be expected from Figure 2.6. Furthermore, in HD simulations, the gas rotates around the protoplanetary core, meaning that the particles will spend more time on spiralling orbits towards the core and have more time to ablate compared to my simulations. However, because the gas-flow mostly affects moderate to small particles $10^3 - 10^{-1}$ cm, which are expected to ablate on short time-scales (Brouwers et al. 2018), I do not expect the results to differ by a large margin compared to HD simulations.

An interesting scenario was pointed out by Popovas et al. (2018), where moderately large particles ablate enough material to become small and well coupled to the gas. These projectiles may consequently become locked on stream-lines of the gas which are directed away from the core; thus the accretion onto the core can be lowered due to ablation.

2.4 Destruction mechanisms

The focus of this work is the destruction of the in-falling solid material in protoplanetary envelopes. The mass deposition rate is set by sublimation, and fragmentation is included as a Collective Wake fragmentation model. This section presents the ablation and fragmentation model used in this work.

2.4.1 Ablation model

The surface of meteors gets heated from the net energy-flux onto the surface. In this case, the source-terms are friction and background radiation, while the sink-terms are the re-emitted black-body radiation and sublimations[7]. The main source and sink equations were introduced in Section 1.3.2, and the sum of Equation 1.2, 1.3, and 1.4 form the total net energy-flux onto the solid surface:

$$\sum \dot{E}_{\rm i} = \underbrace{\pi r_{\rm s}^2 \Lambda C_{\rm D} \frac{\rho_{\rm g} v^3}{2}}_{\text{Friction}} + \underbrace{4\pi r_{\rm s}^2 \epsilon \sigma_{\rm sb} \left(T_{\rm g}^4 - T_{\mathbb{S}}^4\right)}_{\text{Radiation}} + \underbrace{L_{\rm s} \frac{{\rm d}M}{{\rm d}t}}_{\text{sublimation}} . \tag{2.38}$$

The net energy flux can be related to the surface temperature through

$$C_{\rm v} M_{\mathbb{S}} \frac{dT_{\mathbb{S}}}{dt} = \sum \dot{E}_{\rm i}, \tag{2.39}$$

(D'Angelo & Podolak 2015), where $C_{\rm v}$ is the specific heat capacity for constant volume, a temperature dependent parameter, and $M_{\mathbb{S}}$ is the surface mass that is defined as

$$M_{\mathbb{S}} = \frac{4}{3}\pi \rho_{\rm s} \left[r_{\rm s}^3 - \left(r_{\rm s} - \delta\right)^3\right], \tag{2.40}$$

where $\rho_{\rm s}$ is the density of the particle, and δ is the surface thickness, defined as

$$\delta \equiv \min\left(r_{\rm s}, 0.3 \frac{K}{\sigma_{\rm sb} T_{\mathbb{S}}^3}\right), \tag{2.41}$$

where K is the thermal conductivity (D'Angelo & Podolak 2015). The latter min-function is due to the fact that δ can not exceed the radius of the particle. The sublimation rate is given by

$$\frac{dM}{dt} = 4\pi r_{\rm s}^2 v_{\rm th} (\rho_{\rm v} - \rho_{\rm s}), \tag{2.42}$$

Kimura et al. (2002), where a spherical surface area is assumed, $v_{\rm th}$ is the thermal velocity of the molecules given by a Maxwellian velocity distribution as

$$v_{\rm th} = \left(\frac{k_{\rm B} T}{2\pi \mu m_{\rm H}}.\right)^{1/2}, \tag{2.43}$$

[7] Also referred to as the latent cooling.

Here, k_{B} is the Boltzmann constant, ρ_{vap} and ρ_{sat} are the vapour and the saturated vapour densities, respectively. Note that these are related to the respective pressure correspondence through the ideal gas law. Hence, the rate at which particles leave the surface is set by the thermal velocity, and the density ratio between equilibrium and the current vapour densities determine the amount of transferred mass. μ is in this case the mean molecular weight of the species that is sublimating. I will make the further assumption that the vaporised material is quickly removed from the meteor surface. The vapour density can then be neglected, and the final expression is given by

$$\frac{dM}{dt} = -4\pi r_{\mathrm{s}}^2 \left(\frac{\mu m_{\mathrm{H}}}{2\pi k_{\mathrm{B}} T_{\mathbb{S}}} \right)^{1/2} P_{\mathrm{s}}(T_{\mathbb{S}}), \tag{2.44}$$

where the ideal gas law has been applied (Equation 2.7), and $P_{\mathrm{s}}(T_{\mathbb{S}})$ is calculated from Equation 2.12 or 2.13, depending on the material that is sublimating. Equation 2.44 holds as long as surface temperatures are lower than the critical temperature of the sublimating material, which are listen in Table 2.3. At the critical temperature, the molecules can not enter the liquid phase no matter how much the pressure is increased, and the sublimation becomes limited by the latent heat of sublimation, L_{s}, Podolak et al. (1988). At this point, the net energy-flux onto the surface vanishes and the temperature remains at the critical value. This requires an endothermic cooling rate that corresponds to a mass loss of

$$\frac{dM}{dt} = -\frac{1}{L_{\mathrm{s}}} \left[\pi r_{\mathrm{s}}^2 \Lambda C_{\mathrm{D}} \frac{\rho_{\mathrm{g}} v^3}{2} + 4\pi r_{\mathrm{s}}^2 \epsilon \sigma_{\mathrm{sb}} \left(T_{\mathrm{g}}^4 - T_{\mathrm{c}}^4 \right) \right], \tag{2.45}$$

as can be derived from Equation 2.39 (D'Angelo & Podolak 2015).

The ablation model described above has been used in recent work, and further been developed in some cases, e.g. Brouwers et al. (2018); Ronnet et al. (2017), where in the first, they implemented a further complex relation on the propagation of heat through the material and Λ; and in the latter, their results indicated that the equilibrium surface temperatures are quickly reached, where $\dot{T}_{\mathbb{S}} \equiv 0$. Hence, their energy-flux equation could be simplified to

$$0 = \rho_{\mathrm{g}} C_{\mathrm{D}} \Lambda \frac{v^3}{8} + \epsilon \sigma_{\mathrm{sb}} \left(T_{\mathrm{g}}^4 - T_{\mathbb{S}}^4 \right) - \frac{L_{\mathrm{s}}}{4\pi r_{\mathrm{s}}^2} \frac{dM}{dt}, \tag{2.46}$$

Initially using Equation 2.39 with the variables listed in Table 2.3, I found that the required time-steps to evolve the temperature were on the order of sub-seconds. The equilibrium temperature is thus quickly reached, and Equation 2.46 becomes the optimal choice in this work, which is used. Note that Equation 2.46 is highly non-linear, and has a strong dependence on the surface temperature through the mass deposition rate, given by Equation 2.44.

2.4.1.1 Sublimation time-scales

We can estimate the sublimation time-scales for a given surface temperature by using Equation 2.44. Considering a constant density of $1\,\mathrm{g\,cm^{-3}}$ for solids with radii of 10^{-1} –

Table 2.3: A summary of the parameters used to calculate the surface temperatures. The material parameters are corresponding to a mixture of rock and ice, used in the corresponding cited literatures: the thermal conductivity K, the latent heat of sublimation L_s, the specific heat capacity at constant volume C_v, the fraction of dissipated energy from the gas Λ, the emission and absorption coefficient ϵ, and the assumed particle density ρ_s. Furthermore, the table shows the internal strength scaling factor α, the nominal dynamical pressure limit $(\rho_g v^2)_{\mathrm{lim},0}$, and the critical temperatures of the considered species in Madhusudhan et al. (2014), where the silicates are assumed to behave as quartz. For clarity, the table shows the values used for the protoplanetary core-mass M_p, its density ρ_p, and the semi-major axes r_p; the nominal model is highlighted with brackets.

parameter	value	units	source
K	4×10^5	$[\mathrm{erg\,s^{-1}g^{-1}K^{-1}}]$	Podolak et al. (1988)
$L_s(H_2O)$	2.83×10^{10}	$[\mathrm{erg\,g^{-1}}]$	D'Angelo & Podolak (2015)
$L_s(SiO_2)$	8×10^{10}	$[\mathrm{erg\,g^{-1}}]$	D'Angelo & Podolak (2015)
$L_s(CO_2)$	5×10^9	$[\mathrm{erg\,g^{-1}}]$	Bryson et al. (1974)
C_v	1.17×10^7	$[\mathrm{erg\,g^{-1}K^{-1}}]$	D'Angelo & Podolak (2015)
Λ	1/4	-	D'Angelo & Podolak (2015)
ϵ	1	-	D'Angelo & Podolak (2015)
ρ_s	1	$[\mathrm{g\,cm^{-3}}]$	-
α	0.1	-	Register et al. (2017)
$(\rho_g v^2)_{\mathrm{lim},0}$	0.1	[MPa]	Benz & Asphaug (1999)
$T_c(CO)$	134.45	[K]	-
$T_c(CH_4)$	199.55	[K]	-
$T_c(CO_2)$	304.25	[K]	-
$T_c(H_2O)$	647	[K]	-
T_c(quartz)	4500	[K]	D'Angelo & Podolak (2015)
M_p	0.1, 0.5, 1.0, 5.0, (10), 50	$[M_\oplus]$	-
ρ_p	5.5	$[\mathrm{g\,cm^{-3}}]$	-
r_p	1, (5), 10, 50, 100	[au]	-

10^8 cm and by simply using the temperature range found in protoplanetary envelopes, the inverse of Equation 2.44 multiplied by the particle mass ($M/\dot{M}$) gives a sublimation time-scale which is plotted in Figure 2.7 for water and silicate. Since the saturated vapour-pressure is a steep function of the temperature, the sublimation can happen on small time-scales, on the order of seconds. However, note that Equation 2.44 only holds until the critical temperature is reached.

2.4.2 Fragmentation

A large variety of fragmentation criteria and models are used in the literature, e.g. Borovička & Spurný (1996); Register et al. (2017); Mordasini et al. (2006). In this work, a simple cut-in-half model is used, based on the Collective Wake approach described in Register et al. (2017). This model requires a dynamical pressure limit (internal strength), which is predefined for a given impactor, and determines the condition where the first breakup point occurs. Several other fragmentation models exist, as mentioned in Section 1.3.3. However, the Collective Wake model has proven to be able to describe the overall main structure in the light-curves of meteors (Register et al. 2017), hence it was chosen to give a reasonable and simple destruction scenario.

2.4.2.1 Initial breakup point

The limiting dynamical pressure is assumed to be a constant throughout this work, unless otherwise stated, set by the lower limit obtained by Benz & Asphaug (1999) for both rocky and icy bodies $(\rho_g v^2)_{\mathrm{lim},0} = 0.1\,\mathrm{MPa}$ (Figure 2.9). Nonetheless, an approximate fit to the data of Benz & Asphaug (1999) was also implemented in this work for comparison, given by

$$\log_{10}(\rho_g v^2)_{\mathrm{lim},0} = 7.96 - 0.34\log_{10}(r_s) \qquad \text{for} \quad r_s \leq 10^4\,\mathrm{cm} \tag{2.47}$$

$$\log_{10}(\rho_g v^2)_{\mathrm{lim},0} = 3.51 + 0.77\log_{10}(r_s) \qquad \text{for} \quad r_s > 10^4\,\mathrm{cm} \tag{2.48}$$

where the zero denotion stands for the initial breakup condition.

2.4.2.2 Collective Wake model

The initial fragmentation occurs once the predefined dynamical pressure limit of 0.1 MPa is reached. The main body will then break up into two fragments, each with half of the mass of the parent body, which are assumed spherical. The radius of each fragment can be calculated from

$$\rho_f \frac{4\pi R_f^3}{3} \equiv \frac{\rho_p}{2}\frac{4\pi R_p^3}{3} \tag{2.49}$$

where f and p denotes property of one fragment and the parent body, respectively. If the density is assumed to be the same for the fragment and the parent, the radius of the fragment is related to the parent radius as

$$R_f = 2^{-1/3} R_p \tag{2.50}$$

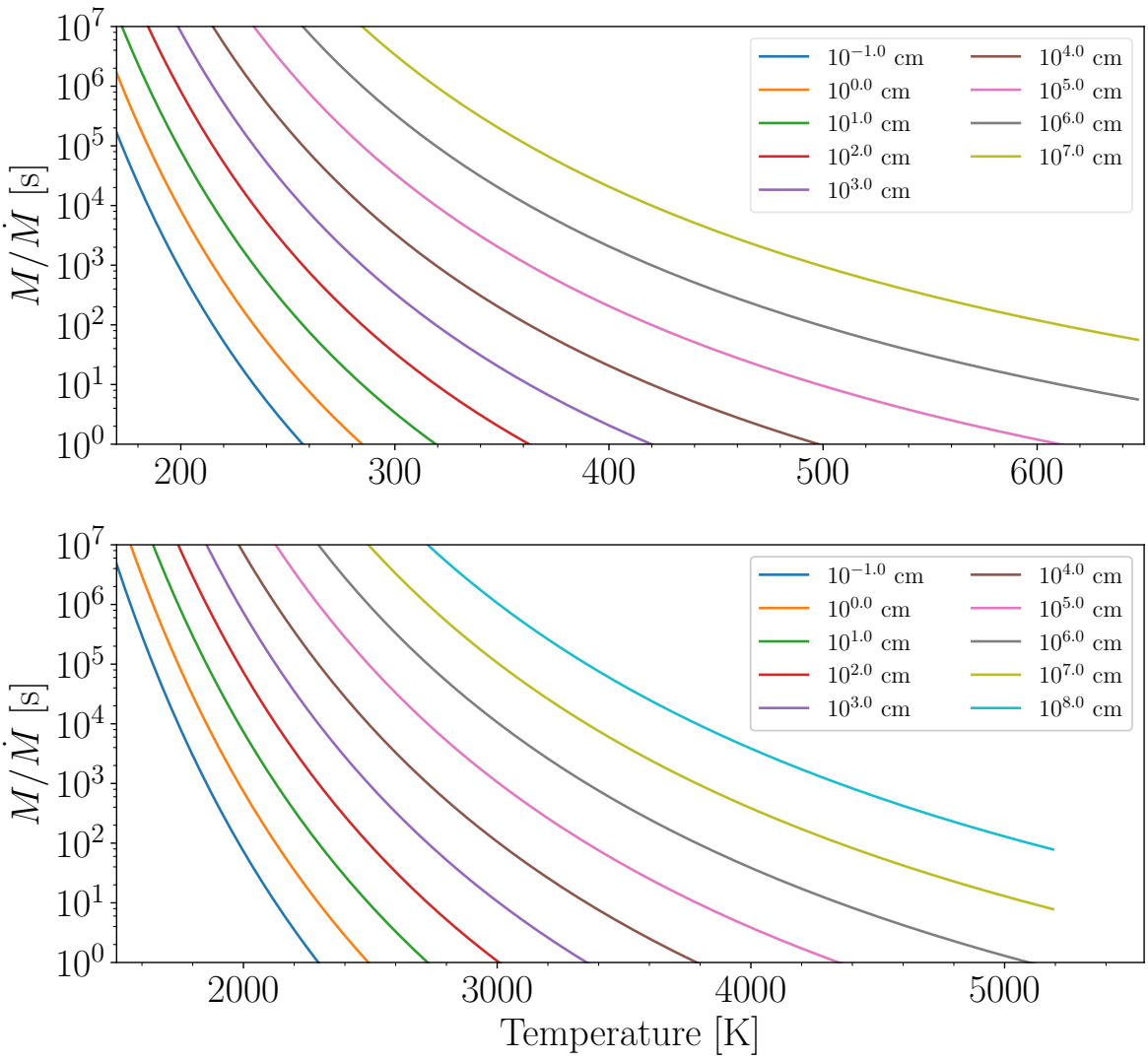

Figure 2.7: Sublimation time-scales of water ice (top), and forsterite (bottom) as a function of surface temperature. The density of the sublimating particles is set to unity. The individual particle sizes are labelled in the plots, with the smallest particles being located towards the left in the figure, and the larger the particle, the higher temperatures are needed to fully sublimate within the same time-scale.

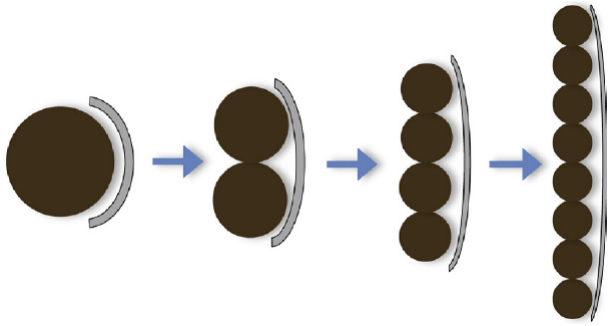

Figure 2.8: The collective wake fragmentation approach where the parent bodies split into two fragments, each with half of the mass of the parent (Register et al. 2017).

Each time the impactor is fragmented, the number of fragments double as shown in Figure 2.8. Thus, the effective area of the fragments is given by

$$A_{\rm eff} = 2 \cdot 4\pi R_{\rm f}^2 = 2^{1/3} 4\pi R_{\rm p}^2 \tag{2.51}$$

where the factor of 2 comes from the fact that the parent splits into two fragments. The effective area of the fragments correspond to a super particle with a radius of

$$R_{\rm eff} = \left(\frac{A_{\rm eff}}{4\pi}\right)^{1/2} = 2^{1/6} R_{\rm p} \tag{2.52}$$

If the two created fragments are further reaching their fragmentation limits, the radius of the second generation fragments, $f2$, follow according to Equation 2.50 that

$$R_{\rm f2} = 2^{-1/3} R_{\rm f} = 2^{-2/3} R_{\rm p}, \tag{2.53}$$

which can be written in a general way as a function of the number of fragmentations, i

$$R_{\rm f,i} = 2^{-i/3} R_{\rm p}. \tag{2.54}$$

The sum of the area of all fragments is then given by

$$A_{\rm eff,i} = 2^i 4\pi R_{\rm f,i}^2 = 2^{i/3} 4\pi R_{\rm p}^2 \tag{2.55}$$

Finally, the effective radius is given by Equation 2.52, thus

$$R_{\rm eff,i} = 2^{i/6} R_{\rm p}, \tag{2.56}$$

where $R_{\rm eff,i}$ is the effective radius of a super-particle that contains the fragments under a 'Collective Wake' (Register et al. 2017), i is the number of times that the particle has reached a fragmentation limit, and $R_{\rm p}$ is the initial radius of the particle in question. Consequently, the fragmentation event does not include any mass loss. However, the

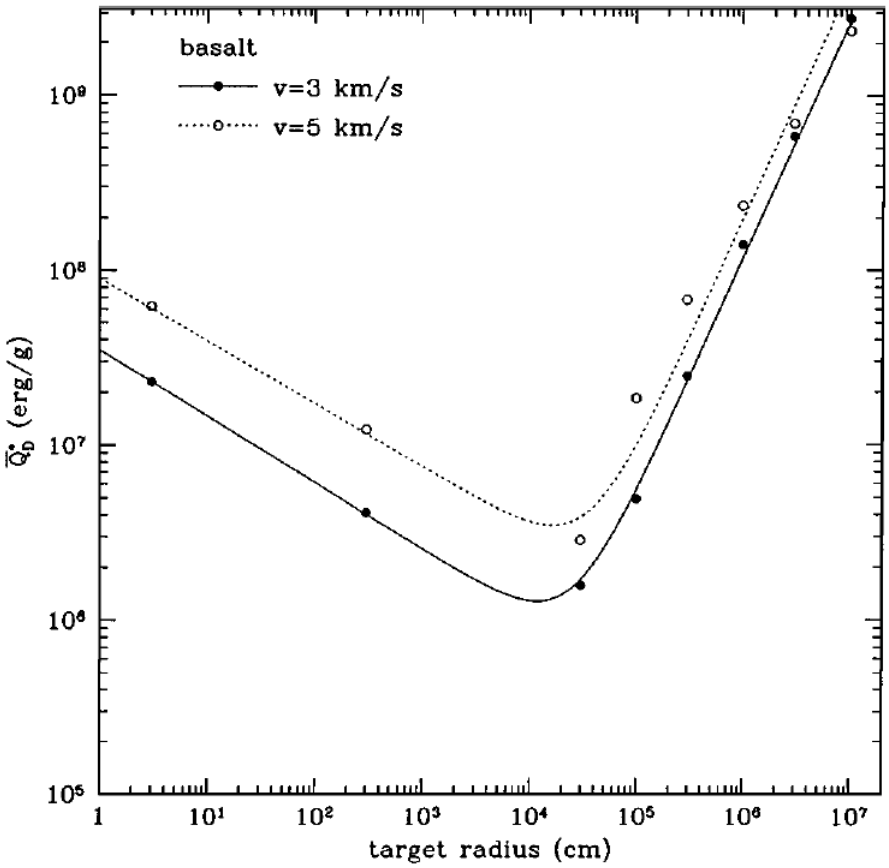

Figure 2.9: The internal strength of basaltic rocks, impacting with a velocity of 3 and $5\,\mathrm{km\,s^{-1}}$ in a SPH approach Benz & Asphaug (1999).

effective radius will result in a stronger drag-force as well as increasing the ablation rate, as it is to be used as the particle size in the presented equations in this work.

Furthermore, for each fragmentation, the individual fragments will have greater internal strength compared to the parent body. The scaling of the internal strength can be estimated as

$$(\rho_\mathrm{g} v^2)_\mathrm{lim,f} = (\rho_\mathrm{g} v^2)_\mathrm{lim,p} Q^\alpha, \tag{2.57}$$

where Q is the mass-ratio between the parent and the fragment, and α is a scaling parameter on the order of $\alpha = 10^{-1}$ Register et al. (2017), which is assumed throughout this project.

2.5 Simulations

This section describes the initial conditions and the numerical methods used. Derivations are not included, and for detailed descriptions of the exact numerical approaches, the reader is referred to the literature.

2.5.1 Numerical methods

The code is based on the Runge-Kutta approach by Dormand & Prince (1980), and the time-step is set by a fraction of the minimum value between the gravitational scattering time $t_{\rm g}$, the friction time $t_{\rm f}$ (Section 2.3.1.1), and the radial distance from the protoplanet over the particle velocity $t_{\rm inv} = R/v_{\rm s}$:

$$\delta t = \frac{1}{5}\min\big(t_{\rm g}, t_{\rm f}, t_{\rm inv}\big), \tag{2.58}$$

where the gravitational scattering time is defined as

$$t_{\rm g} = \sqrt{\frac{r^3}{GM_{\rm p}}}. \tag{2.59}$$

Consequently, the time-steps scale with the distance from the core, such that the trajectories are resolved at the closest approach. These time-steps have shown to be enough to calculate the temperature, as well as the sublimation rates. However, a lower limit of $\delta t = 1\,{\rm s}$ was set in order to prevent long simulation times. These cases correspond to when small particles settle towards the core with low velocities, which can safely be extrapolated afterwards. For the smallest particles, e.g. $10^{-1} - 10^{0}\,{\rm cm}$ at $5\,{\rm au}$, that follow the criteria of Equation 2.31, the trajectories are set by the terminal velocities (Section 2.3.2), which reduces the simulation time significantly.

Finally, the equilibrium surface temperature (Section 2.4.1) is described by a highly non-linear equation and is hence solved numerically by the means of the bisection method. The outer and inner boundary is in this case chosen to be the initial surface temperature (the local disc temperature if outside of the envelope) $\pm 10^3\,{\rm K}$, where negative values are omitted for obvious reasons. The large range of temperatures is due to the fact that, e.g. once the endothermic cooling is turned off, when the water has fully vaporised, the temperature gradients may increase significantly.

2.5.2 Initial conditions

As will be seen in Chapter 3, the initial positions of the particles matter. The initial positions are kept the same in all simulations unless otherwise mentioned. The particles are located along the top and the bottom of the shearing-box, at $y = \pm 3\,R_{\rm Hill}$. This azimuthal distance ensure that they are in disc-like conditions, and their initial velocities can be approximated by the first terms in Equation 2.34 and 2.35, respectively. Furthermore, in order to avoid confusing interpretations of the impact parameters (initial x-positions), the global pressure gradient of the disc is set to zero – thus the radial drift of the dust is neglected[8]. As this work focuses on single encounters between the impactors and protoplanets, the additional complexity of global radial drift will essentially make it difficult to

[8]With radial drift, the particles at larger semi-major axis than the protoplanet can drift out from the shearing-box frame, and later re-enter the frame when they have drifted past the protoplanetary orbit. This would yield the same result as if the particle was introduced at the re-entry coordinates, complicating the interpretation of the results.

quantify particle properties and accretion rates as a function of initial positions. Finally, the particle radii included in this work are

$$r_{\rm s} = [10^{-1}, 10^{0}, 10^{1} ... - 10^{8}]\,{\rm cm},$$

where for each size, 120 particles are evenly distributed in the impact parameter-range between $x_0 = -3\,R_{\rm Hill}$ and $3\,R_{\rm Hill}$. For the nominal model, $r_{\rm p} = 5\,{\rm au}$, the corresponding Stokes number for each particle size is on the order of

$$\tau \sim [10^{-3}, 10^{-2}, .., 10^{0}, 10^{2}, 10^{4}, .., 10^{10}, 10^{12}].$$

Note that once the particles become large, the Stokes number will scale non-linearly, hence the different scaling-factor above $\tau = 1$.

2.5.3 Accretion rates

Because of the even distribution of impact parameters, each particle corresponds to a mass-flow through a channel with a width

$$\delta x = \frac{6\,R_{\rm Hill}}{120}, \tag{2.60}$$

and an accretion rate onto the protoplanet, calculated as

$$\dot{M}_{\rm p,i} = 0.01\Sigma_{\rm g}\,\delta x\,v_{\rm i}\,(1 - f_{\rm i}). \tag{2.61}$$

Here, the dust is assumed to be accreted from the full dust scale-height in the disc, and the dust column-density is set to one percent of the gas column-density in a MMSN. $v_{\rm i}$ is the initial velocity of the particle, assuming that the mass-flow is constant, and $f_{\rm i}$ is the ratio of the final to the initial particle mass after the encounter. For example, in case of full ablation or accretion by directly hitting the protoplanetary core, $f_{\rm i} = 0$, and the corresponding channel becomes an efficient accretion source. The total accretion rate, where all the dust in the MMSN is assumed to be incorporated into a one particle size population, is given by the sum the accretion-channels for the particles

$$\dot{M}_{\rm p} = 0.01\Sigma_{\rm g}\,\delta x \sum_{\rm i} v_{\rm i}\,(1 - f_{\rm i}). \tag{2.62}$$

Finally, to calculate the accretion rate due to all particle sizes, a distribution of mass between the populations has to be assumed. In this work, I assume a dust column-density of $0.01\Sigma_{\rm g}$ in each size-bin. As 10 particle sizes are considered, the total dust to gas ratio when all particles are accounted for corresponds to 0.1.

2.5.3.1 Hill accretion

Previously work has shown that the particles that are most efficiently accreted onto protoplanets are those with a Stokes number of $\tau \sim 1$ (Section 2.3.1.1), e.g. Lambrechts & Johansen (2012). For the nominal model of this work, these particles are about one meter in size. The accretion rate can be written as

$$\dot{M}_{\rm p} = 2 r_{\rm d}\, \Sigma_{\rm d} v_{\rm d} \tag{2.63}$$

where $r_{\rm d}$ is the effective radius from which the material is accreted, $v_{\rm d} = (3/2)\Omega_p\, r_{\rm d}$ is the Keplerian speed at a distance $r_{\rm d}$ from the protoplanet, and $\Sigma_{\rm d}$ is the dust column-density of the disc. The case of $\tau = 1$ corresponds to when the friction-time is comparable to the gravitational crossing-time, e.g.

$$t_{\rm f} = \frac{\Delta\, v}{g} = (3/2)\Omega r_{\rm d} \frac{r_{\rm d}^2}{G M_{\rm p}} \tag{2.64}$$

where $\Delta\, v$ is the relative velocity between the protoplanet and the particle (assumed to be the Keplerian speed at a distance $r_{\rm d}$), and g is the gravitational acceleration from the protoplanet. Using the Stokes number for small particles (Equation 2.28) it can be shown that

$$r_{\rm d} = 3^{1/3} R_{\rm Hill} \tau^{1/3}. \tag{2.65}$$

Thus, for $\tau \sim 1$, the particles are expected to accrete from the whole Hill radius, which is the efficient Hill accretion regime (Lambrechts & Johansen 2012). Equation 2.63 can further be used to derive the scaling of the Hill accretion regime as

$$\dot{M}_{\rm p} \propto \tau^{2/3}, \quad \dot{M}_{\rm p} \propto r_{\rm p}^{-1}, \quad \& \quad \dot{M}_{\rm p} \propto M_{\rm p}^{2/3} \tag{2.66}$$

which are useful comparisons when analysing accretion rates onto protoplanets, and will be used in the Chapter 3.

2.5.3.2 Gravitational focusing

When particles are large enough, such that $\tau \gg 1$, the drag become negligible, and the probability for planetesimals to get accreted is set by the gravitational cross-section of the protoplanet. Since the energy of an incoming planetesimal has to equal the final energy that the impactor would have at the surface of the planetary core, the gravitational cross-section can be described as

$$\sigma_{\rm grav} = \pi R_p^2 \left(1 + \frac{v_{\rm esc}^2}{v_\infty^2}\right) \tag{2.67}$$

(Hughes & Boley 2017), where R_p is the radius of the protoplanet, $v_{\rm esc}$ is the escape speed, and v_∞ is the initial velocity of the planetesimals in the disc. Assuming that the incoming planetesimals approach the protoplanet at the Hill speed, the effective gravitational radius can, for the nominal model, be estimated to be

$$R_{\rm grav} = R_{\rm p}\left(1 + \frac{2GM_{\rm p}}{R_{\rm p}(3/2\,\Omega R_{\rm Hill})^2}\right)^{1/2} = R_{\rm p}\left(1 + \frac{2^3}{3}\frac{R_{\rm Hill}}{R_{\rm p}}\right)^{1/2} \sim 0.05\, R_{\rm Hill}. \tag{2.68}$$

Because the planetesimals are not strongly affected by drag, it is difficult for them to fall within the gravitational cross-section, hence they get efficiently scattered. Consequently, the planetesimal accretion is expected to be lower than the Hill accretion.

Chapter 3

Results

In this chapter, I present the results of my work. By combining the equation of motion in a shearing-box with a model for particle destruction, I have been able to analyse the fate of pebbles and planetesimals entering a protoplanetary envelope, and the effect on planetary growth. This chapter summarises the results, beginning with the different trajectory dynamics obtained with and without ablation (Section 3.1), followed by the accretion windows that are discussed in Section 3.2. The evolution of the surface temperatures of the impactors is presented in Section 3.3. The particle velocity distribution and dynamical pressure are brought up in Section 3.4. In Section 3.5, the trajectories of the particles are connected to the ablation rates. Section 3.6 is finally dedicated to the accretion rates onto protoplanetary cores. The classical core accretion scenario (CCA), where particle destruction is not included, is compared to protoplanetary meteor accretion (PMA), where the destruction is accounted for. As a final remark, if otherwise not mentioned, the results regard the nominal model of this work, where the core mass corresponds to $10\,M_{\oplus}$ that is located at 5 au.

3.1 Trajectories and dynamics

The physics behind the particle trajectories is determined by the gravitational force and the gas-drag. However, because the gravitational potential is the same for all particle sizes considered here, the gas-drag alone is responsible for the differences between the size populations. It is hence reasonable to divide the results into groups depending on the Stokes number which quantifies the strength of the coupling between the particles and the gas (Section 2.3.1.1). When $\tau \ll 1$ the coupling to the gas is strong and the trajectories are expected to trace the gas-flow that is shown in Figure 2.5. If $\tau \sim 1$, the drag-force from the gas is acting on the same time-scales as the crossing-time of the particles over the Hill-sphere. The particles are in this case expected to experience the maximal loss of angular momentum to the gas during the passing-time. When $\tau \gg 1$, the friction times are long in comparison to the crossing-time, and the trajectories become dominated by gravity. This section discusses the results obtained for each particle size and compares the CCA to the PMA. A summary can be found at the end of the section.

3.1.1 Stokes number < 1

The trajectories of the particles with a Stokes number less than unity have been plotted in Figure 3.1. For clarity, only the trajectories which lead to some form of mass deposition to the protoplanet are plotted. The left and the right columns correspond to the CCA and the PMA results, respectively. For each sub-figure, the x- and y-axis are the local approximations of the radial and the azimuthal disc components (Section 2.3). Thus, the particles on the right side of the protoplanet enter the shearing-box frame at $y = 3\,R_{\mathrm{Hill}}$, while the particles on the left enter the frame at $y = -3\,R_{\mathrm{Hill}}$. Three spherical regions around the protoplanet have further been marked in the sub-figures: the Hill-sphere (black dashed), the water ice line (orange dashed), and the silicate rock-line – calculated based on the properties of forsterite (red dot). Each trajectory corresponds to an accretion channel that is weighted by the fraction of mass of the particle that is transferred to the protoplanet. Consequently, only the particles that lead to direct impact yield the non-zero accretion channels in the CCA, while for the PMA, all of the trajectories that enter the protoplanetary envelope have shown to deposit some mass. The range of impact parameters that span the accretion channels is furthermore defined as the accretion window. Finally, an inset is shown for each sub-plot to highlight the innermost trajectories. The particles falling under the criterion of $\tau < 1$ are the 10^{-1} (top), 10^{0} (mid), and 10^{1} cm particles (bot), respectively.

At the top of Figure 3.1, the trajectories are essentially mapping the background gas-flow due to their strong coupling to the gas as discussed in Section 2.3.2. Consequently, only the particles close to the core are pulled out from the gas-flow and further redirected towards the centre by the gravitational force, as can be seen in the inset. Note that in the CCA, six particles are pulled out from the gas to be accreted, while in the PMA, only four particles are directed towards the core. The same phenomenon can be seen in the mid panel, where 20 particles of 10^{0} cm in size are hitting the core in the CCA while 18 are fully accreted in the PMA. Treating the impactors as meteors can thus result in the loss of fully accreted particles. This is similar to the results of a recent study by Popovas et al. (2018), who argued that the coupling between the gas and the particles grows stronger when they are made smaller due to ablation. This scenario is consistent with the scaling of the friction-time in the Epstein regime where $t_f \propto r_{\mathrm{s}}$ (Section 2.3.1.1). The ablating particles decrease their radii, hence the friction-time, and the drag-force overcomes the gravitational pull such that the particles can escape full accretion.

In the mid and the bottom panel of Figure 3.1, the 10^{0} and 10^{1} cm particles are shown, respectively. As the particle size grows, so does the number of fully accreted particles in both the CCA and the PMA. This is a consequence of the positive correlation between the particle size and the friction-time (Section 2.3.1.1). As the friction-time increases towards the crossing-time of the Hill-sphere, the loss of angular momentum increases and the particles fall towards the core more efficiently. Notably, in the case of 10^{1} cm, the range of impact parameters that result in full accretion has increased to about one Hill radius, hence, Hill accretion is expected (Section 2.5.3).

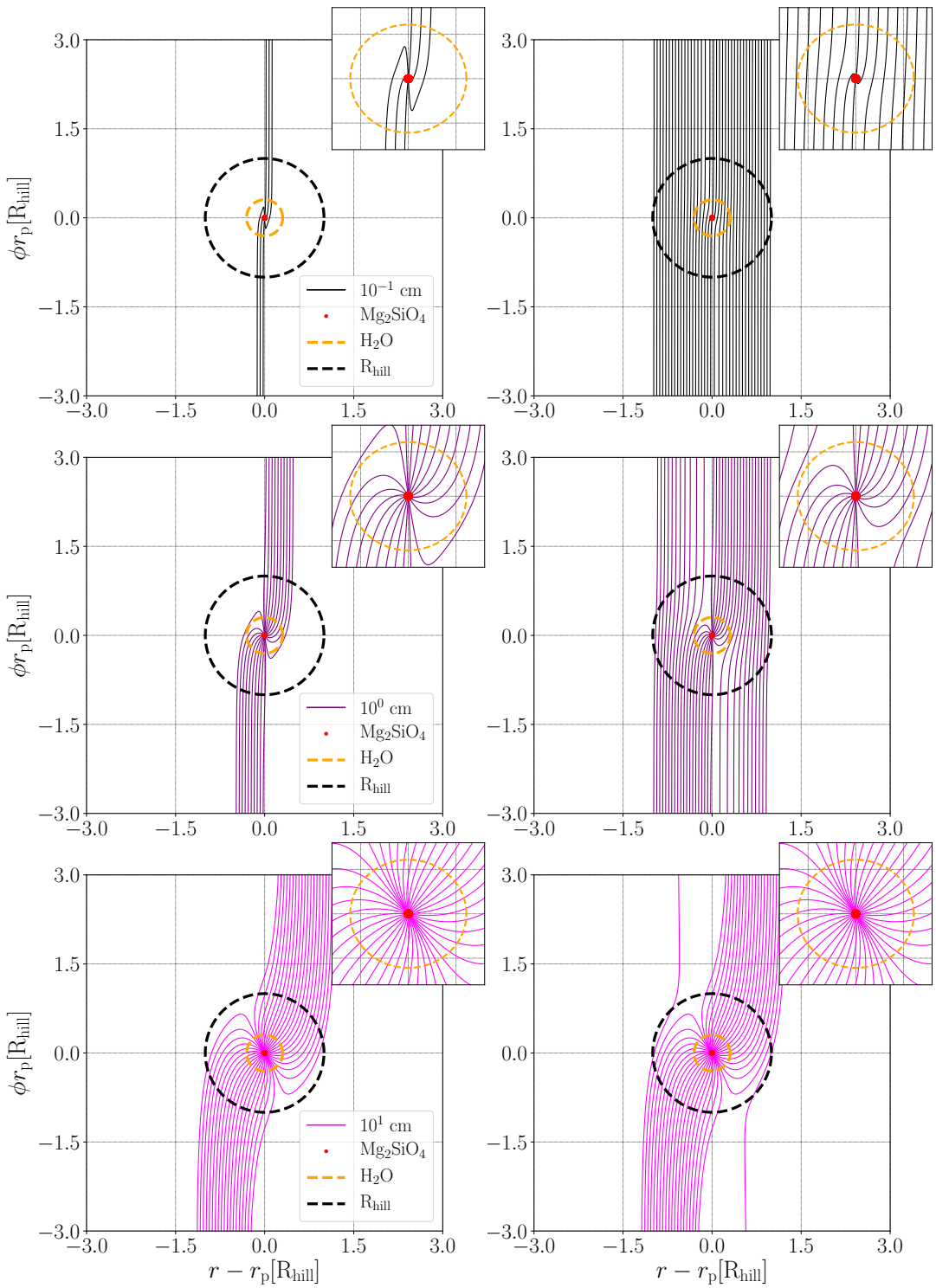

Figure 3.1: The trajectories surrounding a protoplanet with a core mass of 10 $M_\oplus$, located at 5 au, where the particles deposit at least some of their mass. The left and right panels correspond to the CCA and the PMA scenarios, respectively. The Stokes number are $\sim 10^{-3}$, 10^{-2}, and 10^{-1} (top to bottom), and the particle size and the respective Hill radius and condensation-lines are labelled according to the legend.

Furthermore, the impact parameters of the 10^1 cm particles are shifted away from the protoplanetary orbit, e.g. $x_0 = 0$. When the particles cross the orbit of the protoplanet before entering the Hill-sphere, their trajectories are still dominated by the stellar tide. Consequently, the particles are falling onto Keplerian orbits that are directed away from the core[1]. The PMA is in this case essentially the same as for the CCA. In comparison to the 10^{-1} and 10^0 cm case, where the number ratio of mass depositing particles between the PMA and the CCA is large, the number ratio of mass depositing particles for 10^1 cm is close to unity.

3.1.2 Stokes number ~ 1

The 10^2 cm size particles correspond to a Stokes number of $\tau \sim 1$ and experience the full headwind from the gas with maximal loss of angular momentum. Their trajectories have been plotted for the CCA and the PMA in Figure 3.2, where the reader is directed to the first paragraph of Section 3.1.1 for details regarding the figure.

Similarly to the 10^1 cm particles (Figure 3.1), the trajectories of the 10^2 cm particles are strongly bent towards the core from higher and lower impact parameters because of the positive correlation between the particle size and the friction-time. Similar to the 10^1 cm particles, the accretion window for 10^2 cm is well approximated by the Hill radius, and Hill accretion is expected (Section 2.5.3). Furthermore, note that two (one) particles in the PMA scenario are scattered through the envelope from the higher (lower) impact parameters, respectively. These particles only glance the envelope in a region where the temperatures are close to that of the local disc (Section 2.2). In terms of accretion rates, the difference between the PMA and CCA are thus small. Noticeably, the 10^2 cm impactors swirl around the protoplanet before they are accreted which can bee seen in the insets. This is a result of their angular momentum being robbed by the gas-drag. The available time to ablate before impacting the core is thus slightly increased – an important detail when asking if the matter is accreted in gaseous or solid form.

3.1.3 Stokes number > 1

Once the particles have a stokes number $\tau > 1$, the gas-drag acts on time-scales that are greater than the crossing-time, and the trajectories are predominantly determined by the gravitational force (Section 2.3.1.1). The gravitational cross-sectional area is on the order of a few percent of the Hill radius (Section 2.5.3) and the number of particles that are fully accreted is expected to drop compared to the case of Hill accretion which was observed for the 10^1 and 10^2 cm particles (Section 3.1.1 & 3.1.2). In Figure 3.3, the trajectories of the particles of 10^3 (top), 10^4 (mid), and 10^5 cm in size (bottom) are shown, respectively, where the details regarding the figure are presented in the first paragraph of Section 3.1.1.

[1]In Appendix A.1, all particle trajectories are shown, indicating that the particles with small impact parameters end up on horseshoe-like orbits as discussed in Section 2.3.2.1. However, note that the gas is still approximated by a linear flow.

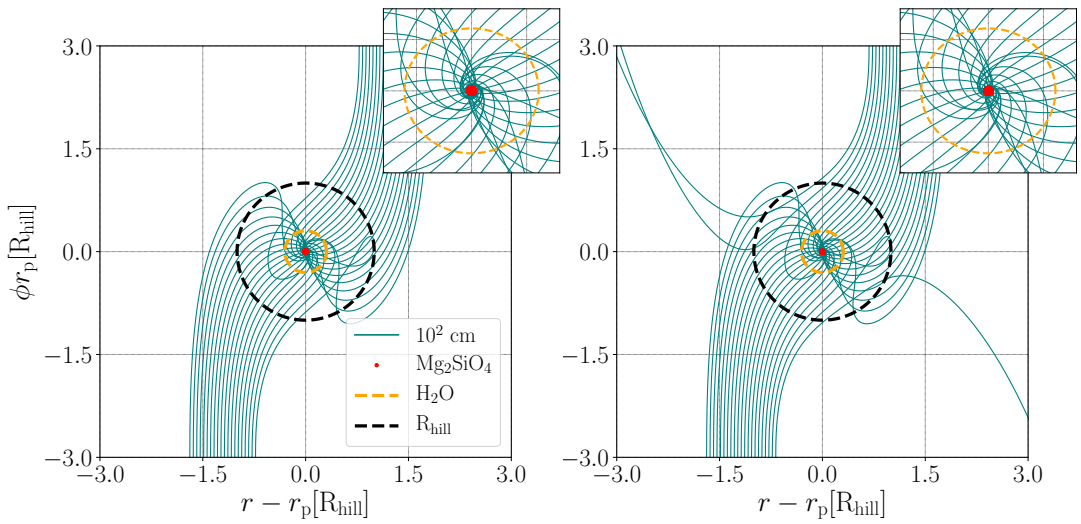

Figure 3.2: The same plot as Figure 3.1 but with particles of Stokes number $\tau \sim 1$. Both the CCA (left) and the PMA (right) show the efficient Hill accretion of these particles that are most affected by gas-drag.

For particles with sizes of 10^3 cm (top), the drag is still weakly operating, yielding a continuous accretion window. However, as the particle size is increased to 10^4 and 10^5 cm, the number of accreted particles strongly decrease which is most clearly visible in the CCA (left). For the PMA, the cross-section to undergo at least some ablation is still set by the Hill-region. Nonetheless, the scattering frequency has increased significantly in comparison to the particles with lower Stokes number. The accretion windows become chaotic in the sense that a small change in the initial conditions has a strong effect on the final outcome.

A feature of interest is the apparent in-spiralling pattern that the particles follow before falling to the core, as can be seen more clearly in the left column of Figure 3.3. Since the density of the gas is increasing towards the protoplanetary core, the gas-drag is most efficient near the core surface. Consequently, the particles can be slowed down at their pericenter passage and lose angular momentum. However, because the planetesimals are not as strongly affected by the gas-drag as the pebbles, several scattering events are required before they lose enough momentum to fall towards the core. Once the planetesimals have entered such long lasting in-spiralling orbits, they are said to be captured by the protoplanet. The captured particles will during the in-spiralling time ablate their material in the PMA and become smaller and more affected by the gas-drag, speeding up the in-spiralling process in comparison to the CCA. However, the additional time spent on in-spiralling orbits allows for larger particles to fully ablate in the envelope in contrast to simulations of central impacts used in previous studies.

Finally, the particles with sizes of 10^6, 10^7, and 10^8 cm are plotted in Figure 3.4. In the case of 10^6 and 10^7 cm particles, the in-spiralling patterns are present, meaning that the particles are still able to be captured. However, for the 10^6 and 10^7 cm particles, only six and three particles, respectively, were lucky enough to get accreted.

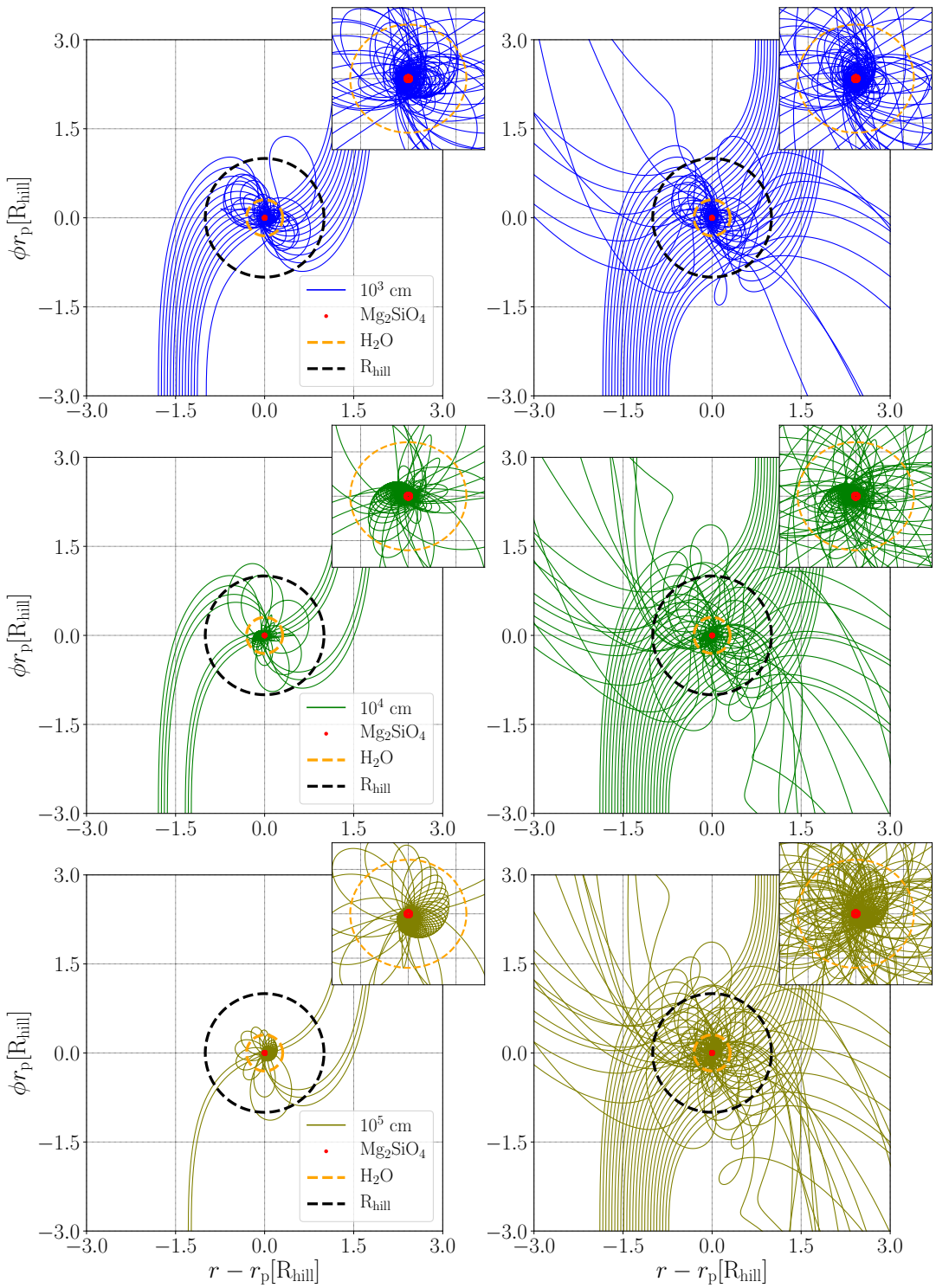

Figure 3.3: The same plot as in Figure 3.1, but for small planetesimals with Stokes number of $\tau \sim 10^2$, 10^4, and 10^6 (top to bottom). For details regarding the structure of the figure see first paragraph in Section 3.1.1.

On the other hand, the PMA continues to follow the trend of increasing number of scattering events through the envelope as was seen for the smaller planetesimals (Figure 3.3). The increased number of scatterings and the lower number of fully accreted particles can be explained by the increased friction-times which makes it more difficult to capture the planetesimals. At a size of 10^8 cm, only one particle is accreted in the CCA (bottom left). Nonetheless, the particle was lucky enough to fall within the gravitational cross-section (Section 2.5.3), and no gradual loss of angular momentum on in-spiralling orbits is observed.

3.1.4 Summary on trajectories

In this section, the trajectories of the particles, ranging form 10^{-1} to 10^8 cm in size are summarised. In order to remain general, both the size and the Stokes number of the particles are stated. This is because the behaviour of the particles is depending on the interplay between both the properties of the gas and that of the particles (Section 3.1). Nonetheless, the particle sizes are accurate in the case of a protoplanet located at 5 au in a MMSN.

- Particles on the order of $10^{-1} - 10^0$ cm ($\tau \sim 10^{-3}$ to 10^{-2}) have small accretion windows because they are strongly coupled to the gas-flow. Thus they need to pass the core at small distances for the gravity to be able to pull them out from the gas-flow. Ablation of these particles leads to a decreasing friction-time, such that the particles that would have been accreted in the CCA instead drift away from the protoplanetary core with the gas. Lastly, the number of particles that deposit mass in the PMA is much larger in comparison to the CCA model.

- For particles of size $10^1 - 10^2$ cm ($\tau \sim 10^{-1}$ to 10^0), the Hill accretion is observed. These particles lose their angular momentum efficiently due to gas-drag because the friction-times are comparable to the crossing-time over the Hill-sphere. Furthermore, the number of mass depositing particles is similar between the PMA and the CCA, thus Hill accretion is expected in both cases.

- For the planetesimals with sizes of $10^3 - 10^8$ cm ($\tau \sim 10^2$ to 10^{12}), the accretion windows become chaotic as the trajectories are dominated by gravity. Because the gravitational crossing-section is small in comparison to the Hill radius, planetesimal-scattering, away from the protoplanet, dominates the final outcomes. Nonetheless, planetesimals can in rare cases be captured if they come close enough to the core that the gas-drag can rob a fraction of their angular momentum. If the planetesimals are captured, they spiral towards the core, a process that takes more time compared to central impacts. This opens for discussion whether they have time to fully ablate or if they reach the core.

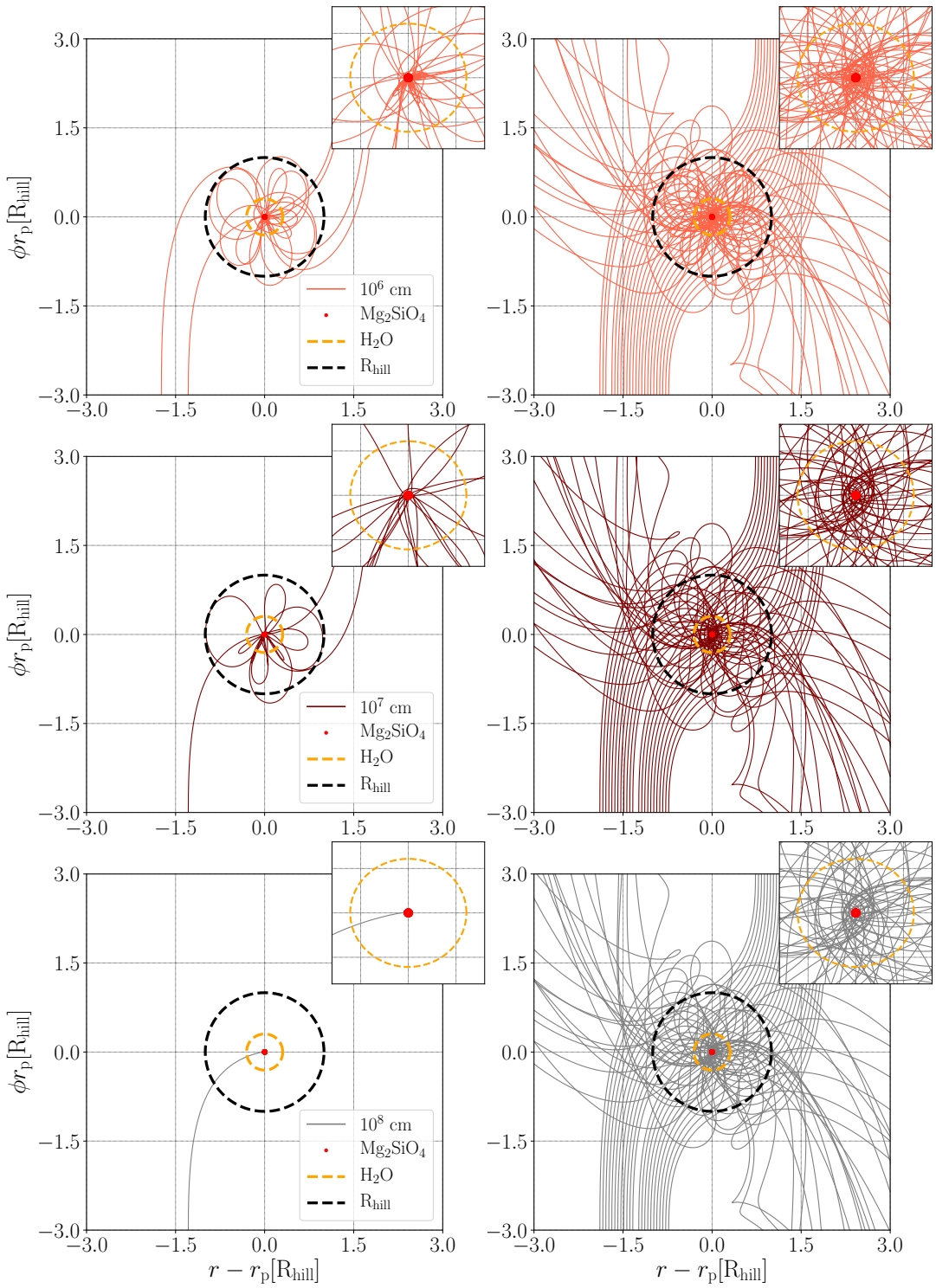

Figure 3.4: Same plot as in Figure 3.1, for planetesimals above 1 km with Stokes number of $\tau \sim 10^8$, 10^{10}, and 10^{12} (top to bottom). For details regarding the structure of the figure see first paragraph in Section 3.1.1.

3.2 Accretion windows

In the previous section, I showed that the number of mass depositing particles is larger when the encountering solids are treated as meteors in comparison to the classical core accretion. This section is dedicated to the mass deposition of the individual size-populations. It is important to understand how much mass is lost by the individual particles as it provides an estimate for the efficiency of the respective accretion channels, thus also for the time-scales over which protoplanets grow. By further comparing the PMA and the CCA models, I evaluate the importance of particle destruction in the envelopes.

To quantify the mass deposition, I create mass-window diagrams, which show the final mass of the solids after the encounter as a function of the impact parameter. In Figure 3.5, the mass-window diagram from the PMA simulations is shown for the nominal parameters. Here, each sub-plot correspond to the particle size denoted in the legend. To understand the diagram, points located at $\Delta M_{\rm s} = 0$ correspond to solids that were fully accreted, and for $\Delta M_{\rm s} = 1$ no mass was deposited. Furthermore, the initial water-mass fraction of the impactors has been plotted as a horizontal dashed line, where points that fall on this line are interpreted as particles that lost their water content.

For the 10^{-1} cm particles (upper left), the mass deposition region has a width of one Hill radius. However, full accretion only occurs within a fraction of the Hill radius, where $|x| < 0.1\,R_{\rm Hill}$. For larger impact parameters, the particles lose their water content through sublimation. Towards the edges of the accretion window, the water deposition decreases as the closest distance between the particles and the protoplanet increases, resulting in a wing-like structure. To a lesser extent, the wing-like structure remains present if the particle size is increased to 10^{0} cm (upper right). Thus, for the two smallest particle sizes considered, the ablation gives a weighting factor over the accretion window. For comparison, Figure 3.6 shows the same mass-window diagram but in the case of the CCA model. Notably, no wing-like structure is obtained for the 10^{-1} and 10^{0} cm particles, and the accretion window of the first mentioned has a width of $|x| = 0.15\,R_{\rm Hill}$. It is thus apparent that the escape, from full accretion, of two 10^{-1} and 10^{0} cm particles, respectively, (Section 3.1.1), is due to ablation which strengthened the coupling between the particles and the gas. However, the escaping particles had impact parameters at the outer edge of the regime where particles were 'fully accreted' (Figure 3.5). The accretion window extends further out in the PMA model, beyond $|x| = 0.15\,R_{\rm Hill}$, where a drying zone for the pebbles is located, acting as a water-vapour deposition source to the protoplanet.

In the Hill accretion regime, for $10^{1} - 10^{2}$ cm particles (second top, Figure 3.5), all the impactors are fully accreted, with well defined accretion windows. The same result is obtained in the CCA model (second top, Figure 3.6). At this point the mass-window diagrams do not differ between vapour and solid accretion. However, the total accretion for both the PMA and the CCA are here expected to follow the efficient Hill accretion (Section 2.5.3).

For the larger planetesimals ($r_{\rm s} \geq 10^{3}$ cm), we notice that the accretion windows becomes less well defined, and eventually turn chaotic as the particle size increases. The

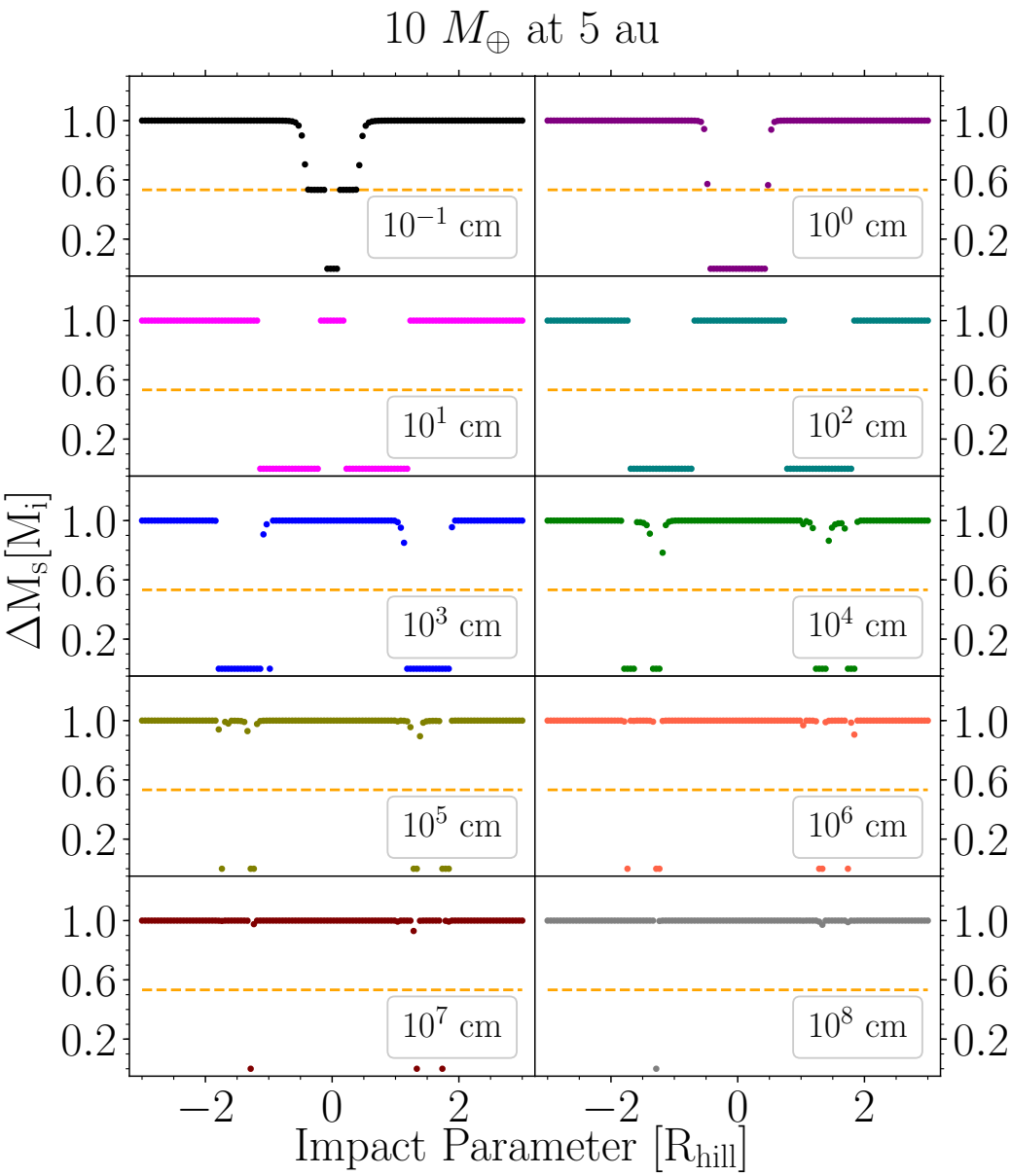

Figure 3.5: The ratio of the final to the initial mass, after an encounter, as a function of particle size and impact parameter. The orange dashed line corresponds to the initial water-mass fraction of the solids. Notably, when particle destruction is included, the particles can ablate a fraction of their mass as they pass the protoplanet without being fully accreted. Thus the accretion window is enlarged when ablation is included in comparison to the CCA where only the fully accreted particles define the size of the accretion window. This effect can be seen on the edges of the accretion windows for the 10^{-1} cm particles. For particles of $10^1 - 10^2$ cm, the accretion window is essentially the same as in the CCA, and for planetesimals ($10^3 - 10^8$ cm), the partially ablated solids only deposit mass on the order of a few percent, and the accretion windows are chaotic.

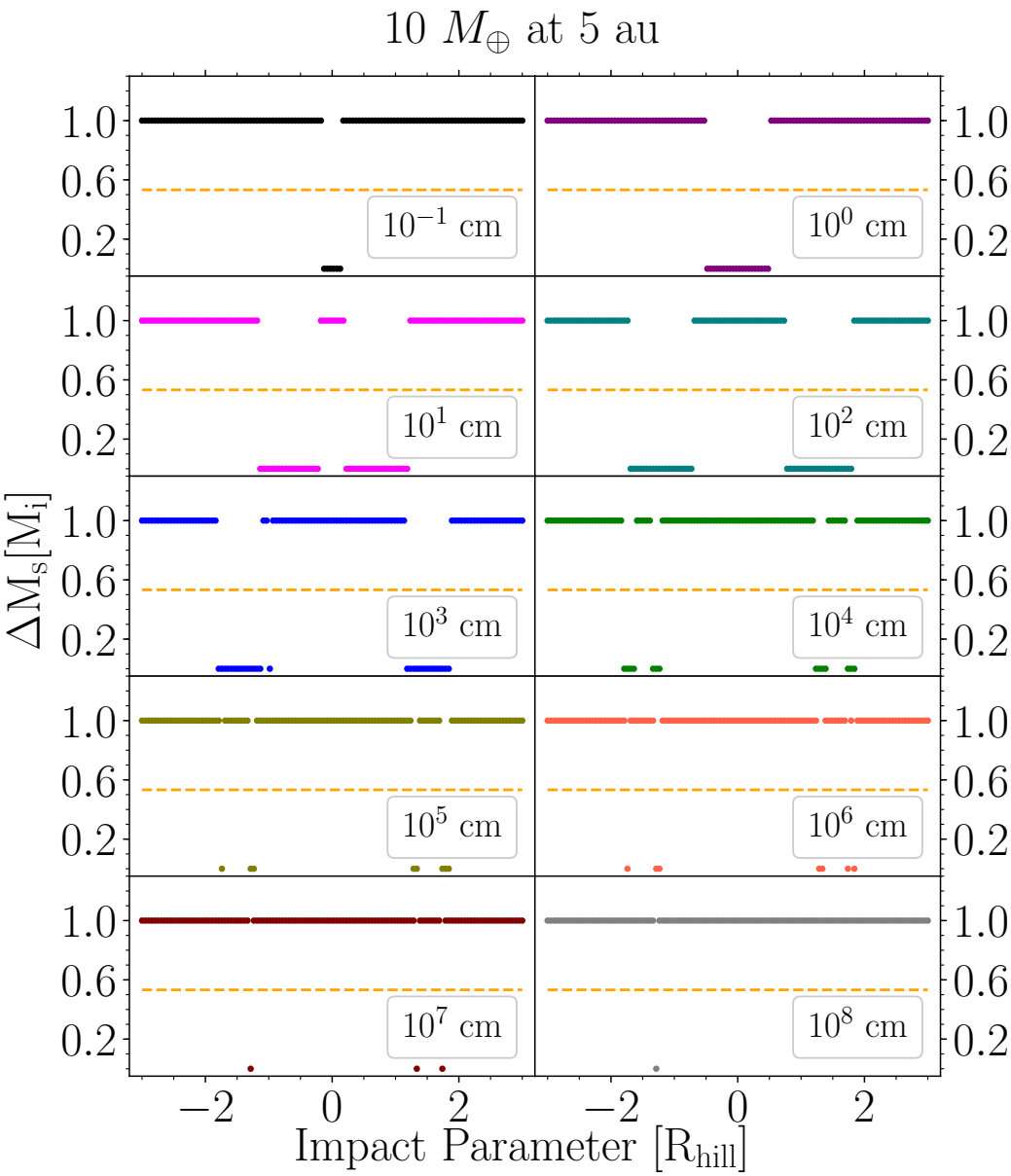

Figure 3.6: Same plot as in Figure 3.5, but in the case of the CCA model. Because ablation is not included, the particles are either located at a value of 1 or 0. Thus, no structure on the edges of the accretion windows is obtained, which is most prominent in the case of the 10^{-1} cm particles when compared to Figure 3.5. See text for details.

results shown in Figure 3.5 further suggest that significant partial ablation is an unlikely scenario for planetesimals, as the ablated mass of these objects are mostly found on the order of a few percent. The majority of the accreted mass thus come from planetesimals that are fully accreted, either by ablation close to the core or a by direct impact. The similarity between the PMA and the CCA model, for the fully accreted planetesimals, ($\geq 10^3$ cm, Figure 3.5 & 3.6) indicate that ablation has little to no impact on which particles are fully accreted, thus the total accretion is expected to essentially be the same.

3.3 Surface temperatures and ablation time-scales

In Section 3.2, it turned out that scattered planetesimals ablate inefficiently, with only a few percent of mass being lost if they are not fully accreted. Since the ablation rate is directly connected to the surface temperature of the impactors, it is of interest to relate the surface temperature to the respective particle trajectories. In Figure 3.7, the temperatures of the particles have been plotted against the radial distance from the protoplanetary core. This has been done for a subset of data points extracted from my simulations[2], where particles that follow the same structure have been combined. In addition, the temperature of the envelope is plotted as a yellow line for comparison, as well as the water ice line (orange dashed) and the silicate line (red dashed).

For small particles ($\leq 10^1$ cm, top left), the surface temperatures trace the temperature of the envelope. Since the frictional heating of these particles is low, due to the strong coupling to the gas (Section 2.3.2), it becomes apparent from Equation 2.46 that $T_{\mathbb{S}} = T_{\mathrm{g}}$ only holds if there is little to no latent cooling. This means that the particles rapidly remove the available material that is undergoing sublimation, thus quickly reaching a point with no latent cooling where $T_{\mathbb{S}} = T_{\mathrm{g}}$. Finally, all the particles are fully ablated at above $10\,R_{\mathrm{c}}$.

As the size of the particles is further increased (10^2 cm, top right), the surface temperatures start to deviate from the envelope profile as they pass the water ice line. The reservoir of water is now larger, thus the time to sublimate increases and more energy is used to change the ice into vapour rather than heating the surface. Once the water is gone, the solids are moving towards the envelope temperatures. Notably, the points along the envelope profile are more scattered in comparison to the smaller particles, which is due to the frictional heating that becomes more important as the particles decouple from the gas, and possibly the start of silicate sublimation.

For particles of size $10^3 - 10^5$ cm (mid), the latent cooling is apparent as a separate branch with temperatures below that of the envelope. The massive reservoirs of water allows for longer cooling which keeps the surface temperatures low deeper inside the envelope. Noticeably, the difference between the envelope and the surface temperatures reach up to several hundred Kelvin. When the solids have lost their water content and stop to sublimate, they reach the envelope temperature similarly to the pebbles. The significant

[2]The full dataset consist of approximately 10^6 points for each particle size, hence a data reduction has been made to highlight the general features. The omitted data points are mainly those that overlap.

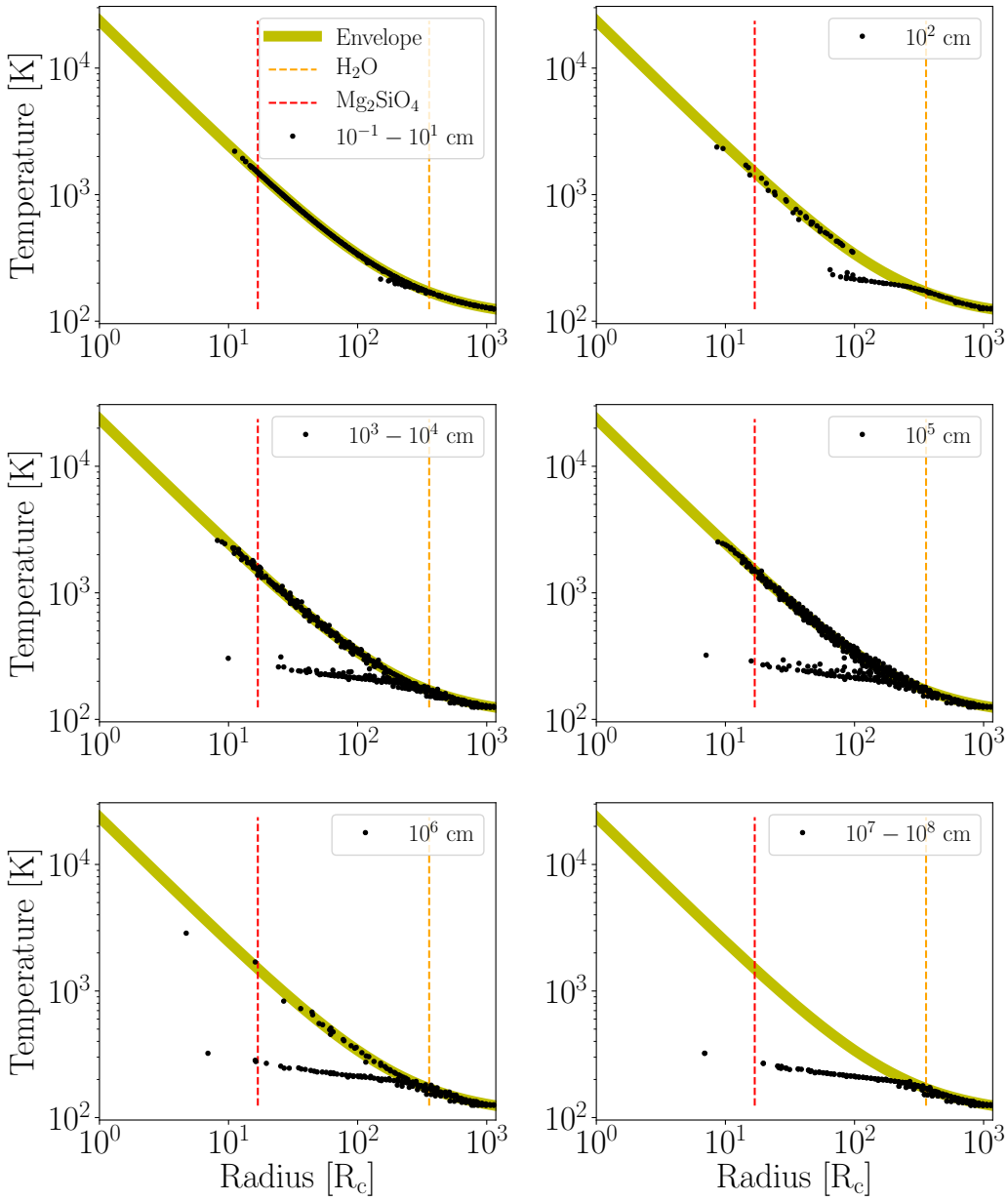

Figure 3.7: The surface temperature of the impactors as a function of their distance from the protoplanetary core. The particles which follow the same trend has in this case been plotted together. Furthermore, the water ice and the silicate lines are shown as orange and red dashed lines, respectively, to guide the eye. The temperature of the envelope is plotted as a yellow line for comparison. For the smaller particles (top), their water content is quickly removed as they pass the water ice line, causing them to heat up rapidly to the envelope temperatures. For the small planetesimals (mid) they have enough water ice to remain cold deeper into the envelope. However, once they have lost their water, they quickly retain the ambient temperature. For larger planetesimals (bot), the amount of water available is enough to keep the surface temperatures low in comparison to the temperature of the envelope throughout the scattering events.

scatter around both branches for the $10^3 - 10^5$ cm particles is finally due to increased relative velocities between the impactors and the gas, as the Stokes number is large.

For the $10^6 - 10^8$ cm particles (bottom), the difference between the surface temperature and the gas can now reach close to an order of magnitude, hence indicating that the low mass deposition fractions of the planetesimals, shown in Section 3.2, is due to efficient latent cooling. Furthermore, as was discussed in Section 3.1.3, it is more difficult to capture the larger planetesimals because the efficiency of the gas-drag drops with increasing particle size. Consequently, less amount of $10^6 - 10^8$ cm size particles are captured by the protoplanet, thus the number of data points and the scattering drops in comparison to the $10^3 - 10^5$ cm population (mid).

3.3.1 Surface temperature and ablation rate

In this section, I analyse the relation between the surface temperature and the ablation rate of the particles, and further compare the result to the envelope temperature. This is done by solving Equation 2.46 for $T_{\mathbb{S}}(T_{\mathrm{g}})$ numerically, using the mean relative velocity between the gas and the particles obtained in the simulations (constant frictional heating). An ablation rate can then be related to the envelope temperature through the surface-envelope-temperature relation and Equation 2.44[3].

In Figure 3.8, the surface temperature (left), and the ablation time-scale ($M/\dot{M}$, right), have been plotted against the temperature in the envelope. This has been done for solids made entirely out of water (orange), and forsterite (black), respectively, using the parameters from Table 2.3. Furthermore, the temperature of the envelope has been plotted as a yellow line for comparison. For readability in the right panel, only a subset of particle sizes have been plotted, where the size is shown in the respective text boxes[4].

In the left panel, the water rich particles indicate that as long as there is water present at a given envelope temperature, thus also location in the envelope, the particle can remain cool. This reflects the importance of the amount of available water ice in the solids that encounter the protoplanet. When no material is sublimating, the surface of the solids obtain the temperature of the envelope, clearly shown in the case of the silicate rich impactors, which do not sublimate to a significant degree below 2000 K.

In the right panel, the ablation times stretch between tenths of years ($\sim 10^8$ s) to seconds depending on the envelope temperature and the particle size. In order for a particle to fully ablate, the scattering time within a temperature limit inside the envelope has to be comparable to the ablation time-scale. Near the water ice line, the sub-centimetre particles require a scattering time which is longer than about 1-100 days. Meanwhile, the particles that are larger than 10^1 cm would need a few years. However, the ablation time-scales decrease as the particles approach the protoplanetary core. As an example, it takes a few

[3]In case the surface temperature reaches the critical temperature of either water or silicate (Table 2.3), the mass loss is given by Equation 2.45. However, these temperatures are not reached due to latent cooling.

[4]The particles, that are not shown in Figure 3.8, follow the same pattern as the particles shown; but are shifted to the middle between the plotted lines.

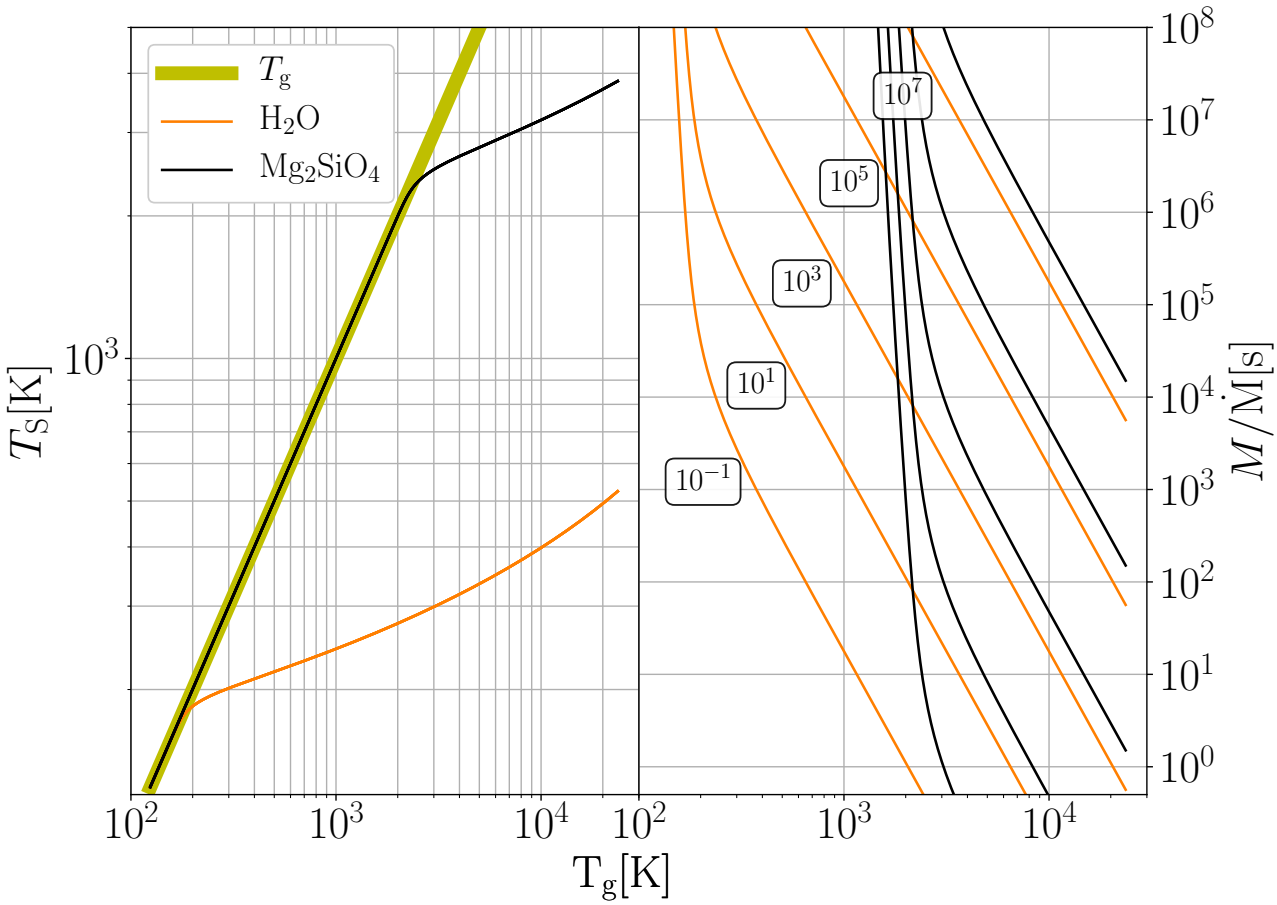

Figure 3.8: The surface temperature (left) and the ablation time-scale (right) for water- (orange), and silicate-rich impactors (black), as a function of envelope temperature. Furthermore, the envelope temperature has been plotted as a yellow line for comparison. In the right panel, a subset of particle sizes have been chosen for readability, with the size being denoted in the text boxes connected to the respective lines, given in centimetre.

days to sublimate a 10^3 cm size, water-rich, planetesimal at $T_g = 10^3$ K. In the left panel of Figure 3.8, it is shown that 10^3 K in the envelope corresponds to an effective surface temperature of about 250 K, meaning that the sublimation is limited by the latent cooling. As another example, for the planetesimals of 10^7 cm in size, as much as 3000 K is needed for them to fully sublimate their water within a year. It is thus likely that planetesimals have to be captured on in-spiralling orbits, as discussed in Section 3.1.3, in order to fully ablate before hitting the core. In the case of silicate-rich particles, the importance of in-spiralling orbits increases, if they are to fully ablate, due to the higher condensation temperatures. Nonetheless, in Figure 3.7, most data points are not located close to the core. There are three possible explanations in the case of the planetesimals: The probability of scattering close to the protoplanet is small, the in-spiralling planetesimals spent enough time in their orbits to fully ablate before they reached the core, and/or the planetesimals reach a fragmentation limit.

As a final remark, the similarity between the theoretical surface temperatures, shown in Figure 3.8, and the data points found in my simulations (Figure 3.7), tells us that a constant frictional heating is a fair approximation.

3.4 Dynamics and fragmentation

In order to determine the importance of fragmentation, a collective wake model was implemented (Section 2.4.2). The initial internal strength were then derived from Benz & Asphaug (1999), with a minimum dynamical pressure limit of 10^7 dyne cm^{-2}. In this section, I present the velocities and dynamical pressures obtained in the nominal model.

In Figure 3.9, the velocity (left) and the dynamical pressure (right) are plotted against the radial distance from the core. The water ice and the silicate line are further shown as an orange and a red dashed line, respectively, to guide the eye. In the left panel, the Hill speed is shown with a dotted line, as it is the typical speed at which planetesimals are scattered by protoplanets and a commonly used velocity in central impact simulations, e.g. Mordasini et al. (2006), hence also a useful quantity for comparison. The colors on the data points are relating the particle sizes that behave similarly. For each size, an average velocity and dynamical pressure has been calculated as a function of radial distance, plotted as black lines in order to highlight the general trend within each population[5].

The 10^{-1} cm particles (blue) correspond the most slowly moving population, and are the only ones that slow down significantly as they pass the silicate line. The low speed can be understood from their strong coupling to the gas, which also is the reason why most of them pass the protoplanet without being pulled towards the core (Section 3.1.1). Only the particles passing close to the protoplanetary surface will get redirected towards the core. Nonetheless, it should be noted that these particles are the most uncertain regarding dynamics due to their tight coupling to the approximated gas-flow used in this work (Section 2.3.2).

[5]The bins used for the averaging are logarithmically distributed in 50 steps between $10^{-3} - 1\,R_{\rm Hill}$.

The 10^0 particles (orange) have a nearly constant velocity once they have passed the water ice line. They slow down when the gravity and the drag-force become comparable and are eventually accelerated towards the core.

The 10^1 cm particles (green) approach the water ice line close to the Hill speed. As they ablate, the gas-drag is still acting which results in a complicated structure when they approach the core. Noticeably, once the particles of both 10^{-1}, 10^0, and 10^1 cm ablate their silicate, they essentially settle down towards the core.

On higher velocities are the $10^2 - 10^6$ cm boulders and planetesimals (purple) followed by a high-velocity population of $10^7 - 10^8$ cm planetesimals (red). These populations only show an increase in the mean velocity towards the protoplanetary core, where the smaller population has significant scattering, while the larger planetesimals are more consistent due to being more difficult to capture by the protoplanet, as was also pointed out in Section 3.3.1. The lack of a complicated structure, in comparison to the pebbles, indicate that the complexity shown for the $10^{-1} - 10^1$ cm population is due to drag.

In the right panel, the same group distribution is observed since the dynamical pressure is proportional to the velocity squared. For comparison, the dynamical pressure has further been calculated using multiples of the Hill speed, shown as dash-dotted lines. The multiples shown here are for 1, 10, and 100 times the Hill speed.

To conclude the dynamical pressure trends for the sub-metre pebbles, none of them are reaching anywhere near the fragmentation limit of $10^7\,\mathrm{dyne\,cm^{-2}}$ as one would intuitively expected for small particles. However, it is surprising that the planetesimals of $10^2 - 10^8$ cm also did not reach the fragmentation limits used the simulations. Consequently, neither the constant fragmentation limit, nor the estimated internal strengths of Benz & Asphaug (1999) resulted in the Collective Wake approach being used to a larger extent (Section 2.4.2). My results are thus in agreement with Inaba & Ikoma (2003) but not with the results of Mordasini et al. (2006), where the first did not find fragmentation important in contrast to the latter mentioned. There are two possible reasons for why fragmentation is not observed: Firstly, due to the initial velocities being too small. Secondly, the densities in the envelope being underestimated.

If the upwards bending trend of the planetesimals in Figure 3.9 (right) is extrapolated towards the core, the critical fragmentation limit of $10^7\,\mathrm{dyne\,cm^{-2}}$ would be reached below $1-3\,R_\mathrm{c}$. The theoretical dynamical pressure lines (dash-dotted) indicate that several tenths of the Hill speed is needed if the planetesimals are to reach a dynamical pressure limit. On the other hand, if the density of the envelope can be increased, the required velocities would be lower. For example, Lambrechts et al. (2014) found that if the envelope is polluted by water, the densities may increase by an order of magnitude. Since the dynamical pressure scales linearly with the density of the gas, the planetesimals in my simulations would reach a maximum of about $10^6\,\mathrm{dyne\,cm^{-2}}$, which is still not enough to reach the fragmentation limits used in this work. As a final remark, the Hill speed decreases further out in the protoplanetary disc, and the radius of the protoplanetary core further depends on its assumed density, making it difficult to pinpoint the location where the particles would fragment.

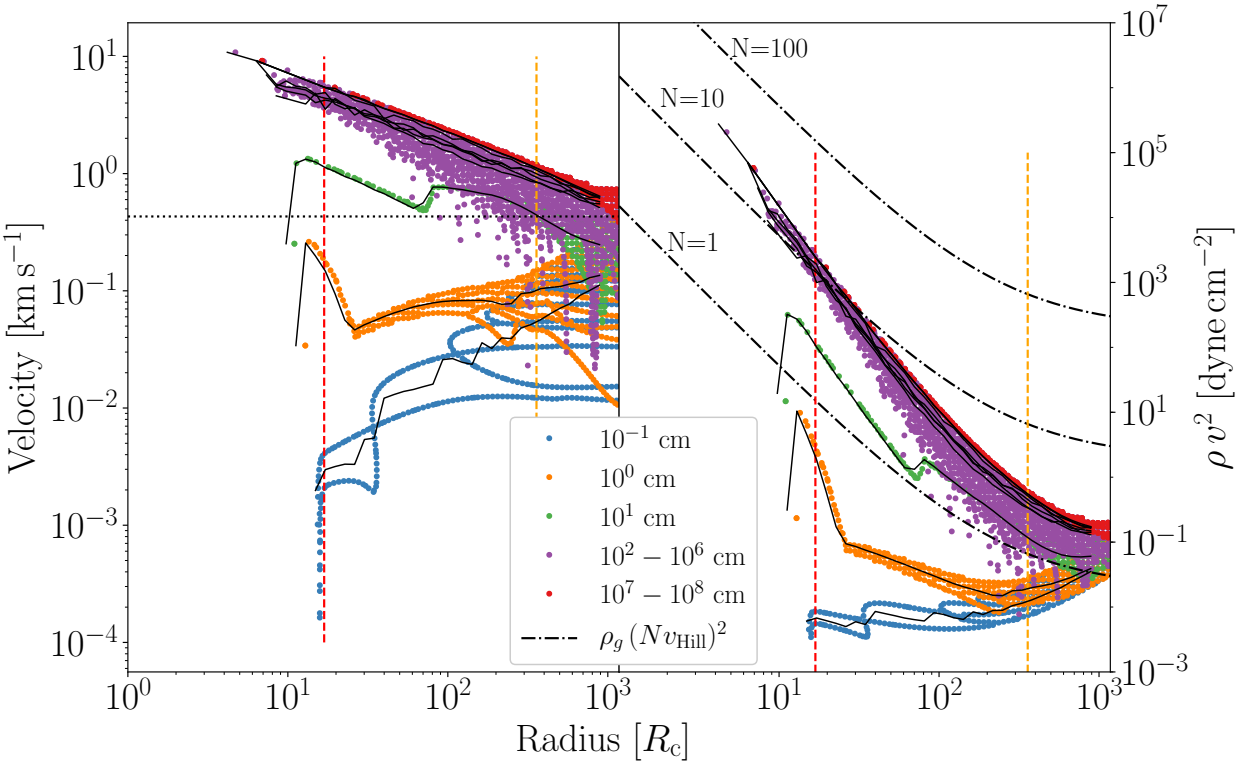

Figure 3.9: The velocity distribution for particles ranging from 10^{-1} to 10^{8} cm as a function of distance from the core (left). The condensation lines of water and silicate have been plotted as an orange and red dashed line, respectively. We see five different trends between the size populations: 10^{-1} cm (blue), 10^{0} cm (orange), 10^{1} cm (green), $10^{2}-10^{6}$ cm (purple), and $10^{7} - 10^{8}$ cm (red). The average velocity for a logarithmic distribution of bins on the x-axis has been over-plotted for each particle size to highlight the most common velocities for a given radial distance. Furthermore, the Hill speed is shown as a dotted line for comparison. The right panel shows the same distribution as in the left panel, however, this time for the dynamical pressure that the particles are subjected to. Notably, they do not reach the lower fragmentation limit of 10^{7} dyne cm^{-2} that was used in this work. In addition, the theoretical dynamical pressures obtained for multiples of the Hill speed are plotted as dashed-dotted lines, where the multiplicities shown are 1, 10 and 100.

3.5 Ablation versus radial distance

It is of interest to relate the ablated mass as a function of distance from the core and time. It tells us whether ice lines are good estimates for the regions where the particles sublimate when combined with dynamics. Furthermore, it gives an idea whether the scattering times are comparable to the ablation time-scales, a requirement to fully ablate which was discussed in Section 3.3.1.

In this section a subset of particles have been chosen to highlight specific features that are observed in the simulations, shown in Figures 3.10, 3.11, and 3.12. The top panel shows the radial distance from the core, and the bottom panel corresponds to the mass of the particles, both as a function of simulated time. The figures further contain the Hill radius (black dashed), and the Bondi radius[6] (gray dashed), which has shown to play an important role for low-mass accretors, e.g. Lambrechts & Johansen (2012).

3.5.1 Stokes number < 1

The particles with low Stokes number are in general expected to follow the gas-flow, thus not experience any significant frictional heating (Section 2.4.1 & 2.3.2). The ablation is consequently set by the latent cooling and the net radiation absorbed. With the low frictional heating in mind, Figures 3.10 shows the trajectories for three particles with sizes of 10^{-1} (black), 10^{0} (blue), and 10^{1} cm (red). For details regarding the figure, the reader is directed to the second paragraph in Section 3.5.

For the 10^{-1} cm dust grain (black), the particle approaches the core with a low velocity (see Section 3.4) and begins to slowly sublimate before reaching the water ice line. As the particle reaches the ice line it has essentially dried out. This means that the water ice line acts as a lower radial boundary which stops water from the smallest particles to enter deep into the envelope, unless the gas-flow with the vaporised material is pulled towards the core. The dry particle then becomes strongly coupled to the gas and leaves the envelope, similar to the case found in Popovas et al. (2018).

For the 10^{0} cm size particle (blue), a trajectory which barely reaches the water ice line has been chosen. Though, it deposited essentially all of its water-content before leaving the system. The particle spends well above a thousand days inside the envelope, however, the time spent close to the ice line is on the order of 100 days. Nonetheless, this time is comparable to the ablation time-scales discussed in Section 3.3.1. Arguably, small dust particles can not provide water to the core, because they have enough time to fully sublimate in the outskirts of the envelope. This raises the question whether the outer parts of the envelope become saturated with water – enough to stop the mass loss from the dust grains (see Equation 2.42), or if all the vaporised water is transported away from the core with the gas-flow (Section 2.3.2.1).

[6]The Bondi radius defines the radial distance from the protoplanet, where the orbital speed equals the sound speed of the gas, e.g. $R_{\rm Bondi} = GM_{\rm p}/c_s^2$. It marks the boundary where the structure of the envelope differs significantly compared to the local disc-parameters.

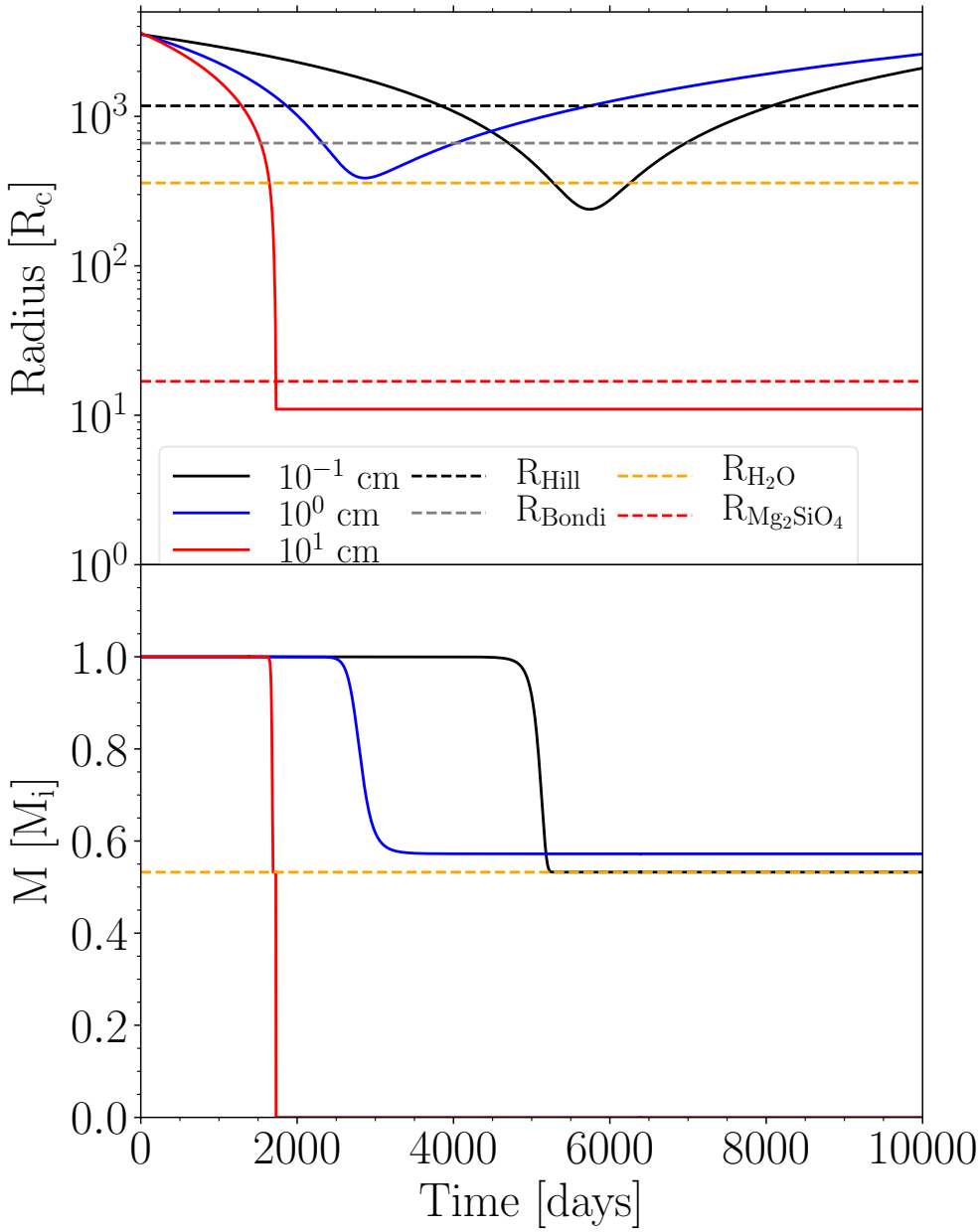

Figure 3.10: The evolution paths of three particles with Stokes number of $\sim 10^{-3}$, 10^{-2}, and 10^{-1}, encountering a $10\,M_{\oplus}$ core at 5 au. The top panel shows the distance from the core, and the bottom panel is the particle mass in terms of its initial mass, plotted against the simulated time.

The red line in Figure 3.10 correspond to 10^1 cm particles, which also represents the metre-sized solids due to their similar trajectories once they have entered the envelope (Figure 3.1 & 3.2). As they efficiently lose momentum to the gas they are essentially guaranteed to get accreted once they have entered the Hill sphere. During the in-fall, the 10^1 cm particles lose their water content within about ~ 10 days, consistent with the fact that the ablation time-scales correlate with the radial distance in the envelope (Figure 3.8). Notably, once the remaining silicate pebble reaches the silicate condensation line, it is rapidly vaporised at a radial distance from the core of about $10\,R_{\rm c}$ as can be seen in the top panel.

In conclusion, small particles may begin to sublimate outside of the ice lines, indicating the importance of the steep end of the ablation time-scales, discussed in Section 3.3.1. The slow trajectories in the outskirts of the envelope result in long orbital time-scales, such that low saturated vapour-pressure support is enough to fully ablate the particles. At the ice lines, the water of the small particles is essentially gone.

3.5.2 Stokes number > 1

The larger particles ($r_{\rm s} > 10^2$ cm) show more scattering outcomes and in-spiralling scenarios compared to the dust grains (Section 3.1). It was further indicated in Section 3.2, that planetesimals either ablate fully close to the core, or only ablate a few percent of their mass when scattered. This section is dedicated to a subset of trajectories from the size population in the range $10^3 - 10^8$ cm.

Figure 3.11 shows the distance from the core (top) and the particle mass in terms of the initial mass (bottom) as a function of the simulated time – see second paragraph in Section 3.5 for the structure of the figure.

For the 10^4 cm particle (blue), the planetesimal first encounter the protoplanet by passing the water ice line by a small margin. The time spent inside the envelope during the single scattering event is significantly smaller than for the slow dust grains shown in Figure 3.10. Nonetheless, the planetesimal is located below the ice line for about 100 days during the first scattering, but less than a percent of its mass is ablated. In the second scattering of the 10^4 cm size particle, it comes near the ice line, but no ablation occurs. It turns out, that the planetesimals have to pass the water ice line by a large fraction in order to sublimate, which is shown by the 10^3 (black) and 10^5 cm (red) particles. In this case, each scattering event below the water ice line remains on the order of 100 days. For the 10^5 cm size planetesimal, the in-spiralling accretion scenario is further observed, where the planetesimal losses a few percent of its water for every close encounter. Intuitively, it is expected that the closer encounters lead to more sublimation. However, this is not clear from Figure 3.11. The 10^5 cm particle spends several hundred days deep inside the envelope before it finally dries out. The only mechanism to limit the sublimation is thus the latent heat, which in Section 3.3 was shown to be efficient.

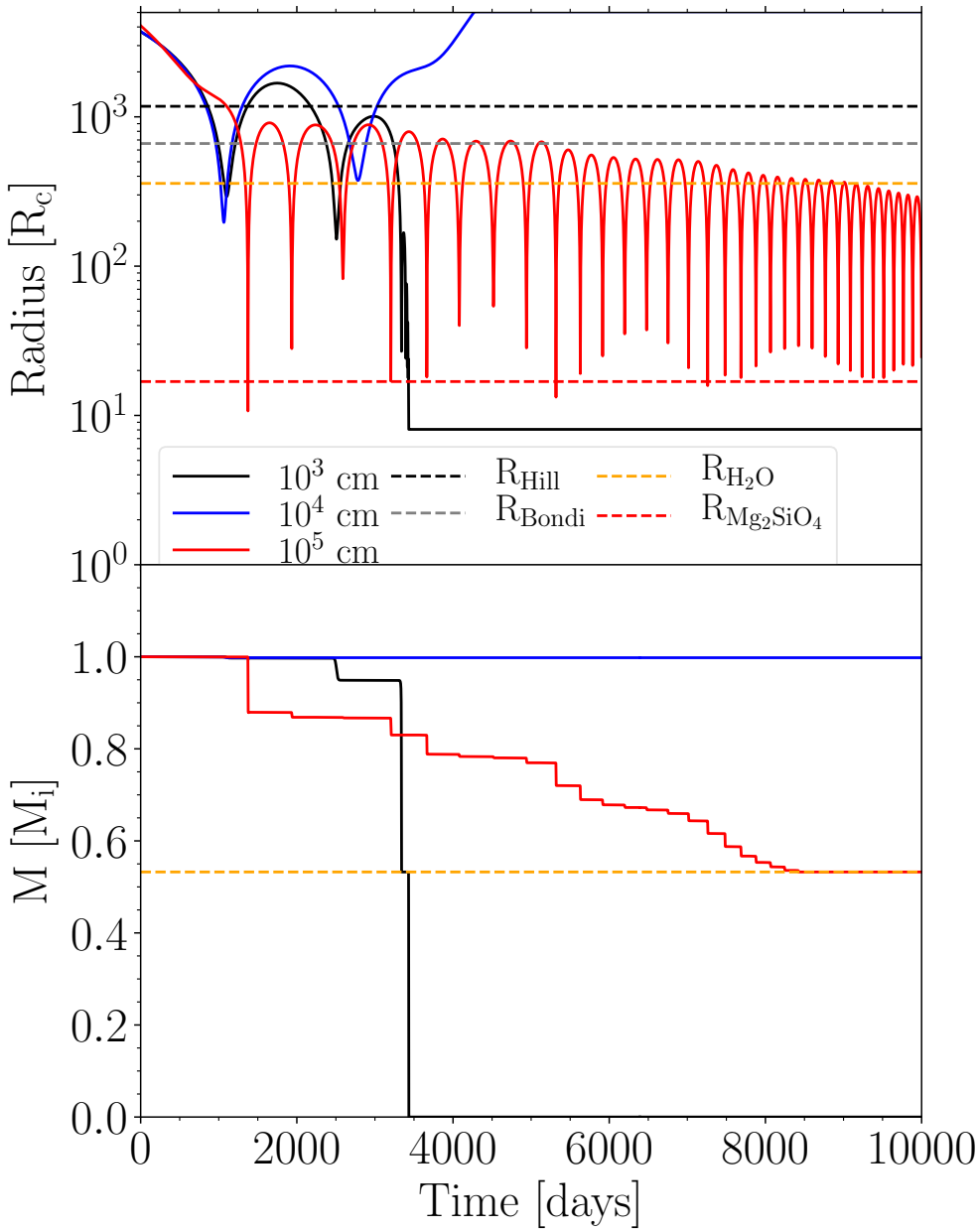

Figure 3.11: Same plot as in Figure 3.10, but for small to intermediate size planetesimals with Stokes number of $\tau \sim 10^2$, 10^4, and 10^6.

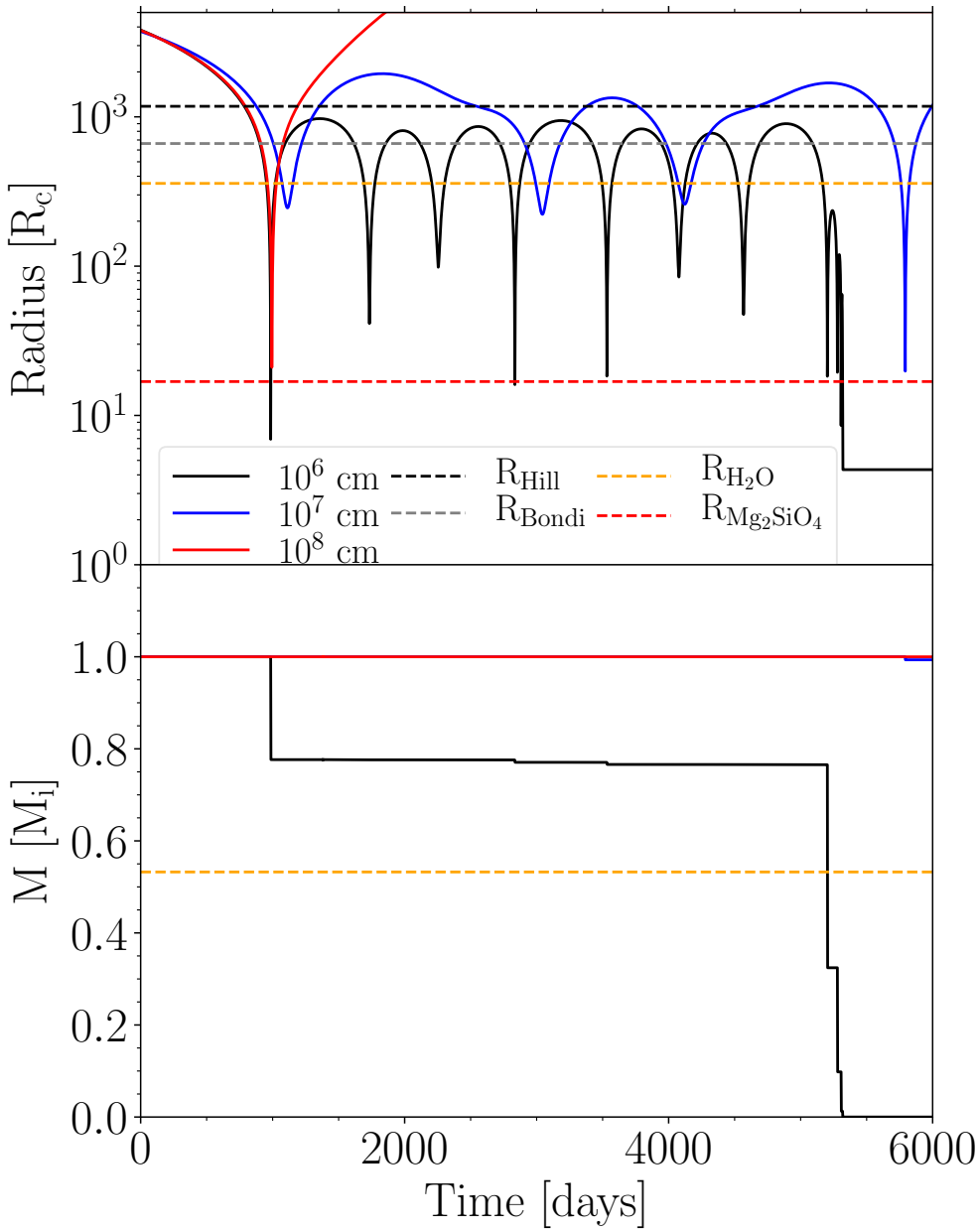

Figure 3.12: Same plot as in Figure 3.10, but for large planetesimals with Stokes number of $\tau \sim 10^8$, 10^{10}, and 10^{12}.

In Figure 3.12, the trajectories of 10^6 (black), 10^7 (blue), and 10^8 cm (red) size particles are shown. This is to illustrate that multiple scatterings are not necessarily providing water to the protoplanet through ablation, unless they get close to the core. As an example, the 10^6 cm size planetesimal is not depositing a significant fraction of water, unless it nearly reaches the silicate condensation line. The silicate line for a $10\,M_\oplus$ core at 5 au corresponds to a distance of $\sim 0.01\,R_{\rm Hill}$ (Figure 2.2), thus the cross-section is even smaller than that of gravitational focusing (Section 2.5.3). The 10^8 cm planetesimal is here shown to be resistant against ablation even if it penetrates deep into the envelope. Finally, the 10^7 cm particle remains in the outer parts of the envelope throughout its scattering events, thus having negligible mass loss.

3.5.3 Destruction radii

A commonly used plot when studying destruction events in protoplanetary envelopes is the penetration depth of the impactors. It estimates when the protoplanetary cores stop to grow – when all impactors vaporise in the envelope, e.g. Brouwers et al. (2018). While those plots are mostly based on central impacts, thus resulting in well defined destruction radii, the results obtained in this work rely on the dynamics of the particles, making the plot rather difficult to interpret once scattering events become important. Nonetheless, the location of the complete vaporisation events of water has been plotted against the initial particle size in Figure 3.13, for a 1, 5, 10, and $50\,M_\oplus$ core at 5 au. The planetesimals are widely scattered as expected. However, the small particles that are affected by drag can roughly be treated as central impactors, hence the distance at which they lost their water is well defined.

In the case of a core mass of $1\,M_\oplus$ (top left, Figure 3.13), and for lower masses, the final location of destruction radii is chaotic, because the thin envelopes allow even small particles to scatter. Consequently, for such small cores, the destructive radius only tells us that the 10^{-1} cm size particles are completely dried out just after passing the water ice line, while the larger particles can not be quantified.

For $50\,M_\oplus$ cores (bottom right) larger particles are affected by the gas-drag, as the density in the envelope is higher, and the friction-time scales as $t_{\rm f} \propto c_{\rm s}^{-1}\,\rho_{\rm g}^{-1}$. Thus, the destruction radius for the particles around a $50\,M_\oplus$ core become well defined up to metre-sized objects.

However, because the $1\,M_\oplus$ core is dominated by scattering, and $50\,M_\oplus$ cores are rarely considered in the literature, they are difficult to compare to previous work. Though, the destruction radii for $10^{-1} - 10^1$ cm particles, around a 5 and $10\,M_\oplus$ core, are well defined (top right & bottom left), and can be compared to e.g. Pollack et al. (1986), who showed that the destruction radius is located about $10^2\,R_{\rm c}$. Their result is thus in rough consistency with my results. Finally, the most massive planetesimals are rarely depositing all of their water inside the envelopes, with only one 10^8 cm planetesimal being fully dried out above the $50\,M_\oplus$ core in the lower right panel.

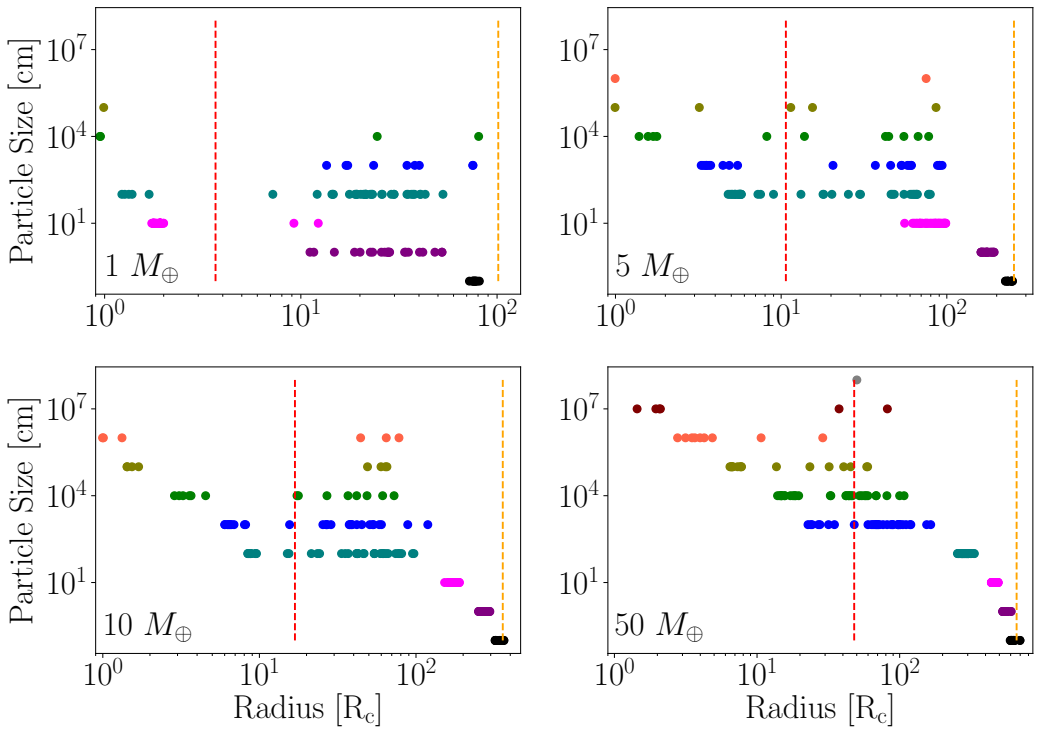

Figure 3.13: The particle sizes plotted against the radius at which the particles sublimated their final water content in the simulations. This is shown for core masses of 1 and 5 $M_\oplus$ (top), as well as for 10 and 50 $M_\oplus$ (bottom), located at 5 au. For 1 $M_\oplus$, no trend is observed besides millimetre pebbles being vaporised close to the water ice line. For larger protoplanetary cores, the majority of the small particles deposit all their water close to the water ice line. The larger object are, on the other hand, not well quantified by this approach, as their trajectories are dominated by scattering, thus the final location at which they deposited their final water content is widely scattered.

3.5.4 Minimum particle size to reach the core

Depending on what size of particles are being accreted by protoplanets, they will either ablate in the envelope, or reach the core. The study of the minimum particle size that is able to penetrate the protoplanetary envelopes has been made in previous work, e.g. Mordasini et al. (2006). The goal is to estimate the minimum particle size as a function the mass of the envelope. When no particles can make it to the core, the impactors contribute to the pollution of the envelope instead of the core-growth. Consequently, the minimum particle impactor gives a hint on whether the internal structure of giants, that we see today, e.g. Fortney & Nettelmann (2010), evolved from small cores with massive polluted envelopes, or from massive cores.

In this section I present the particles that were able to penetrate down to the protoplanetary core for the particle radii

$$[10^0, 10^1, 10^2, ..., 10^8]\,\mathrm{cm},$$

for protoplanets with core masses of 0.5, 1.0, 5.0, 10, and 50 $M_\oplus$, corresponding to envelope-masses of

$$[0.2, 0.4, 2.3, 5.7, 98.0] \times 10^{-2}\,M_\oplus,$$

obtained by integrating the respective density density-profiles (Section 2.2). The result is shown in Figure 3.14, where the particle size is plotted against the mass of the envelope. Here, the particles that are capable of reaching the core are marked as filled circles, whereas the particles that were fully ablated in the envelope are market with a cross. Furthermore, the results of Mordasini et al. (2006), presented in Section 1.4, have been plotted in the background for comparison. Because the particles considered here are not central impacts, the smallest particle that is capable of reaching the core, for a given protoplanetary mass, is expected to be larger than what was obtained by Mordasini et al. (2006)[7]. For recap, on the left of the thick drawn line, their model predict that the impactors will penetrate to the core. Meanwhile, on the right side of the line, the impactors are fully ablated.

In Section 3.5.3, it was shown that the specific trajectories of the impactors become important once the size of the impactor is larger than about 10^{-1} cm for core masses of 1 $M_\oplus$; 10^1 cm for 5 and 10 $M_\oplus$; and about 10^2 cm for 50 $M_\oplus$. These four cases correspond to the four most massive envelopes shown in Figure 3.14, and indicate that the crosses, which are located on the left of the thick line, are all in the regime where the particle trajectories matter. The dynamics thus make it unlikely that these particles survive down to the core as predicted by Mordasini et al. (2006).

Finally, as was seen in Section 3.4, the particles do not reach the fragmentation limits applied in this work. Consequently, no complex pattern, such as the 'tooth-shaped' curve in Figure 3.14 (see also Section 1.4), is reproduced.

[7] A central impact scenario results the shortest path to the core, hence it is the ideal case for the particles to reach the core.

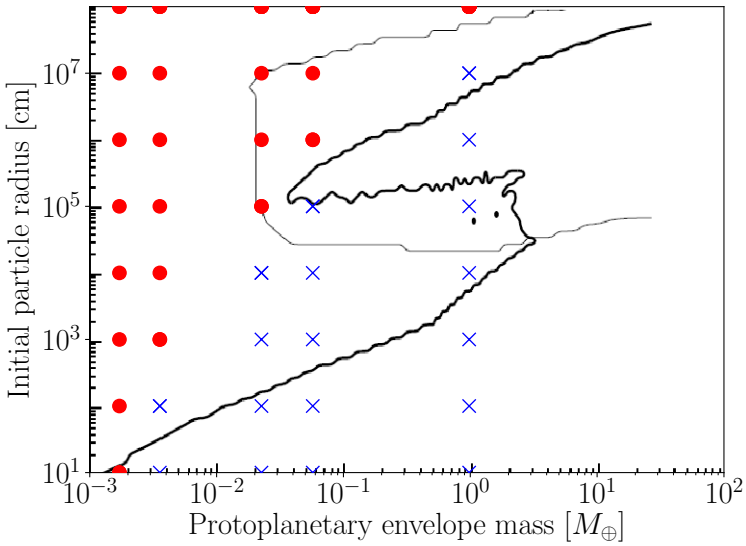

Figure 3.14: The particle size versus envelope mass. The particles that were able to reach the core (red filled circles), and those that fully ablated in the envelope (blue cross) for protoplanets located at 5 au, have been plotted onto the resulting graph of Mordasini et al. (2006). The thick line divides the region where the particles are expected to hit the core (left), and the region where they fully ablate in the envelope (right). The thin line corresponds to the region where they found that fragmentation becomes important.

3.6 Accretion rates

After analysing the destruction of single particles (small scales), it is of interest to connect the results to the larger picture in planet formation models. A reasonable step is to combine the obtained mass deposition rates of the individual particles with an accretion model. Here, the protoplanets are subjected to a continuous flow of particles, where the rate of the inflow is determined by the Keplerian, or sub-Keplerian speed, and the dust column-density (Section 2.5.3). In the previous sections of Chapter 3, the impact parameter was related to a mass loss efficiency due to ablation. Thus, the accretion rate onto the protoplanets can be divided into channels, centred on each impact parameter and then be weighted according to the fraction of mass that either hit the core, or sublimated in the envelope.

3.6.1 Vapour accretion versus full accretion

Whether material is accreted in the form of vapour or solid is of interest when studying the internal structure and composition of protoplanets. The classical view of protoplanets is a solid core with a thin envelope, depending on its formation stage. However, if most material vaporises before reaching the core as the protoplanet grows, it is possible that the whole protoplanet takes the form of a vapour-blob.

Figure 3.15 shows the accretion rate of both the vapour and solid material (red triangles) and that of the vapour only (cross marks), plotted against the particle size. This is done for the respective core masses: 0.1 & 0.5 $M_\oplus$ (top), 1 & 5 $M_\oplus$ (mid), and 10 & 50 $M_\oplus$ (bot). The protoplanets are located at 5 au, thus the impactors in this case consist of water and silicates (Section 2.1.1). Here, the dust column density is assumed to be $0.01\,\Sigma_\mathrm{g}$ for each particle size population. In addition, the efficient Hill accretion has been plotted for the minor bodies as a blue dotted line (Section 2.5.3).

For the 0.1 $M_\oplus$ core (upper left), the difference between the vaporised material and the total accretion indicates that most material is accreted in solid form. The accretion rates for the smaller particles, up to 10^2 cm, are in agreement with the Hill accretion and reach up to $\sim 5 \times 10^{-5}\,M_\oplus\,\mathrm{yr}^{-1}$. The planetesimal accretion is on the other hand remaining constant with size. Nonetheless, if the accretion would be dominated by planetesimals, the core would still have time to grow a few Earth-masses during the life-time of the disc ($\sim 10^6$ yr). However, note that the disc is in this case treated in two dimensions, meaning that the full scale-height for the dust populations is assumed to be incorporated into the accretion channels, consequently overestimating the accretion rates if the vertical oscillations are proven to be important (Johansen et al. 2015). This is the case for planetesimals, where the frequent scattering events increase the scale-height as they encounter protoplanetary embryos in the disc.

As the protoplanetary mass grows, the fraction of the accreted mass that comes in the form of vapour is increased. If protoplanets grow predominantly by pebble accretion (Lambrechts & Johansen 2012), the core is already evaporating all the impactors when

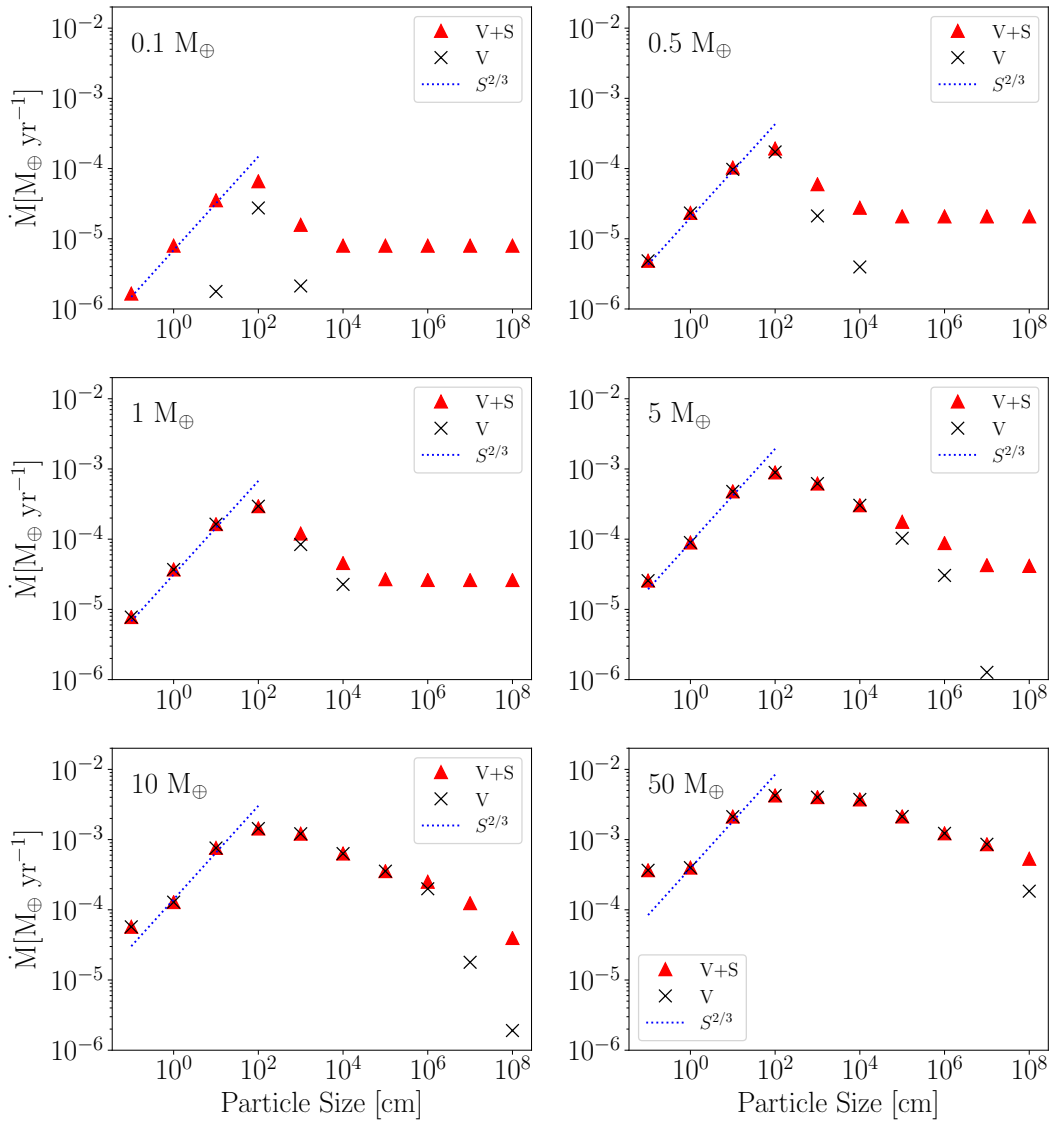

Figure 3.15: The accretion rate as a function of particle size and protoplanetary mass. The red triangles correspond to the total accretion rates (both solid and vapour). The black cross are the accretion rates of vapour into the envelope. The blue dotted line corresponds to the classical Hill accretion, as derived by Lambrechts & Johansen (2012).

reaching $0.5\,M_\oplus$ (top right). Protoplanets above $1\,M_\oplus$ can already ablate a significant part of the in-falling planetesimals. Based on the low obtained planetesimal accretion rates found in 3D hydrodynamical simulations, e.g. Bitsch et al. (2015); Alibert et al. (2018), it is reasonable to conclude that once the cores reach above $1\,M_\oplus$, the majority of the impactors are accreted in the form of vapour, resulting in vapour-blob worlds.

As an addition, the material accreted in the form of vapour versus the full accretion for a $10\,M_\oplus$ core at 1, 10, 50, and 100 au is shown in Appendix A.3. The probability of accreting large planetesimals further out in the disc is smaller due to the lowered densities. However, all the accreted material is vaporised. In the case of 1 au, a similar structure to the nominal model is shown (bottom right Figure 3.15), though it should be noted that the planetesimals at this semi-major axis consist of Silicate only in our model.

3.6.2 Full accretion rates

In this section, the full accretion (both in the form of vapour and solid material) from the PMA is compared to the CCA, where ablation is omitted. The accretion rate as a function of particle size is plotted in Figure 3.16. The CCA (black squares), is similar to the total accretion from the PMA model (red triangles). The Hill accretion is furthermore plotted (blue dotted) and traces the accretion rates for the pebbles, until the core mass reaches about $50\,M_\oplus$. At those large core masses, the density of the gas in the envelope is high enough for the smallest particles ($10^{-1} - 10^{0}$ cm) to couple to the gas strongly enough to pass the protoplanet on the approximated stream-lines used in this work (Section 2.3.2). However, in the PMA model, the dust grains encounter the condensation lines, which are moved further out in the envelope as the protoplanet grows (Section 2.2.1). The particles thus deposit a fraction of their mass, even if not passing close to the core, similar to the two smaller particles shown in Figure 3.10. For an intuitive picture, the trajectories around a $50\,M_\oplus$ core are shown for 10^{0} cm size particles in Appendix A.2, indicating that without ablation most particles pass without being accreted. This explains why the accretion rate for the smaller particles in the CCA falls below the total accretion in the PMA model for larger core masses.

Figure 3.16 shows that already at $0.1\,M_\oplus$, the cores can accrete several Earth-masses of 10^{2} cm particles within the life-time of the protoplanetary disc, which is the pebble accretion Lambrechts & Johansen (2012). The overall accretion rates for more massive protoplanets increases towards larger impactors as the protoplanet grows. This is because the more dense envelopes become more efficient at capturing the larger impactors due to the inverse scaling between the friction-time and the gas-density (Section 2.3.1.1), and because of the growing gravitational cross-section (Section 2.5.3).

I further obtain the scaling of the Hill accretion with respect to the core mass, shown in Figure 3.17 (right), where the accretion rates of the individual size populations, ranging from 10^{-1} to 10^{8} cm have been added. The apparent accretion rates thus correspond to that of a 0.1 dust to gas ratio in a MMSN model. The black squares represent the CCA, while the red triangles are the full accretion rates from the PMA model. The Hill accretion

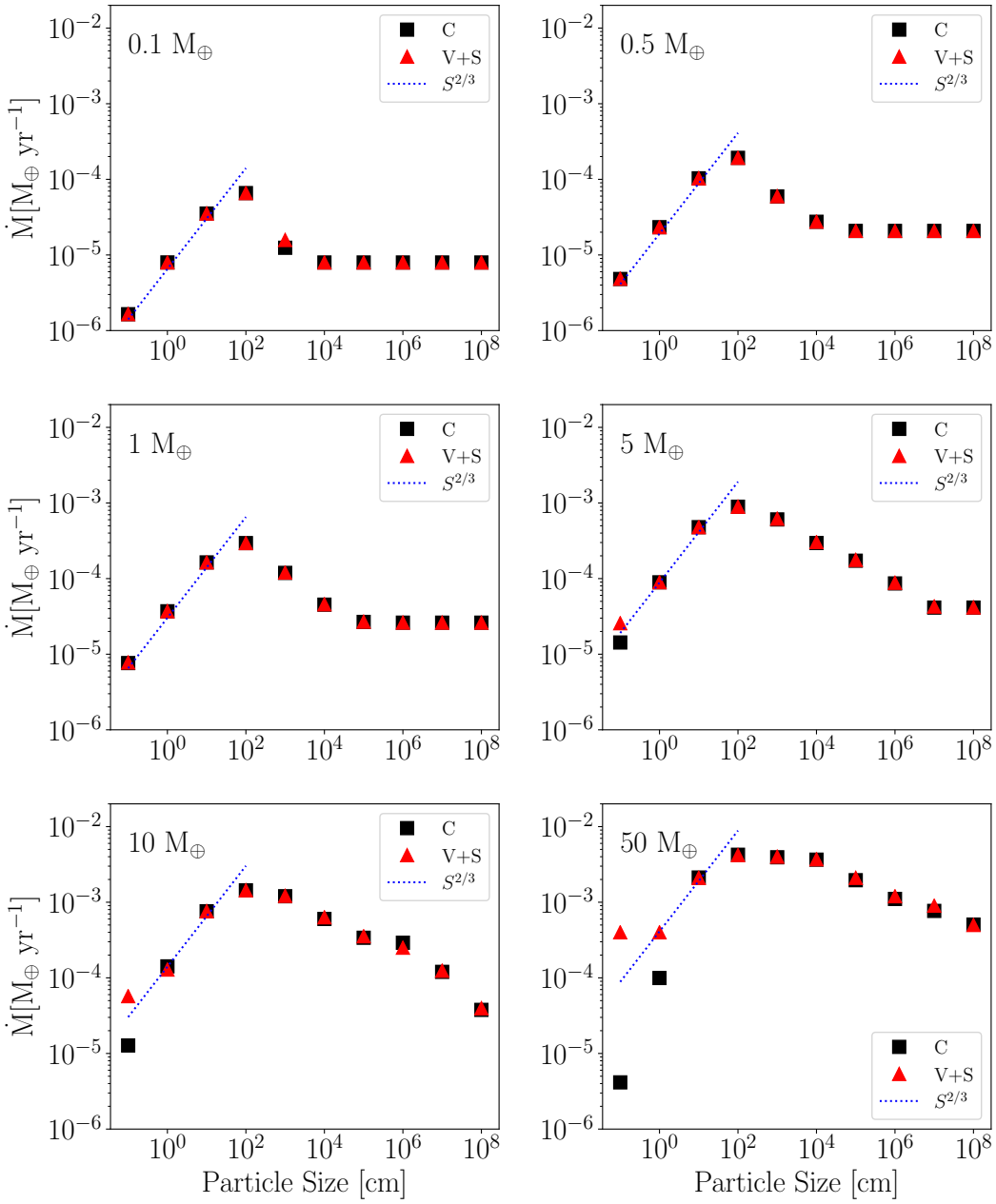

Figure 3.16: The total accretion rate as a function of protoplanetary mass. The PMA model is denoted by red triangles. The classic core accretion is plotted with black squares. The blue dotted line correspond to the Hill accretion, as derived by Lambrechts & Johansen (2012). With increasing core mass, the accretion rates increase overall. However, there is little to no deviation between the classical core accretion and the PMA model, unless core masses of $10 - 50\,M_\oplus$ are reached.

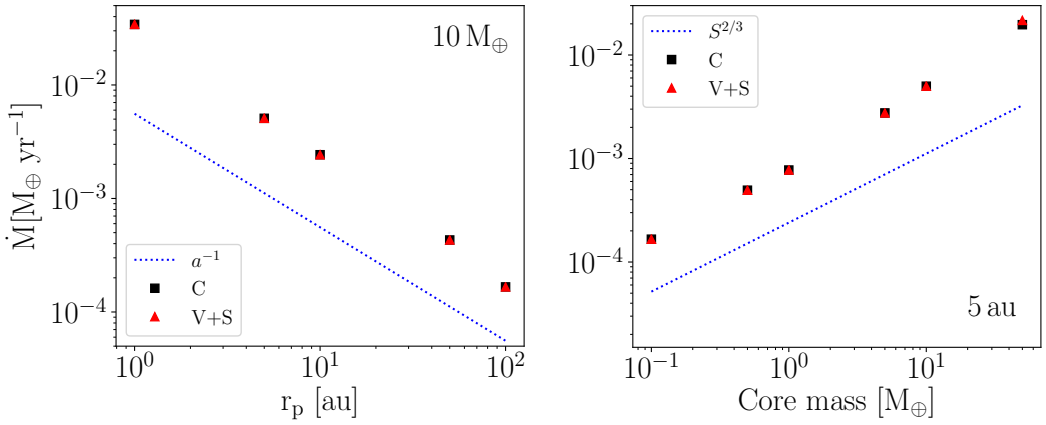

Figure 3.17: The total accretion rate in the PMA (red triangles) and the CCA model (black squares), plotted against the semi-major axis (left), and the protoplanetary mass (right). The blue dotted line corresponds to the Hill accretion. Notably, each size on the particles are here assumed to have a column density of 1% of the gas in the protoplanetary disc. Hence, the total mass of the dust in the graphs correspond to a gas to dust ratio of 1/10 which offsets the Standard hill accretion from the data points.

for a dust to gas ratio of 0.01 is plotted as a blue dotted line, confirming that the total accretion rate scales in the same way as the Hill accretion ($\dot{M}_p \propto M_p^{2/3}$, Section 2.5.3). The similar scaling means that the total accretion onto the protoplanets is dominated by Hill accretion. However, as the density in the envelope increases, the larger impactors become captured more frequently, and a slight bending towards higher accretion rates can be seen between the core masses of 10 and 50 $M_\oplus$. Because the planetesimals do not have well defined accretion windows, it is expected that the results would diverge from the Hill accretion for larger core masses. Nonetheless, the Hill accretion remains the dominant contributor.

The total accretion has also been analysed as a function of the semi-major axis for a core mass of 10 $M_\oplus$ that is located at 1, 5, 10, 50 and 100 au, shown in the left panel of Figure 3.17. Note that the chemical mixing ratios at 50 and 100 au includes CO_2 ice for the impactors (Section 2.1.1). The mass-fraction of the particles are then calculated to

$$[\, f_{CO_2},\, f_{H_2O},\, f_{\text{silicate}} \,] = [\, 0.16,\, 0.24,\, 0.60 \,].$$

Note that the accretion rates are in rough agreement with the theoretical Hill accretion, plotted as a blue dotted line and scaling as $\dot{M}_p \propto r_p^{-1}$ (Section 2.5.3). However, at 50 and 100 au, the accretion rates drop slightly in comparison to the Hill accretion. This is because further out in the disc, the particle size that corresponds to $\tau \sim 1$ is drawn towards sub-millimetre particles, which are not included in this work. Consequently, the Hill accretion is moved towards a regime that is not taken into count and the achieved accretion rates drop.

Finally, the accretion rates obtained with the CCA and the PMA overlap in both the right and left panel of Figure 3.17, implying that, as long as the volatiles are contributing to the protoplanetary growth, the total mass deposition does not differ from the CCA. In conclusion, the full accretion rates onto protoplanets follow the classical core accretion model. The accretion rates are peaking in the Hill accretion regime and scale accordingly with the core mass, the semi-major axis, and the particle size (Section 2.5.3). Thus, assuming that both the vapour and solid material contribute to the protoplanetary growth, the overall accretion rates predicted by simulations without ablation, used in previous work, e.g. Lambrechts & Johansen (2012), do not change with respect to the PMA models.

3.6.3 Introducing a planetesimal scale-height

Since planetesimals are easily scattered as they encounter planetary embryos (Section 2.5.3) and are further not effectively damped by the gas-drag, they rarely reside in the 2D plane of the disc, which has been assumed throughout this work. This section is dedicated to how an increasing scale-height would affect the planetesimal accretion rates. This is done for both the CCA, and the PMA model. Note that in the vicinity of a planetary embryo, the gas will spiral towards the protoplanet in the disc-plane (Section 2.3.2.1). However, because planetesimals are weekly bound to the gas, the vertical gas-flow is neglected, which is a good first order approximation (Nakagawa et al. 1986).

3.6.3.1 The setup for vertical oscillations

To quantify the relation between the scale-height and the accretion rates, the vertical motion of the planetesimals can be approximated with harmonic oscillations of fixed amplitudes (Johansen et al. 2015). The velocity for a given scale-height is then approximated as

$$v_z = \Omega R_\mathrm{b} \cos(\Omega t), \tag{3.1}$$

where the amplitude corresponds to a fraction of the Keplerian speed at the given scale-height R_b (Section 2.3.2). The vertical velocity is then related to a position above the disc-plane and an acceleration given by

$$z = R_\mathrm{b} \sin(\Omega t) \quad \& \quad a_z = -\Omega^2 z, \tag{3.2}$$

,respectively. Note that the equations are symmetrical, thus the sign of the velocities can be interchanged. The initial parameters related to the mid-plane are following the prescription in Section 2.5.2. Though, because the phase-space of initial parameters increases significantly when a scale-height is introduced, the initial vertical positions for each planetesimal is picked randomly from a uniform distribution, $\mathbb{U}$, between $\pm R_\mathrm{b}$. Thus the initial conditions for each planetesimal is determined as

$$z_0 = R_\mathrm{b}\, \mathbb{U}(-1,1), \quad \& \quad v_{\mathrm{z},0} = \Omega R_\mathrm{b} \cos\left(\sin^{-1}\left(\frac{z_0}{R_\mathrm{b}}\right)\right)\mathbb{D}(-1,1), \tag{3.3}$$

where $\mathbb{D}$ obtains the value -1, or 1, stochastically. In total 40 simulations are repeated for each scale-height accounted for, such that the mean accretion rate becomes stable. The procedure is done for scale-heights of $R_{\rm b} = [0.1, 0.5, 0.75, 1, 1.5]\, R_{\rm Hill}$,.

3.6.3.2 Results

Figure 3.18 shows the accretion rate for a $10\, M_\oplus$ core located at 5 au. For comparison to the nominal model, the CCA and the PMA model without vertical oscillations are shown as black squares and red triangles, respectively (see bottom left in Figure 3.16). The yellow filled circles are the mean accretion rates as obtained from 40 simulations including vertical oscillations and without considering ablation. Yellow line(s) are further drawn between the minimal and the maximal accretion rates that were obtained in the 40 simulations. Thus, a long yellow line corresponds to a large spread in the outcomes, while short lines indicate a more consistent accretion rate. The black crosses, mark the mean of the full accretion rates from the 40 simulations that included both vertical oscillations and ablation. Finally, the dotted black lines shown the span of the accretion rates obtained in the simulations that include ablation.

The results shown in Figure 3.18 correspond to a scale-height of $R_{\rm b} = 0.1\, R_{\rm Hill}$. For the particle sizes of $10^3 - 10^5$ cm, the outcomes are stable, as no spread is seen for both the PMA (black dotted) and the CCA (yellow line). Their corresponding mean values are thus stable and are furthermore essentially on top of the nominal results. For planetesimals of 10^6 cm in size, the accretion rates in the CCA range from no accretion, to about $\sim 10^{-4}\, {\rm M}_\oplus\, {\rm yr}^{-1}$. Meanwhile, for the PMA, the accretion rates are more consistent but still span over one order of magnitude. This is because the particles in the PMA have a much larger cross-section, defined by the water ice line, in comparison to the CCA, making it more difficult to pass the protoplanet without depositing mass. The largest planetesimals of $10^7 - 10^8$ cm are barely being accreted in the CCA, and in the PMA simulations, a significant drop compared to the nominal model is observed.

Figure 3.19 shows the accretion rates as a function of particle size, as described in the first paragraph of this section, but for scale-heights of 0.5 and $0.75\, R_{\rm Hill}$ (top), and further for 1 and $1.5\, R_{\rm Hill}$ (bottom). First thing to notice is that the $10^7 - 10^8$ cm planetesimals, in the top panel, do get accreted in the CCA scenario, in contrast to Figure 3.18. However, at a scale-height of 1 and $1.5\, R_{\rm Hill}$ (bottom) they result in no accretion. The outcome of the two largest planetesimals can thus be concluded to still behave stochastically in my results.

On the other hand, the mean accretion rates obtained for the small to the intermediate planetesimals of $10^3 - 10^6$ cm behave as expected. That is, for an increasing scale-height, the probability of being accreted goes down, both in the CCA and the PMA. Notably, for a scale-height of $1\, R_{\rm Hill}$, the accretion of planetesimals above 10^4 cm decreases by more than an order of magnitude in comparison to the nominal model.

We note that the spread of the outcomes stretches over at least an order of a magnitude for the planetesimals larger than 10^3 cm if the scale-height is increased above $0.1\, R_{\rm Hill}$.

Thought, the spreading of the outcomes should not be over-interpreted, because with an increasing scale-height, the number of possible initial configurations increase as well, and the data becomes more scattered. Consequently, the smaller scale-heights shown are more reliable compared to the larger ones.

3.6.3.3 Conclusion

From the study of the vertical scale-heights, I can conclude that for the largest particles of $10^7 - 10^8$ cm, a small scale-height is enough to significantly lower the accretion rates by about an order of magnitude.

The accretion rates of the smaller planetesimals (10^3 cm) are less affected by the vertical oscillations, indicating that they settle efficiently towards the mid-plane and approach the values obtained in the nominal model.

The general trend, as observed for the intermediate planetesimal population $10^3 - 10^6$ cm is a decreasing accretion rate with increasing scale-height.

Finally, the accretion rates obtained from the mid-plane model are upper limits, where for at least the two largest planetesimal-sizes, the accretion rates are expected to be at least an order of magnitude lower. Nonetheless, in this work I focus on the effects introduced by particle destruction, and the exact accretion rate for planetesimals is a topic for future work.

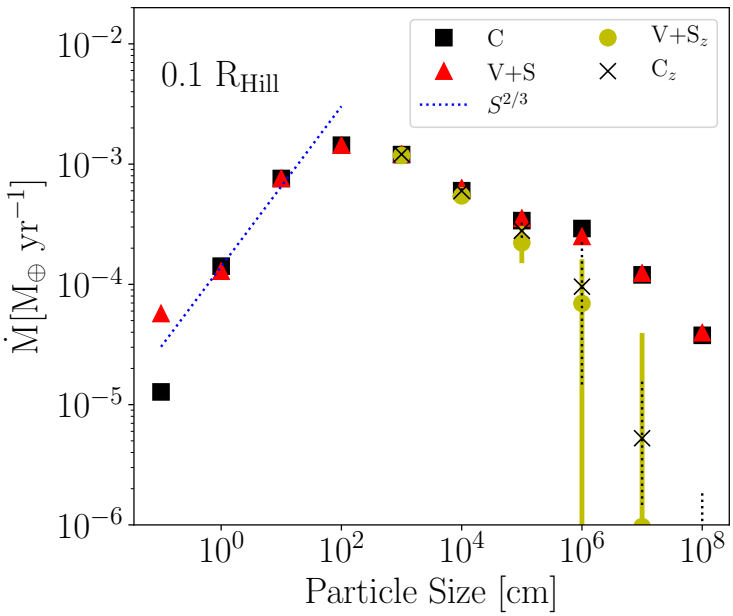

Figure 3.18: The dependence of the accretion rate on the vertical oscillations of planetesimals with sizes above 10^2 cm. Here, the scale-height on the vertical oscillations is set to $0.1\,R_{\rm Hill}$. The yellow circles are the mean values of the accretion rates obtained from 40 simulations with a CCA scenario. The black crosses correspond to the mean accretion rate obtained in the PMA case. The yellow lines, and the black dotted lines, span between the maximum and the minimum accretion rates obtained in the CCA and PMA simulations, respectively. In the background, the nominal accretion rates have been plotted, corresponding to the bottom left panel in Figure 3.16.

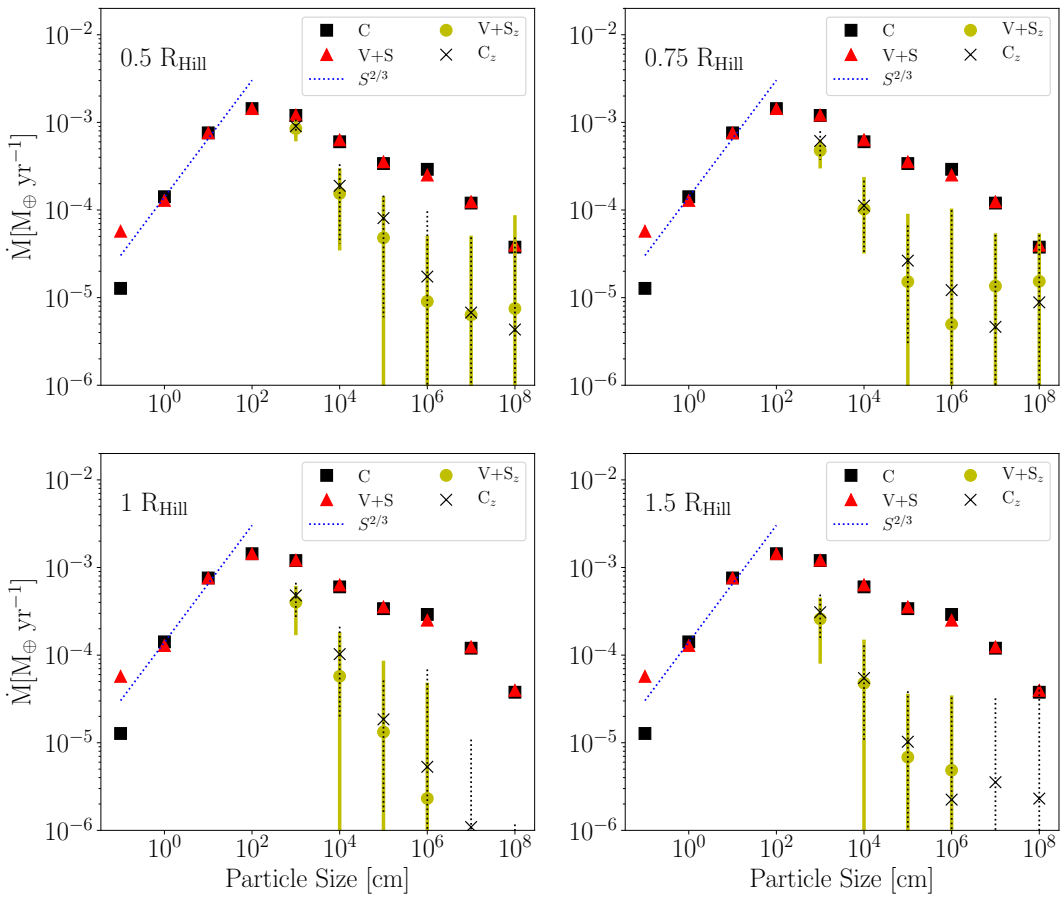

Figure 3.19: Same plot as in Figure 3.18, but for different vertical scale-heights. While the populations with the largest planetesimal show a chaotic behaviour as the scale-height is increased, the accretion rates related to the small and the intermediate planetesimals decrease.

Chapter 4

Discussion and Conclusions

In this thesis, I have demonstrated the various fate of pebbles and planetesimals that enter protoplanetary envelopes. This has been achieved by the means of 2D simulations in a controlled environment in a shearing-box frame centred on the protoplanet.

The main focus involves the trajectory-dynamics, the radius at which particles are destroyed inside the envelopes, the ablation rate and the surface temperature evolution, and the dynamical pressures obtained by the impactors. The results from the single particle trajectories and the ablation rates are then used to estimate the accretion rate onto protoplanets, differing between the deposition of vapour in the envelope and the solid material that reaches the core. Furthermore, the total mass deposition, when including the destruction of particles, is compared to the classical core accretion model, where no destruction is assumed. Finally, vertical oscillations in the disc have been introduced for the planetesimals in order to show the relation between the scale-height and the accretion rates.

In this chapter, the results are connected to the larger picture in planet formation, and the methodology is discussed with some suggestions of future work.

4.1 Protoplanetary vapour-blobs

In Section 3.6.1, I found that at 5 au, thus outside the water ice line, accreted pebbles up to 10^2 cm in size are fully sublimated by protoplanets with core masses above $0.5\,M_\oplus$. For boulders of 10^3 and 10^4 cm in size, the core requires a mass between $1-5\,M_\oplus$ to fully sublimate the material, and to fully destroy 10^5 and 10^6 cm planetesimals, a core mass above $5-10\,M_\oplus$ is needed. For the very large 10^7 and 10^8 cm planetesimals, the core has to be several tenths of Earth-masses. However, the dominant size of the accreted solids is yet unknown, and simple power-law distributions of the dust populations are commonly applied to observations (Birnstiel et al. 2018).

Because the cores of gas giants have to form within a few $\sim 10^6$ yr, particles with Stokes number about unity (10^1-10^2 cm at 5 au) are often considered a promising population, because they can contribute mass on the order of 10^{-4} to about $10^{-3}\,M_\oplus\,\mathrm{yr}^{-1}$. In Section 3.6.3, I find that planetesimal accretion can be as inefficient as 10^{-6} to $10^{-5}\,M_\oplus\,\mathrm{yr}^{-1}$ and is thus not favourable. Note, that for every accretion rate evaluated in this work, all the

dust from the MMSN is assumed to reside in the size population in question. Since the accretion rates scale linearly with the dust column-density, a reduction by a factor 10 of the dust material results in planetary growth time-scales becoming longer than the typical disc life-time in the case of planetesimal dominated accretion.

If pebbles dominate the dust population in the protoplanetary disc, my results in Section 3.6.1 indicate that every protoplanetary core with a mass above $0.5\,M_\oplus$ is capable of fully sublimating the impactors. Thus, a possibility is that the protoplanets become vapour-blobs during their active accretion phase. In Section 3.5, I found that the water of the pebbles is likely deposited at the theoretical ice lines inside the envelopes. Thus, the evolution of the chemical composition in the envelope is likely driven by the motion of the gas that comes from the disc rather than by solids that would penetrate down to the core. As discussed in Section 2.3.2.1, analysis of the gas-flows inside protoplanetary envelopes by the means of hydrodynamical simulations are needed to understand the transport of the vaporized material. A detailed analysis of the gas-flow inside the envelope could help understanding whether the protoplanets become polluted by the evaporated material or if the material is transported away. The latter being found by e.g. Popovas et al. (2018).

If protoplanets are vapour-blobs once they reach half an Earth-mass, the evolution-path of the internal structure to become either a gas-giant, or a terrestrial planet is not clear. The fact that the gas-giants in our solar-system have diluted or solid cores, as modelled by measuring their gravitational moments (Helled 2018; Bolton et al. 2017), suggest that the solid material of the protoplanetary vapour-blobs would need to form from the material inside their envelopes. For example, by the settling of heavy elements. Another possibility is that the cores grow by planetesimal accretion, while the pebbles deposit mass to the envelope. However, in Section 3.6.1, I found that solid accretion from planetesimals is feasible only up to about $1\,M_\oplus$, limiting the latter scenario.

4.2 The method

In this thesis, I use the well understood MMSN and an adiabatic envelope. As mentioned in Section 2.2, the model is comparable to those that include convective and radiative zones (Lambrechts et al. 2014). Though, below a few core radii, the density in my model and the temperature is becoming underestimated, which connects to the dynamical pressures obtained (Section 3.4). However, the radius at which particles would fragment is still on the order of $1-3\,R_\mathrm{c}$ if the density was increased – a region that most planetesimals do not reach before getting ablated, or that they reached in rare cases when they impacted the core. Because the dynamical pressure limits were not reached unless the planetesimals essentially were impacting the core, the Collective Wake model was not used frequently. Nonetheless, If the particles were to be more fragile, the argument of particles being destroyed in the envelope, and that protoplanets are vapour-blobs would be strengthened.

The nominal model used in this work consists of a $10\,M_\oplus$ core, located at 5 au. This is because at $10\,M_\oplus$, the condensation lines become well separated from the core, such that the ablation could be analysed in detail. Furthermore, at 5 au, the MMSN is a

better approximation to more advanced disc models, e.g. Bitsch et al. (2015), compared to distances further out, or closer in, inside the protoplanetary the disc.

The ablation model is based on finding the equilibrium surface temperature for a given background radiation and frictional energy. The vapour content is assumed to be stripped away from the solids as soon as it leaves the surface, which is a fair approximation at the velocities of the impactors relative to the gas (Section 3.4). Consequently, the sublimation rates do not saturate. Further analysis of the ablation rate was done in Section 3.3.1, where I found that the latent cooling of the impactors is very efficient.

The parameters that regulated the ablation rates are the latent heat of sublimation, $L_{\rm s}$, the fraction of dissipated energy from the gas, Λ, and the reflectivity and absorption efficiency parameter, ϵ. The latent heat is assumed to be given by a water and rocky mixture (Table 2.3), which is about a factor 2.8 smaller than for pure rock D'Angelo & Podolak (2015). Nonetheless, both the latent heat for rock and water is used in the literature, e.g. Brouwers et al. (2018); Podolak et al. (1988). The latent heat also limits the sublimation at critical temperatures, which are not reached at the surface of the solids in my simulations. However, when calculating the equilibrium surface temperatures (Equation 2.46), a larger latent heat corresponds to a colder surface temperature. It is thus of interest to analyse whether a small change in the latent heat can change the ablation rate significantly. For ϵ and Λ, they are most commonly set to unity, and a constant, respectively D'Angelo & Podolak (2015); Podolak et al. (1988); Ronnet et al. (2017). Nonetheless, work is currently being done regarding the fraction of absorbed energy due to friction, e.g. one model being presented in Brouwers et al. (2018), and should be compared.

4.3 Conclusions

In this section I summarise the conclusions from this work.

1. The inclusion of ablation results in pebbles, up to $\sim 10^2$ cm in size, being fully ablated in the envelopes of protoplanets with core masses above $0.5\,M_\oplus$, assuming a smooth transition between the envelope and the disc (Section 3.6.1). Small planetesimals, on the order of $\sim 10^3 - 10^4$ cm, are fully ablated for core masses about $1 - 5\,M_\oplus$, and the intermediate size planetesimals, $\sim 10^5 - 10^6$ cm, are fully ablated above core masses of $5 - 10\,M_\oplus$. For larger impactors, the core mass has to reach several $10\,M_\oplus$. Because the impactors are ablated inside the envelopes from as early as for core masses of $0.5\,M_\oplus$, protoplanets accrete material predominantly in the form of vapour. Consequently, protoplanets can be considered vapour-blobs.

2. The total amount of vapour and solid material that is deposited inside the envelopes remains the same as in the classical core accretion scenario up to about core masses of $10\,M_\oplus$. Above this mass, the condensation lines become large enough, compared to the Hill region, for the vapour accretion to be enhanced compared to the accretion of solids (Section 3.6.2).

3. Small particles, $10^{-1} - 10^{0}$ cm, can dry out before they reach the ice line and then be transported away from the protoplanet due to strong coupling to the gas (Section 3.5).

4. The latent heat is very efficient at cooling the impactors. The difference between the surface temperatures and the envelope can reach up to a few hundred Kelvin (Section 3.3.1). The sublimation rates are thus significantly lowered by the latent heat. As a consequence, multiple scatterings of planetesimals are needed to fully ablate these impactors. Nonetheless, trajectories with reoccurring scattering events are observed.

5. The most efficiently accreted particles are those with Stokes numbers ~ 1, both when ablation is included and without.

6. The vertical oscillations of planetesimals can lower the accretion rates significantly. While planetesimals on the order of 10^{3} cm are settling towards the mid-plane efficiently, thus being less affected by the scale-height variations, the accretion rates related to the larger planetesimals can drop by orders of magnitude. The corresponding protoplanetary growth time-scales then become comparable to the disc life-time (Section 3.6.3). Consequently, planetesimal accretion is not likely the dominant factor for growing protoplanets.

7. Fragmentation does not play an important role in accretion models unless the internal strength of the impactors is comparable to dynamical pressures on the order of $\lesssim 10^{6}$ dyne cm^{-2} (Section 3.4). Fragmentation is then expected to occur at distances about a few core radii from the protoplanetary surface. Nonetheless, most impactors have fully ablated before reaching these heights.

Appendix A

A.1 Trajectories for all the particle sizes around a 10 $M_\oplus$ core at 5 au

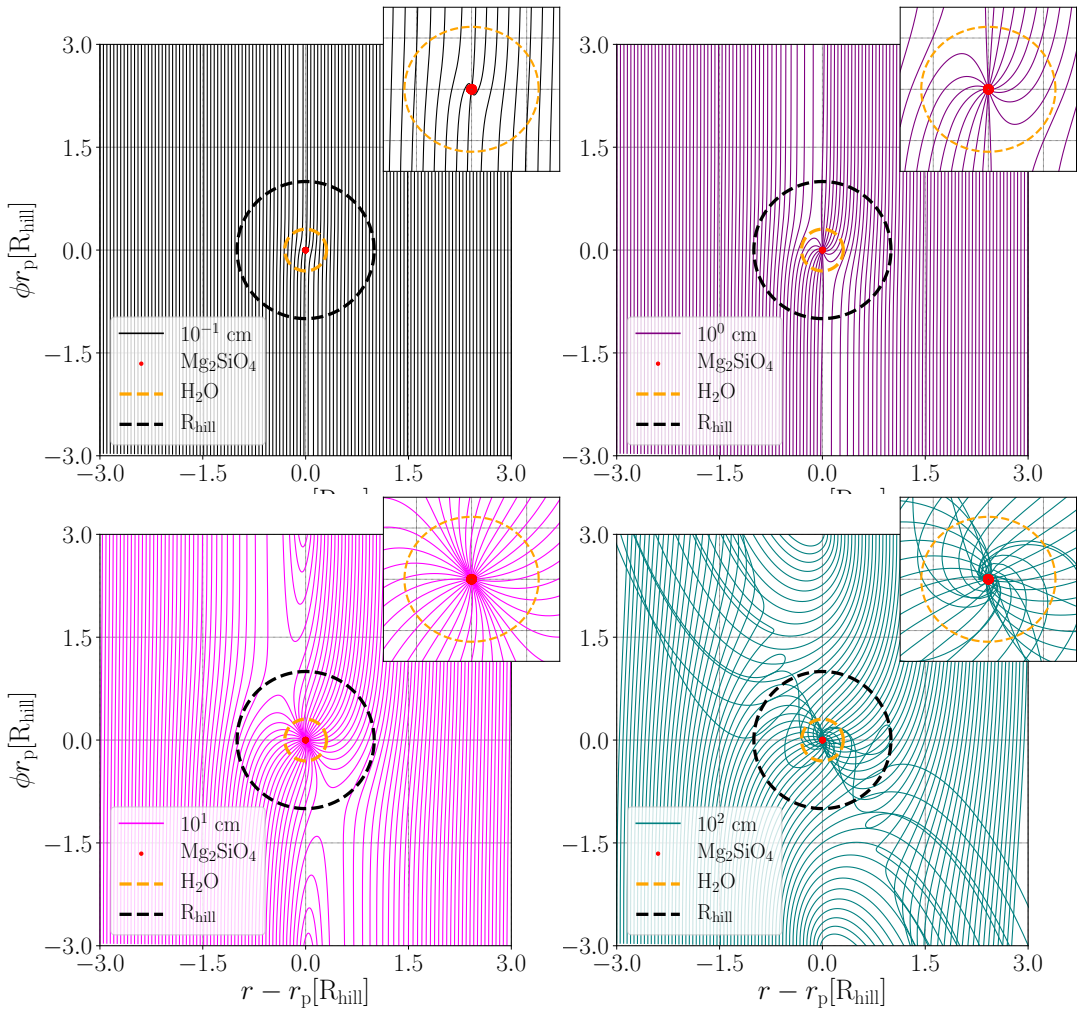

Figure A.1: All trajectories when sublimation is included, highlighting the surrounding particle-flows that are not shown in Section 3.1.

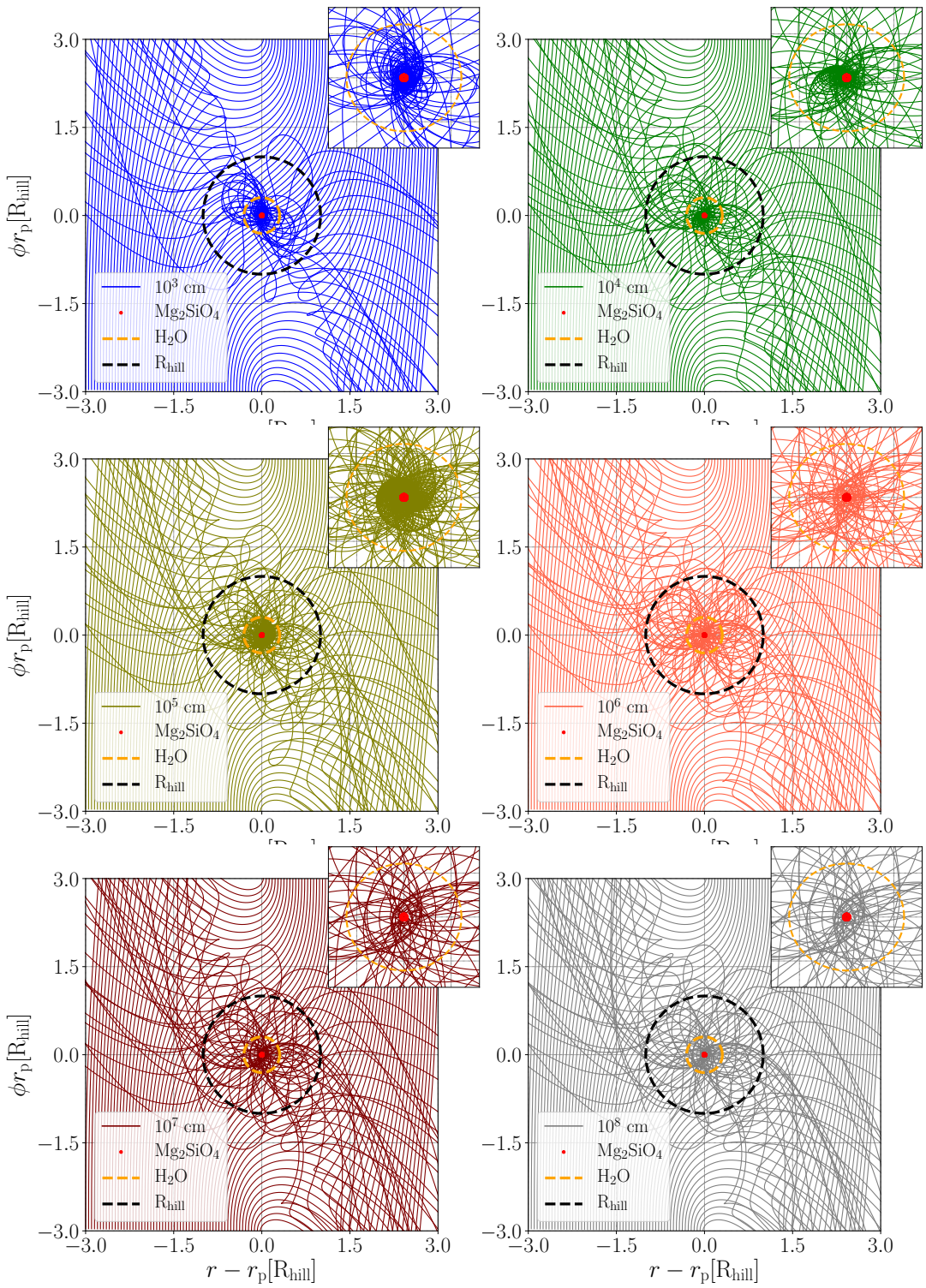

Figure A.2: Continuation of Figure A.1.

A.2 Trajectories of pebbles around a 50 $M_\oplus$ core

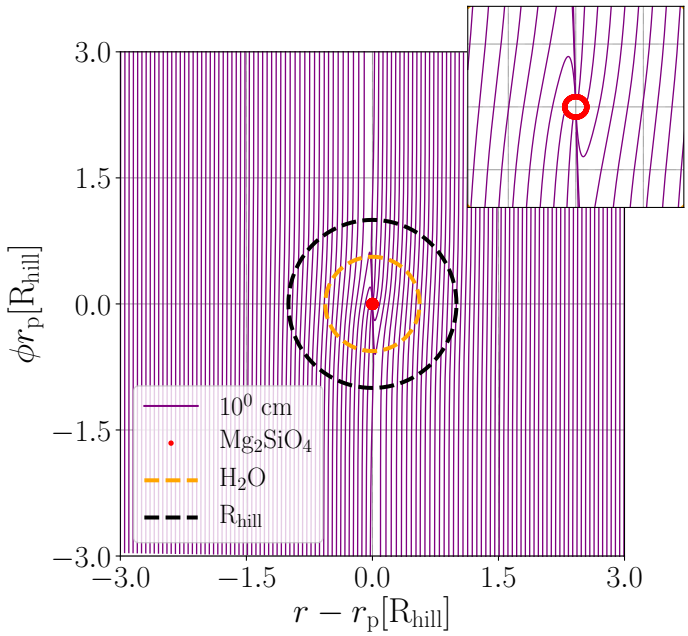

Figure A.3: The 10^0 cm size pebbles around a 50 $M_\oplus$ core are strongly coupled to the gas. For the classical core accretion model, the majority passes through the envelope without interaction. However, if ablation is included they sublimate their water-content as they pass the ice line. Thus the total accretion rate, as shown in the bottom panel of Figure 3.16, increases significantly in comparison to the classical accretion.

A.3 The material accreted in the form of vapour versus full accretion as a function semi-major axis

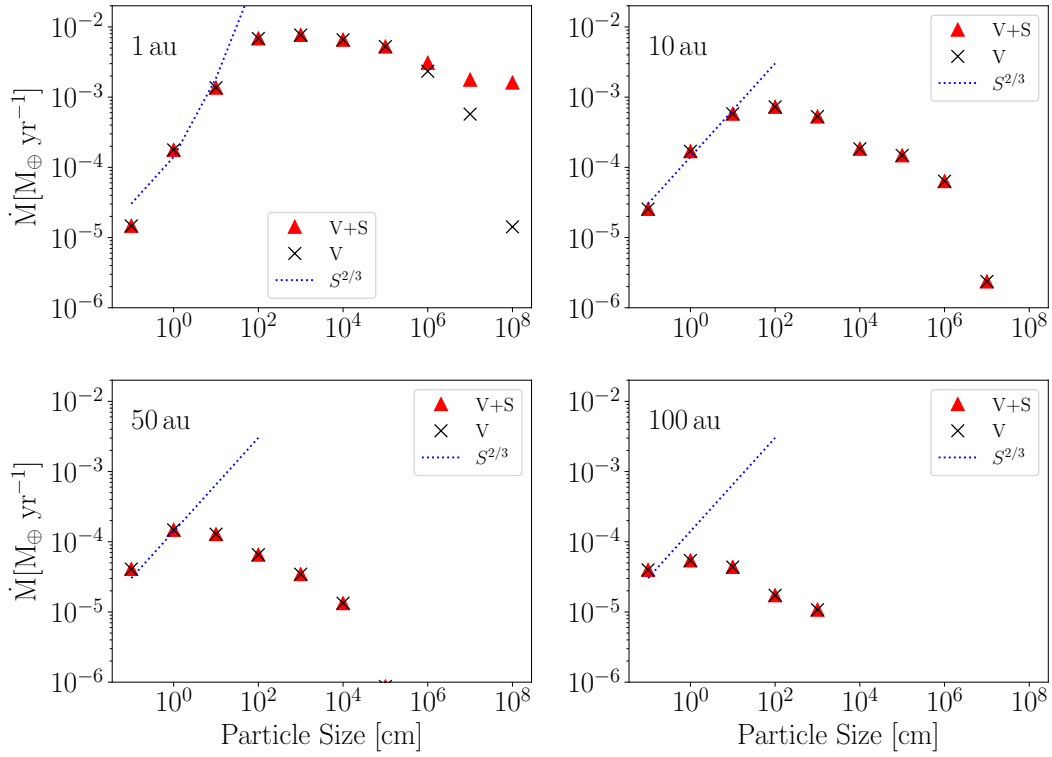

Figure A.4: The total accretion rates of material in the form of vapour (black cross) and both vapour and solid (red triangles) for a core mass of 10 $M_\oplus$, at 1, 10, 50, and 100 au, as discussed in Section 3.6.1. The blue line corresponds to the Hill accretion. The shape of the Hill accretion in the top left panel is due to the non-linear regime being reached for the friction-times (Section 2.3.1.1). Nonetheless, the protoplanets are capable of sublimating all the impactors that deposit material above 10 au. For 1 au, the result is similar to the nominal model, shown in Figure 3.15. However, in this case the impactors only consist of silicate.

Appendix B

B.1 Terminal velocities in hydrostatic equilibrium

In Section 2.3.2, a set of four equations are introduced which describe the gas-flow and terminal velocities of small dust grains. To avoid confusion throughout the derivation I define a set of constants:

$$\begin{array}{ll} a = A\rho_{\mathrm{g}} & b = 2\Omega_{\mathrm{p}} \\ c = GM_{\mathrm{p}}x/\mathbf{r}^3 & d = (1/2)\Omega_{\mathrm{p}} \\ e = GM_{\mathrm{p}}y/\mathbf{r}^3 & f = A\rho_{\mathrm{d}} \\ g = 2\Omega_{\mathrm{k}}\eta v_{\mathrm{k}}. & \end{array}$$

The equations to be solved in the equilibrium case can then be written

$$0 = -a(v_x - u_x) + bv_y - c \tag{B.1}$$
$$0 = -a(v_y - u_y) - dv_x - e \tag{B.2}$$
$$0 = -f(u_x - v_x) + bu_y + g \tag{B.3}$$
$$0 = -f(u_y - v_y) - du_x. \tag{B.4}$$

From Equation B.1 I get that

$$(u_x - v_x) = \frac{c}{a} - \frac{b}{a}v_y$$

which is inserted into Equations B.3, resulting in

$$u_y = \frac{cf - ag}{ab} - \frac{bf}{ab}v_y \tag{B.5}$$

The result is substituted into Equation B.2 and B.4, respectively, to find that

$$v_x = \frac{cf - ag}{bd} - \frac{bf}{bd}v_y - \frac{a}{d}v_y - \frac{e}{d} = \frac{cf - ag - be}{bd} - \frac{ab + bf}{bd}v_y \tag{B.6}$$
$$u_x = \frac{-cf^2 + agf}{abd} + \frac{bf^2}{abd}v_y + \frac{f}{d}v_y = \frac{-cf^2 + agf}{abd} + \frac{bf^2 + abf}{abd}v_y, \tag{B.7}$$

B.1.1 Solving for v_y

Equation B.6 and B.7 are inserted into Equation B.1 where I solve for v_y

$$0 = \frac{-cf^2 + agf}{bd} + \frac{bf^2 + abf}{bd}v_y + \frac{-acf + a^2g + abe}{bd} + \frac{a^2b + abf}{bd}v_y + bv_y - c;$$

$$v_y = \frac{cf^2 - agf + acf - a^2g - abe + bcd}{bf^2 + abf + a^2b + abf + b^2d} = \frac{-(a^2 + af)}{b((f+a)^2 + bd)}g + \frac{(f^2 + af + bd)c - abe}{b((f+a)^2 + bd)}; \tag{B.8}$$

The disc-dependent parts of the equation can now be extracted (terms that include g). Following, I reinsert the notations used and further assume that the global pressure gradient does not change significantly within the shearing-box, hence $\Omega_\mathrm{k} \approx \Omega_\mathrm{p}$, thus

$$v_y = \frac{-A^2(\rho_\mathrm{g}^2 + \rho_\mathrm{g}\rho_\mathrm{d})}{2\Omega_\mathrm{p}(A^2(\rho_\mathrm{d} + \rho_\mathrm{g})^2 + \Omega_\mathrm{p}^2)} 2\Omega_\mathrm{k}\eta v_\mathrm{k} + \frac{(A^2\rho_\mathrm{d}^2 + A^2\rho_\mathrm{d}\rho_\mathrm{g} + \Omega_\mathrm{p}^2)x - 2A\rho_\mathrm{g}\Omega_\mathrm{p}y}{2\Omega_\mathrm{p}(A^2(\rho_\mathrm{d} + \rho_\mathrm{g})^2 + \Omega_\mathrm{p}^2)} \frac{GM_\mathrm{p}}{\mathbf{r}^3}$$

In order to couple the equation to the Stokes number, τ, recall from Section 2.3 that

$$A(\rho_\mathrm{d} + \rho_\mathrm{g}) = \frac{\Omega}{\tau} \tag{B.9}$$

In order to get the standard notation for the disc-part, the equation is multiplied by $(\rho_\mathrm{d}+\rho_\mathrm{g})$ such that

$$v_y = -\frac{\rho_\mathrm{g}}{(\rho_\mathrm{d} + \rho_\mathrm{g})} \frac{\left(\frac{\Omega}{\tau}\right)^2}{(\left(\frac{\Omega}{\tau}\right)^2 + \Omega^2)} \eta v_\mathrm{k} + \frac{(\rho_\mathrm{g} + \rho_\mathrm{d})^2}{(\rho_\mathrm{d} + \rho_\mathrm{g})} A^2 \frac{(\rho_\mathrm{d} + \tau^2(\rho_\mathrm{d} + \rho_\mathrm{g}))x - 2\tau\rho_\mathrm{g}y}{2\Omega_\mathrm{p}(\left(\frac{\Omega}{\tau}\right)^2 + \Omega^2)} \frac{GM_\mathrm{p}}{\mathbf{r}^3};$$

$$v_y = -\frac{\rho_\mathrm{g}}{(\rho_\mathrm{d} + \rho_\mathrm{g})} \frac{1}{\tau^2 + 1} \left[\eta v_\mathrm{k} - \frac{1}{2\Omega_\mathrm{p}} \left((\frac{\rho_\mathrm{d}}{\rho_\mathrm{g}} + \tau^2(\frac{\rho_\mathrm{d}}{\rho_\mathrm{g}} + 1))x - 2\tau y \right) \frac{GM_\mathrm{p}}{\mathbf{r}^3} \right];$$

Finally, the terminal velocity of dust grains becomes

$$v_y = -\frac{\rho_\mathrm{g}}{(\rho_\mathrm{d} + \rho_\mathrm{g})} \frac{1}{\tau^2 + 1} \left[\eta v_\mathrm{k} - \frac{1}{\Omega_\mathrm{p}} \left((\frac{\rho_\mathrm{d}}{2\rho_\mathrm{g}}(\tau^2 + 1) + \frac{\tau^2}{2})x - \tau y \right) \frac{GM_\mathrm{p}}{\mathbf{r}^3} \right], \tag{B.10}$$

and for $\rho_\mathrm{d} \ll \rho_\mathrm{g}$ I obtain

$$v_y = -\frac{1}{\tau^2 + 1} \left[\eta v_\mathrm{k} - \frac{1}{\Omega_\mathrm{p}} \left(\frac{\tau^2}{2}x - \tau y \right) \frac{GM_\mathrm{p}}{\mathbf{r}^3} \right], \tag{B.11}$$

B.1.2 Solving for v_x

To solve for v_x, u_x and u_y I substitute Equation B.10 into Equations B.6, B.7 and B.5, respectively. Reinserting the quantities in Equation B.6 I obtain that

$$\Omega_\mathrm{p}^2 v_x = (A\rho_\mathrm{d}x - 2\Omega_\mathrm{p}y)\frac{GM_\mathrm{p}}{\mathbf{r}^3} - 2A\rho_\mathrm{g}\Omega_\mathrm{p}\eta v_\mathrm{k} - 2A\Omega_\mathrm{p}(\rho_\mathrm{d} + \rho_\mathrm{g})v_y;$$

While inserting the expression for v_x (Equation B.10), I multiply by the inverse pre-factor such that

$$\begin{aligned}
&\frac{(\rho_\mathrm{d}+\rho_\mathrm{g})}{\rho_\mathrm{g}}(\tau^2+1)\Omega_\mathrm{p}^2 v_x = \\
&\frac{(\rho_\mathrm{d}+\rho_\mathrm{g})}{\rho_\mathrm{g}}(\tau^2+1)(A\rho_\mathrm{d}x - 2A\tau(\rho_\mathrm{d}+\rho_\mathrm{g})y)\frac{GM_\mathrm{p}}{\mathbf{r}^3} - \\
&\frac{(\rho_\mathrm{d}+\rho_\mathrm{g})}{\rho_\mathrm{g}}(\tau^2+1)2A\rho_\mathrm{g}\Omega_\mathrm{p}\eta v_\mathrm{k} + \\
&2A\Omega_\mathrm{p}(\rho_\mathrm{d}+\rho_\mathrm{g})\left[\eta v_\mathrm{k} - \frac{1}{\Omega_\mathrm{p}}\left(\left(\frac{\rho_\mathrm{d}}{2\rho_\mathrm{g}}(\tau^2+1)+\frac{\tau^2}{2}\right)x - \tau y\right)\frac{GM_\mathrm{p}}{\mathbf{r}^3}\right];
\end{aligned}$$

I then sort out the disc and protoplanetary part, respectively,

$$\begin{aligned}
&\frac{(\rho_\mathrm{d}+\rho_\mathrm{g})}{\rho_\mathrm{g}}(\tau^2+1)\Omega_\mathrm{p}^2 v_x = \\
&-2A\Omega_\mathrm{p}(\rho_\mathrm{d}+\rho_\mathrm{g})\big[(\tau^2+1)-1\big]\eta v_\mathrm{k} \\
&+\left[-A(\rho_\mathrm{d}+\rho_\mathrm{g})\tau^2 x - 2A\tau\frac{(\rho_\mathrm{d}+\rho_\mathrm{g})}{\rho_\mathrm{g}}\big(\rho_\mathrm{d}(\tau^2+1)+\rho_\mathrm{g}\tau^2\big)y\right]\frac{GM_\mathrm{p}}{\mathbf{r}^3}
\end{aligned}$$

Finally, I clean up the left-hand side and use Equation B.9 to show that

$$\begin{aligned}
v_x = &\frac{\rho_\mathrm{g}}{(\rho_\mathrm{d}+\rho_\mathrm{g})}\frac{1}{\tau^2+1}\frac{1}{\Omega_\mathrm{p}^2}\Bigg[-2\Omega_\mathrm{p}^2\tau\eta v_\mathrm{k} \\
&+\left[-\Omega_\mathrm{p}\tau x - 2\Omega_\mathrm{p}\frac{1}{\rho_\mathrm{g}}\big(\rho_\mathrm{d}(\tau^2+1)+\rho_\mathrm{g}\tau^2\big)y\right]\frac{GM_\mathrm{p}}{\mathbf{r}^3}\Bigg],
\end{aligned}$$

and thus

$$v_x = -2\frac{\rho_\mathrm{g}}{(\rho_\mathrm{d}+\rho_\mathrm{g})}\frac{\tau}{\tau^2+1}\left[\eta v_\mathrm{k} + \frac{1}{\Omega_\mathrm{p}}\left[\frac{1}{2}x + \left(\frac{\rho_\mathrm{d}(\tau^2+1)}{\tau\rho_\mathrm{g}}+\tau\right)y\right]\frac{GM_\mathrm{p}}{\mathbf{r}^3}\right] \tag{B.12}$$

In the case of $\rho_\mathrm{d} \ll \rho_\mathrm{g}$ I get that

$$v_x = -2\frac{\tau}{\tau^2+1}\left[\eta v_\mathrm{k} + \frac{1}{\Omega_\mathrm{p}}\left(\frac{1}{2}x+\tau y\right)\frac{GM_\mathrm{p}}{\mathbf{r}^3}\right]. \tag{B.13}$$

B.1.3 Solving for u_x

The same principle is used on the velocity field of the gas. From Equation B.7 I get

$$A\rho_\mathrm{g}\Omega_\mathrm{p}^2 u_x = -A\rho_\mathrm{d}^2\frac{GM_\mathrm{p}}{\mathbf{r}^3}x + 2A\rho_\mathrm{d}\rho_\mathrm{g}\Omega_\mathrm{p}\eta v_\mathrm{k} + 2A\Omega_\mathrm{p}\rho_\mathrm{d}(\rho_\mathrm{d}+\rho_\mathrm{g})v_y$$

Again, the equation is multiplied by the inverse pre-factor of v_y;

$$\begin{aligned}
&\frac{(\rho_\mathrm{d}+\rho_\mathrm{g})}{\rho_\mathrm{g}}(\tau^2+1)\rho_\mathrm{g}\Omega_\mathrm{p}^2 u_x = \\
&-\frac{(\rho_\mathrm{d}+\rho_\mathrm{g})}{\rho_\mathrm{g}}(\tau^2+1)A\rho_\mathrm{d}^2\frac{GM_\mathrm{p}}{\mathbf{r}^3}x \\
&+\frac{(\rho_\mathrm{d}+\rho_\mathrm{g})}{\rho_\mathrm{g}}(\tau^2+1)2A\rho_\mathrm{d}\rho_\mathrm{g}\Omega_\mathrm{p}\eta v_\mathrm{k} \\
&-2A\Omega_\mathrm{p}\rho_\mathrm{d}(\rho_\mathrm{d}+\rho_\mathrm{g})\left[\eta v_\mathrm{k}-\frac{1}{\Omega_\mathrm{p}}\left((\frac{\rho_\mathrm{d}}{2\rho_\mathrm{g}}(\tau^2+1)+\frac{\tau^2}{2})x-\tau y\right)\frac{GM_\mathrm{p}}{\mathbf{r}^3}\right]
\end{aligned}$$

Which simplifies to

$$\begin{aligned}
&\frac{(\rho_\mathrm{d}+\rho_\mathrm{g})}{\rho_\mathrm{g}}(\tau^2+1)\rho_\mathrm{g}\Omega_\mathrm{p}^2 u_x = \\
&+2A\Omega_\mathrm{p}\rho_\mathrm{d}(\rho_\mathrm{d}+\rho_\mathrm{g})\tau^2\eta v_\mathrm{k} \\
&+\left[A(\rho_\mathrm{d}+\rho_\mathrm{g})\rho_\mathrm{d}\tau^2 x-2A\rho_\mathrm{d}\tau(\rho_\mathrm{d}+\rho_\mathrm{g})y\right]\frac{GM_\mathrm{p}}{\mathbf{r}^3},
\end{aligned}$$

leading to the final result

$$u_x = 2\frac{\rho_\mathrm{d}}{(\rho_\mathrm{d}+\rho_\mathrm{g})}\frac{\tau}{\tau^2+1}\left[\eta v_\mathrm{k}+\frac{1}{\Omega_\mathrm{p}}\left[\frac{1}{2}x-\frac{1}{\tau}y\right]\frac{GM_\mathrm{p}}{\mathbf{r}^3}\right]. \tag{B.14}$$

Notably, a low density of dust makes the terminal velocity approach a value of zero.

B.1.4 Solving for u_y

For the azimuthal velocity of the gas, it follows from Equation B.5 that

$$2A\Omega_\mathrm{p}\rho_\mathrm{g}u_y = A\rho_\mathrm{d}\frac{GM_\mathrm{p}}{\mathbf{r}^3}x-2A\Omega_\mathrm{p}\rho_\mathrm{g}\eta v_\mathrm{k}-2A\Omega_\mathrm{p}\rho_\mathrm{d}v_y$$

Multiplying by the inverse pre-factor of v_y I get

$$\begin{aligned}
&\frac{(\rho_\mathrm{d}+\rho_\mathrm{g})}{\rho_\mathrm{g}}(\tau^2+1)2A\Omega_\mathrm{p}\rho_\mathrm{g}u_y = \\
&+\frac{(\rho_\mathrm{d}+\rho_\mathrm{g})}{\rho_\mathrm{g}}(\tau^2+1)A\rho_\mathrm{d}\frac{GM_\mathrm{p}}{\mathbf{r}^3}x \\
&-\frac{(\rho_\mathrm{d}+\rho_\mathrm{g})}{\rho_\mathrm{g}}(\tau^2+1)2A\Omega_\mathrm{p}\rho_\mathrm{g}\eta v_\mathrm{k} \\
&+2A\Omega_\mathrm{p}\rho_\mathrm{d}\left[\eta v_\mathrm{k}-\frac{1}{\Omega_\mathrm{p}}\left((\frac{\rho_\mathrm{d}}{2\rho_\mathrm{g}}(\tau^2+1)+\frac{\tau^2}{2})x-\tau y\right)\frac{GM_\mathrm{p}}{\mathbf{r}^3}\right]
\end{aligned}$$

Sorting the terms I obtain

$$\begin{aligned}&\frac{(\rho_\mathrm{d}+\rho_\mathrm{g})}{\rho_\mathrm{g}}(\tau^2+1)2A\Omega_\mathrm{p}\rho_\mathrm{g}u_y = \\ &+2A\Omega_\mathrm{p}\big(\rho_\mathrm{d}-(\rho_\mathrm{d}+\rho_\mathrm{g})(\tau^2+1)\big)\eta v_\mathrm{k} \\ &+\left[A\rho_\mathrm{d}x+2A\rho_\mathrm{d}\tau y\right]\frac{GM_\mathrm{p}}{\mathbf{r}^3}\end{aligned}$$

Finally, the azimuthal velocity of the gas is

$$u_y=\left(\frac{\rho_\mathrm{d}}{(\rho_\mathrm{d}+\rho_\mathrm{g})}\frac{1}{\tau^2+1}-1\right)\eta v_\mathrm{k}+\frac{\rho_\mathrm{d}}{(\rho_\mathrm{d}+\rho_\mathrm{g})}\frac{1}{\tau^2+1}\frac{1}{\Omega_\mathrm{p}}\left[\frac{1}{2}x+\tau y\right]\frac{GM_\mathrm{p}}{\mathbf{r}^3} \tag{B.15}$$

for which $\rho_\mathrm{d} \ll \rho_\mathrm{g}$ becomes

$$u_y=-\eta v_\mathrm{k} \tag{B.16}$$

B.1.5 Summary of terminal velocities

To summarize, the terminal velocities of the gas and the dust, assuming a hydrostatic envelope, are given by

$$v_x=-2\frac{\rho_\mathrm{g}}{(\rho_\mathrm{d}+\rho_\mathrm{g})}\frac{\tau}{\tau^2+1}\left[\eta v_\mathrm{k}+\frac{1}{\Omega_\mathrm{p}}\left[\frac{1}{2}x+\big(\frac{\rho_\mathrm{d}(\tau^2+1)}{\tau\rho_\mathrm{g}}+\tau\big)y\right]\frac{GM_\mathrm{p}}{\mathbf{r}^3}\right] \tag{B.17}$$

$$v_y=-\frac{\rho_\mathrm{g}}{(\rho_\mathrm{d}+\rho_\mathrm{g})}\frac{1}{\tau^2+1}\left[\eta v_\mathrm{k}-\frac{1}{\Omega_\mathrm{p}}\left(\big(\frac{\rho_\mathrm{d}}{2\rho_\mathrm{g}}(\tau^2+1)+\frac{\tau^2}{2}\big)x-\tau y\right)\frac{GM_\mathrm{p}}{\mathbf{r}^3}\right] \tag{B.18}$$

$$u_x=2\frac{\rho_\mathrm{d}}{(\rho_\mathrm{d}+\rho_\mathrm{g})}\frac{\tau}{\tau^2+1}\left[\eta v_\mathrm{k}+\frac{1}{\Omega_\mathrm{p}}\left[\frac{1}{2}x-\frac{1}{\tau}y\right]\frac{GM_\mathrm{p}}{\mathbf{r}^3}\right] \tag{B.19}$$

$$u_y=\left(\frac{\rho_\mathrm{d}}{(\rho_\mathrm{d}+\rho_\mathrm{g})}\frac{1}{\tau^2+1}-1\right)\eta v_\mathrm{k}+\frac{\rho_\mathrm{d}}{(\rho_\mathrm{d}+\rho_\mathrm{g})}\frac{1}{\tau^2+1}\frac{1}{\Omega_\mathrm{p}}\left[\frac{1}{2}x+\tau y\right]\frac{GM_\mathrm{p}}{\mathbf{r}^3}. \tag{B.20}$$

However, when the density of the dust is negligible the equations can be written as

$$v_x=-2\frac{\tau}{\tau^2+1}\big(\eta v_\mathrm{k}+\frac{1}{\Omega_\mathrm{p}}\big[\frac{x}{2}+\tau y\big]\frac{GM_\mathrm{p}}{\mathbf{r}^3}\big) \tag{B.21}$$

$$v_y=-\frac{1}{\tau^2+1}\big(\eta v_\mathrm{k}-\frac{1}{\Omega_\mathrm{p}}\big[\frac{\tau^2}{2}x-\tau y\big]\frac{GM_\mathrm{p}}{\mathbf{r}^3}\big) \tag{B.22}$$

$$u_x=0 \tag{B.23}$$

$$u_y=-\eta v_\mathrm{k}. \tag{B.24}$$

Bibliography

Ahrens, T. J., Takata, T., O'Keefe, J. D., & Orton, G. S. 1994, GRL, 21, 1087

Alibert, Y., Venturini, J., Helled, R., et al. 2018, Nature Astronomy, 2, 873

Anderson, D. E., Bergin, E. A., Blake, G. A., et al. 2017, ApJ, 845, 13

Andrews, S. M., Huang, J., Pérez, L. M., et al. 2018, ApJ, 869, L41

Asplund, M., Grevesse, N., Sauval, A. J., & Scott, P. 2009, ARA&A, 47, 481

Baruteau, C. & Masset, F. 2008, The Astrophysical Journal, 672, 1054

Benz, W. & Asphaug, E. 1999, Icarus, 142, 5

Biberman, L. M., Bronin, S. Y., & Brykin, M. V. 1980, Acta Astronautica, 7, 53

Bird, R. B., Stewart, W. E., & Lightfoot, E. N. 2006, Transport Phenomena, Revised 2nd Edition, 2nd edn. (John Wiley & Sons, Inc.)

Birnstiel, T., Dullemond, C. P., Zhu, Z., et al. 2018, ApJ, 869, L45

Bitsch, B., Johansen, A., Lambrechts, M., & Morbidelli, A. 2015, A&A, 575, A28

Bitsch, B., Morbidelli, A., Johansen, A., et al. 2018, A&A, 612, A30

Bolton, S. J., Lunine, J., Stevenson, D., et al. 2017, SSR, 213, 5

Borovička, J. & Spurný, P. 1996, 121, 484

Brouwers, M. G., Vazan, A., & Ormel, C. W. 2018, A&A, 611, A65

Brown, P. G., Assink, J. D., Astiz, L., et al. 2013, Nature, 503, 238

Bryson, C. E., Cazcarra, V., & Levenson, L. L. 1974, Journal of Chemical & Engineering Data, 19, 107

Buchhave, L. A., Latham, D. W., Johansen, A., et al. 2012, Nature, 486, 375

D'Angelo, G. & Podolak, M. 2015, ApJ, 806, 203

Dormand, J. & Prince, P. 1980, Journal of Computational and Applied Mathematics, 6, 19

Draine, B. T. & Lee, H. M. 1984, ApJ, 285, 89

Dullemond, C. P., Birnstiel, T., Huang, J., et al. 2018, ApJ, 869, L46

Fedele, D., van den Ancker, M. E., Henning, T., Jayawardhana, R., & Oliveira, J. M. 2010, A&A, 510, A72

Feistel, R. & Wagner, W. 2007, GCA, 71, 36

Field, G. B. & Ferrara, A. 1995, ApJ, 438, 957

Fischer, D. A. & Valenti, J. 2005, ApJ, 622, 1102

Fortney, J. J. & Nettelmann, N. 2010, SSR, 152, 423

Fray, N. & Schmitt, B. 2009, planss, 57, 2053

Haisch, Karl E., J., Lada, E. A., & Lada, C. J. 2001, ApJ, 553, L153

Hayashi, C. 1981, Progress of Theoretical Physics Supplement, 70, 35

Haynes, D. R., Tro, N. J., & George, S. M. 1992, The Journal of Physical Chemistry, 96, 8502

Helled, R. 2018, The Interiors of Jupiter and Saturn, 175

Hughes, A. G. & Boley, A. C. 2017, MNRAS, 472, 3543

Inaba, S. & Ikoma, M. 2003, A&A, 410, 711

Johansen, A. & Lambrechts, M. 2017, Annual Review of Earth and Planetary Sciences, 45, 359

Johansen, A., Mac Low, M.-M., Lacerda, P., & Bizzarro, M. 2015, Science Advances, 1, 1500109

Johansen, A., Youdin, A. N., & Lithwick, Y. 2012, A&A, 537, A125

Kimura, H., Mann, I., Biesecker, D. A., & Jessberger, E. K. 2002, Icarus, 159, 529

Korycansky, D. G., Zahnle, K. J., & Law, M.-M. M. 2000, Icarus, 146, 387

Lambrechts, M. & Johansen, A. 2012, A&A, 544, A32

Lambrechts, M. & Johansen, A. 2014, A&A, 572, A107

Lambrechts, M., Johansen, A., & Morbidelli, A. 2014, A&A, 572, A35

Lambrechts, M. & Lega, E. 2017, A&A, 606, A146

Lodders, K. 2003, ApJ, 591, 1220

Madhusudhan, N., Amin, M. A., & Kennedy, G. M. 2014, ApJ, 794, L12

Mamajek, E. E. 2009, in American Institute of Physics Conference Series, Vol. 1158, American Institute of Physics Conference Series, ed. T. Usuda, M. Tamura, & M. Ishii, 3–10

Mizuno, H. 1980, Progress of Theoretical Physics, 64, 544

Mordasini, C., Alibert, Y., & Benz, W. 2006, in Tenth Anniversary of 51 Peg-b: Status of and prospects for hot Jupiter studies, ed. L. Arnold, F. Bouchy, & C. Moutou, 84–86

Nagahara, H., Kushiro, I., & Mysen, B. O. 1994, GCA, 58, 1951

Nakagawa, Y., Sekiya, M., & Hayashi, C. 1986, Icarus, 67, 375

Nesvorný, D., Youdin, A. N., & Richardson, D. C. 2010, AJ, 140, 785

Paardekooper, S.-J., Baruteau, C., Crida, A., & Kley, W. 2010, Monthly Notices of the Royal Astronomical Society, 401, 1950

Podolak, M., Pollack, J. B., & Reynolds, R. T. 1988, Icarus, 73, 163

Pollack, J. B., Hollenbach, D., Beckwith, S., et al. 1994, ApJ, 421, 615

Pollack, J. B., Hubickyj, O., Bodenheimer, P., et al. 1996, Icarus, 124, 62

Pollack, J. B., Podolak, M., Bodenheimer, P., & Christofferson, B. 1986, Icarus, 67, 409

Popova, O. P., Jenniskens, P., Emel'yanenko, V., et al. 2013, Science, 342, 1069

Popovas, A., Nordlund, Å., Ramsey, J. P., & Ormel, C. W. 2018, MNRAS, 479, 5136

Rafikov, R. R. 2004, AJ, 128, 1348

Register, P. J., Mathias, D. L., & Wheeler, L. F. 2017, Icarus, 284, 157

Ronnet, T., Mousis, O., & Vernazza, P. 2017, ApJ, 845, 92

Roulston, M. S. & Ahrens, T. J. 1997, Icarus, 126, 138

Santos, N. C., Israelian, G., & Mayor, M. 2004, A&A, 415, 1153

Sharp, D. H. 1984, Physica D Nonlinear Phenomena, 12, 3

Tachibana, S., Tsuchiyama, A., & Nagahara, H. 2002, GCA, 66, 713

Testi, L., Natta, A., Shepherd, D. S., & Wilner, D. J. 2003, A&A, 403, 323

Weidenschilling, S. J. 1977, MNRAS, 180, 57

Whipple, F. L. 1973, NASA Special Publication, 319, 355

Woitke, P., Kamp, I., & Thi, W.-F. 2009, A&A, 501, 383

Youdin, A. N. & Goodman, J. 2005, ApJ, 620, 459

Zahnle, K. J. 1992, JGR, 97, 10

Zhang, S., Zhu, Z., Huang, J., et al. 2018, ApJ, 869, L47